INFORMATION TO USERS

This manuscript has been reproduced from the microfilm master. UMI films the text directly from the original or copy submitted. Thus, some thesis and dissertation copies are in typewriter face, while others may be from any type of computer printer.

The quality of this reproduction is dependent upon the quality of the copy submitted. Broken or indistinct print, colored or poor quality illustrations and photographs, print bleedthrough, substandard margins, and improper alignment can adversely affect reproduction.

In the unlikely event that the author did not send UMI a complete manuscript and there are missing pages, these will be noted. Also, if unauthorized copyright material had to be removed, a note will indicate the deletion.

Oversize materials (e.g., maps, drawings, charts) are reproduced by sectioning the original, beginning at the upper left-hand corner and continuing from left to right in equal sections with small overlaps. Each original is also photographed in one exposure and is included in reduced form at the back of the book.

Photographs included in the original manuscript have been reproduced xerographically in this copy. Higher quality 6" x 9" black and white photographic prints are available for any photographs or illustrations appearing in this copy for an additional charge. Contact UMI directly to order.

UMI

A Bell & Howell Information Company
300 North Zeeb Road, Ann Arbor MI 48106-1346 USA
313/761-4700 800/521-0600

DYNAMIC WEDGE DOSIMETRY ON A DUAL ENERGY LINEAR ACCELERATOR

by

Devin P. Barry
Department of Medical Physics
McGill University, Montréal
November 1996

A Thesis submitted to the
Faculty of Graduate Studies and Research
in partial fulfillment of the requirements for the degree of
Master of Science

ABSTRACT

Radiation therapy is a treatment modality that is used in treatment of close to 50% of newly diagnosed cancer patients. External beam photon radiotherapy is typically administered by the positioning of several different radiation beams from various directions which intersect at the tumor or target within the patient. Patient anatomy often requires the use of wedge shaped isodose distributions to compensate for missing tissue, irregular surface contours, and irregular tumor volumes. For the past 40 years physical wedge filters have provided such isodose distributions but their use resulted in certain detrimental dosimetric consequences such as beam hardening effects, in addition to the practical consequences of filter handling and possible misalignment. With the advent of computer controlled linear accelerators it has become possible to generate wedge shaped isodose distributions dynamically, thus providing a practical alternative to the standard physical wedge.

The dynamic wedge is created by moving one of the primary beam limiting collimators in a continuous fashion to create a continuously decreasing field width while the radiation beam is on. Because of this collimator motion, different segments of the treatment field will be exposed to the primary beam for different intervals of time. This process of shrinking the field width while modulating the collimator jaw velocity and dose rate creates the desired wedge-shaped isodose gradient across the treatment field. The amount of dose that is delivered to the patient as the collimator moves across the treatment field is controlled by pre-specified computer selected look-up tables.

Before a dynamic wedge option can be implemented clinically, it must be thoroughly tested by measuring pertinent beam characteristics, thereby determining the reliability of this technology. Unlike beam measurements in static field radiotherapy, dynamic beam radiatiotherapy requires the use of an integrating dosimetry technique. In this thesis data was accumulated with the use of film dosimetry and direct integration ionization chambers. Using such systems the dosimetric properties of the dynamic wedge installed on a dual energy Clinac 2300 C/D linear accelerator were investigated and the results reported in this thesis formed the basis for the clinical introduction of the dynamic wedge in the radiation oncology department of the Montreal General Hospital.

RESUME

La radiothérapie est un mode de traitement utilisé sur près de 50% des patients atteints du cancer. La radiothérapie par faisceaux de rayons externes consiste en plusieurs faisceaux convergeant en un endroit précis, le volume cible. L'anatomie du patient nécessite la modification des lignes d'isodoses afin de compenser pour le manque de tissue et la forme irrégulière du patient et du volume cible. Au cours des 40 dernières années, les filtres en coin conventionnels ont été utilisés pour contrer ces problèmes. Toutefois, ces filtres présentent quelques désavantages, tels le durciscement du faisceau et les possibilités d'erreurs lors des manipulations et du positionnement du filtre. Avec l'avènement des accélérateurs controlés par ordinateur, les filtres en coin conventionnels sont peu à peu remplacés par des filtres dynamiques.

L'effet de filtre dynamique est créé en translatant une des mâchoires du collimateur, afin de produire un champ de radiation dont la largeur diminue graduellement au cours de l'irradiation. Ainsi, différents segments du champ de traitement seront irradiés pour différent intervalles de temps. En modulant la vitesse des mâchoires et le débit de dose, il est possible d'obtenir des distributions de dose dont la forme est plus appropriée à un volume cible particulier.

Avant son utilisation clinique, un étalonnage complet du filtre dynamique doit être fait. Ceci est accompli en mesurant ses caractéristiques dosimétriques. La nature dynamique du filtre nécessite l'utilisation de techniques de mesure intégrée de la dose. Pour ce travail, donc, les mesures ont été obtenues en utilisant la dosimétrie par film et par chambre d'ionization. Ainsi, les propritétés du filtre dynamique du clinac 2300C/D ont été évaluées. Les résultats de cette étude, exposés dans cette thèse, constituent le point de départ pour l'introduction du filtre dynamique dans le département de radio-oncologie de l'Hôpital Général de Montréal.

ACKNOWLEDGMENTS

I would like to express my sincere gratitude for the guidance of my thesis supervisors Dr. E. B. Podgorsak and Michael D. C. Evans. Their time, patience, and sometimes overwhelming knowledge in the area of medical physics proved to be an invaluable resource during my studies at the Montreal General Hospital.

I thank the entire staff of the medical physics department, who answered many questions pertaining to this thesis and lent an open ear in times of need. Special thanks to Joe Larkin for making the complexities of linear accelerators seem understandable, and to William Parker for explaining some of the subtle uncertainties that I encountered in dosimetry measurements.

Many thanks are due to my office mates Corey Zankowski and Francois DeBlois, for giving great advice and easing my stress with their sense of humor. Also to my dear friend Adam Broughton for his generosity and heartfelt welcome during hard times.

Finally, I would like to thank my father Duncan A. Barry, my mother Diana M. Barry, and my brother Duncan L. Barry, for their unconditional love and emotional support.

This thesis is dedicated to my father Duncan A. Barry, who has always kept me travelling on the straight path.

TABLE OF CONTENTS

CHAPTER 3: CLINAC 2300 C/D ELECTRON LINEAR ACCELERATOR

CHAPTER 4: DOSIMETRY OF WEDGE FILTERS AND DYNAMIC WEDGES

CHAPTER 5: MEASUREMENT OF DOSIMETRIC DATA

AN INTRODUCTION TO RADIOTHERAPY

1.1 Basic aspects of radiotherapy

Radiation therapy, surgery, and chemotherapy are treatment modalities used in the fight against cancer. Radiation therapy and surgery are most often used for controlling localized disease whereas chemotherapy is mainly used for treatment of disseminated malignant disease. Approximately half of all new cancer patients are treated with surgery and the other half with radiotherapy.[1] Chemotherapy may be used in conjunction with either of the two treatment modalities.

In addition to the effort of saving the patient's life, maintaining the *quality* of life is a major goal of radiation therapy. When surgery is implemented there is a possibility of cosmetic disfigurement as well as gross loss of function. Examples of such deleterious effects can be noticed particularly in cases of head and neck cancer. Radiotherapy treatment is an effective alternative to surgery that allows the preservation of bodily function. Treatment of the female breast (for cosmesis), prostate (for preservation of sexual function), and bladder (for preservation of urinary function)[2] are examples of the advantages of radiotherapy over conventional surgical techniques.

When radiation therapy is employed, the primary concern is the delivery of a precisely defined dose of radiation to a predetermined tumor volume. Since radiation is not highly selective of just the tumor cells, healthy tissue surrounding the volume of interest will invariably be irradiated as well. Sparing this healthy tissue while monitoring the tumor dose is a major goal in radiotherapy treatments. In fact, damage to surrounding healthy tissue is the most important limiting factor in delivering tumoricidal doses in conventional radiotherapy. It follows that optimal radiotherapy treatments will minimize the dose to healthy tissues while maximizing the dose to the selected tumor volume.

1.2 High energy photons in radiotherapy

The discovery of x rays by Roentgen in 1895 established a new era in physics which led also to the practical applications of radiation in the medical field. It was soon established that x rays were a form of electromagnetic radiation whose wavelength was very much shorter than that of visible light. Quantum theory predicted that x rays would behave more like bundles of energy or photons rather than waves and that the quantum properties would become more noticeable as the wavelength decreased (or the frequency increased). The present day understanding of the interactions of photons with matter is based upon these quantum properties.

As a beam of photons impinges upon an object, such as the body of a patient, the photons (or quanta) undergo a variety of interactions which can be broadly categorized as attenuation, absorption, and scattering. *Attenuation* describes the decrease in intensity of a photon beam through absorption and scattering processes as it traverses the body. *Absorption* refers to the transfer of the incoming energy from photons to orbital electrons in the irradiated medium via the photoelectric effect, Compton effect, and/or triplet production. In pair production an electron/positron pair is created in the Coulomb field of the nucleus. The secondary charged particles that are set in motion, due to the absorption processes, travel through the medium losing their energy in the form of ionization, excitation, and heat resulting in biological damage. In medical applications of photons, the Compton effect is the predominant interaction process. The secondary photons that are generated by the Compton effect are usually referred to as *scattered* radiation (or simply scatter).

1.3 The purpose of this thesis

In many clinical situations involving external beam radiotherapy it is advantageous to use wedge shaped isodose contours. Until lately these "wedged fields" have been created with the use of physical wedge filters that are attached to the treatment head of the radiotherapy machine. These physical wedges suffer the dosimetric consequences of beam hardening as well as practical inconveniences of filter handling and placement uncertainties. Computer-controlled accelerators, such as the Varian Clinac 2300 C/D installed at the Montreal General Hospital, have the capability of creating wedged fields dynamically through controlled variations in dose rate and through upper collimator motion. This approach differs from conventional physical wedges since it requires no external beam modifiers. The resulting isodose shape is created through an integration of an open field and a field with a

continuously decreasing width. During the entire treatment process the dose rate and collimator velocity are modulated via computer control algorithms.

The difference between modern and conventional dose delivery techniques necessitates new procedures of clinical evaluation and implementation of dosimetric data for the dynamic wedge. A key requirement for dynamic wedge data accumulation is the integration of dose at a fixed point in the treatment field during the whole dose delivery sequence. This is carried out with the use of ionization detectors in the integral mode such as film or with direct integration using ionization chambers. With the help of such systems the dosimetric properties of the dynamic wedge were investigated to ensure that this technology can be implemented in our clinic on a routine basis. Results of our detailed study of the dynamic wedge installed in a Clinac 2300 C/D linac are reported in this thesis.

1.4 Thesis organization

Chapter 2 contains a short description of methods commonly used in medical physics for characterization of clinical photon beams. The difficulties involved in direct measurements of photon spectral distributions and other more practical means for describing the photon beam are also explained.

Chapter 3 provides a discussion of the Varian Associates Clinac 2300 C/D microwave linear accelerator used in our experiments. The operation of the Varian C-series system architecture, photon beam production, photon beam transport, radio-frequency generation, and radio-frequency transmission are explained in some detail.

In *Chapter 4*, the function and dosimetry of wedge filters and dynamic wedges in radiotherapy applications are discussed. Attention is given to the concepts of wedge angle, wedge factor, percentage depth dose, and wedged beam profiles. The dosimetric effects of conventional wedge filters on photon beams are shown and explained. The operation of the Varian dynamic wedge is also described.

Chapter 5 explains the dosimetric systems for measuring the characteristics of photon beams. The main topics are: dosimetric phantoms, ionization chambers, water tank scanners, and film dosimetry.

The results of our experiments are presented and discussed in *Chapter 6*, while the conclusion of this thesis and possible future developments in implementations of the dynamic wedge are provided in *Chapter 7*.

1.5 References

1. R. Silverman, J. Distasio, Radiation Therapy with Heavy Particles and Fast Electrons, Noyes Data Corporation, New Jersey, U.S.A. (1980).

2. C.J. Karzmark, C.S. Nunan, E. Tanabe, Medical Electron Accelerators, McGraw-Hill, Inc. (1983).

PHOTON BEAM PARAMETRIZATION

In the therapeutic applications of radiation it is crucial to be able to predict the behavior of the photon beam within the patient. With accurate knowledge of pertinent photon beam parameters, such as beam quality, beam penetration into absorbing media, beam profiles, and machine output, it is possible to calculate and analyze the dose distribution anywhere in the patient before the treatment is actually given.

2.1 Beam quality

A photon beam is not described completely by stating an exposure or dose that it delivers to a small region of an irradiated medium. Although such quantities have an important clinical significance, they do not sufficiently characterize the *penetrability* of the photon beam in question. For this reason the concept of beam quality has been introduced. The quality of a photon beam can be inferred from measurements of the beam's penetration in various media and is directly related to the energy of the beam. The quality of the photon beam is essential for making proper estimates of the exposure or dose at other locations within the irradiated medium, of differences in energy absorption at inhomogeneous interfaces within the medium (e.g., soft tissue and lung), and of the biological effectiveness of the radiation itself.

The quality of a photon beam can be described most explicitly by the spectral distribution of the beam. The *spectral distribution* provides the relative number of photons per unit energy interval contained in a photon beam. For low output orthovoltage x-ray machines (300 kVp or less) it is possible to measure the spectral distribution directly with scintillation spectrometers, which use sodium iodide (NaI) or germanium-lithium doped (GeLi) crystals. When such a crystal is irradiated each absorbed photon produces a pulse of light, which is channeled through a photomultiplier tube and converted into a voltage signal with a height proportional to the total absorbed energy. After suitable amplification the voltage pulses are sent to a pulse height analyzer where they are sorted according to their magnitude. The pulses are then recorded in 400 or more different channels, each channel

representing a different photon energy. The number of counts in each channel corresponds to the number of photons detected in a particular energy interval.

Since these spectrometers detect the total energy deposited by every incident photon and cannot analyze a second photon until the signal from the former one has been processed, there is an intrinsic limitation on the number of photons per unit time that the detector can count.[1] To reduce the rate of photons reaching the spectrometer to an acceptable value, the photon beam is commonly passed through a small pinhole aperture and measurements are taken at a distance of 10 m from the source. This technique requires great care since the pinhole can introduce scatter artifacts. Moreover, because of the 10 m separation, the resulting spectrum must be corrected to account for the photon attenuation in air.

Another way to overcome the counting rate problem is to pass the photon beam through a thin foil of known composition and use a spectrometer to measure the radiation that is Compton-scattered at an angle of 90^{o}. Since the number of scattered photons at this angle is about three orders of magnitude lower than the number of primary photons incident upon the foil, the counting rate can be reduced by an order of 1000. The original photon spectral distribution can then be reconstructed from the measured data by application of the Klein-Nishina formula.[2] This method is effective but introduces uncertainties that have a tendency to degrade the energy resolution.

In light of the counting rate limit on spectrometers, spectral distribution measurements are not possible with medical linear accelerators because the photon fluence rate produced by these machines is excessively high. Additionally, the scintillation crystal used in the spectrometer cannot be made large and deep enough to fully absorb the highly energetic photons. Considering that the one-to-one correspondence between the photon energy and scintillation output depends upon the total absorption of the photons incident on the spectrometer, direct spectroscopic measurements of high energy photons are very inefficient.[2] As a result, simpler alternatives based on penetrability measurements in a known absorbing material are used to characterize the quality of high energy photon beams used in medical physics and radiotherapy.

One method for describing the quality of photon beams is through half-value layer (*HVL*) measurements. The *HVL* is the thickness of absorber material that reduces the incident photon beam intensity (or exposure rate) to half of its original value as measured with a dosimeter calibrated to read roentgens[3] (or Kerma in air). When a monoenergetic photon beam travels through an attenuator (e.g., lead) it will be attenuated exponentially according to the following relationship:

$$I(x) = I_o \cdot e^{-\mu(E) \cdot x} \quad , \tag{2.1}$$

where $I(x)$ is the intensity of the photon beam after passing through a thickness x of the attenuator material, $\mu(E)$ is the linear attenuation coefficient of the attenuator material for photon energy E, and I_o is the incident photon beam intensity. The *HVL* can be found simply by letting $I(x) = 0.5\ I_o$. Under this condition it follows that:

$$HVL = \frac{0.693}{\mu(E)} \quad , \tag{2.2}$$

It is evident that by measuring the *HVL* one can calculate the linear attenuation coefficient $\mu(E)$ and find the corresponding energy of the photon beam from tables relating μ and E. It should be noted that for a monoenergetic photon beam (e.g., Co-60) the first half-value layer (*HVL1*) is equal to the second half-value layer (*HVL2*), where *HVL2* is the thickness of material required to reduce the photon beam from 50% to 25% of its original intensity after it has travelled through the distance *HVL1*.[4] For polyenergetic photon beams (from linear accelerators) *HVL1* will generally be less than *HVL2* since low energy photons are preferentially attenuated by the attenuator. The result is that polyenergetic beams become increasingly harder (more penetrating) as the attenuator thickness increases. The ratio *HVL2/HVL1* is referred to as the heterogeneity coefficient and is equal to 1 for monoenergetic photon beams and is larger that 1 for heterogenous photon beams.

Unfortunately, for megavoltage radiotherapy machines, the *HVL* is not a reliable parameter for characterizing photon beam quality because the linear attenuation coefficient does not change rapidly with energy at high photon beam energies. Therefore, a small change in the value of the attenuation coefficient results in a large change in the effective beam energy. The *HVL* technique is most appropriate for orthovoltage machines since at orthovoltage energies the attenuation coefficient changes rapidly with energy.

A more convenient way to characterize a photon beam is by measuring the *percentage depth dose* (*PDD*) in a phantom material. This quantity is measured most easily inside a water phantom using an ionization chamber. Even though other dosimetry systems, such as thermoluminescent detectors (TLDs), diodes, and film can be used, ion chambers are preferred because of their better precision and smaller energy dependence. The *PDD* relates, in the form of a percentage, the dose at any depth d along the central axis of the

beam to the maximum dose measured at a given depth d_{max} on the same axis. This can be represented mathematically as follows:

$$PDD\,(d, FS, SSD, E) = \frac{D\,(d, FS, SSD, E)}{D\,(d_{max}, FS, SSD, E)} \times 100 = \frac{D_Q}{D_P} \times 100 \quad , \qquad (2.3)$$

where d is the depth of interest below the phantom surface, d_{max} the depth of maximum dose, SSD is the source-surface distance, FS is the field size at SSD, E is the energy of the incident photon beam, and D_Q and D_P are doses at depths d and d_{max} in phantom, respectively, as shown schematically in Fig. 2.1.

For megavoltage photon beams the PDD follows a characteristic behavior, increasing from a low value on the phantom surface to a broad maximum (100%) at d_{max} and then decreasing essentially exponentially with increasing depth, as shown schematically in Fig. 2.2. The region of the initial increase in dose between the surface and d_{max} is called the *buildup region*. For megavoltage photon beams the dose at d_{max} is substantially greater than the surface dose. This offers a distinct advantage over lower energy orthovoltage beams where d_{max} occurs essentially on the surface. Thus, in the case of megavoltage photon beams, higher doses can be delivered to deep seated tumors without exceeding the limiting skin tolerance level. This is known clinically as the *skin sparing effect.*

The physics that leads to the buildup region can be explained as follows: when the photon beam enters the phantom, secondary electrons are set in motion from the surface and from deeper layers. These electrons travel away from their point of origin until all of their energy is dissipated in the absorbing medium. The result is an electron fluence that attains a maximum value at the depth d_{max}. Since the absorbed dose is proportional to the electron fluence, the PDD increases until a maximum is reached at d_{max}. Beyond d_{max} the PDD decreases in an approximately exponential fashion as a result of the photon fluence attenuation in the absorbing material.

From Fig. 2.3 which shows PDD curves for Co-60, 6 MV, 10 MV, and 18 MV photon beams (SSD = 100 cm, FS = 10×10 cm^2) it can be seen that, as the photon energy increases, the depth of dose maximum increases for same field size and SSD, and that the beam becomes more penetrating at a given depth beyond d_{max} for the same field size and SSD. Photon beams also become more penetrating with increasing SSD for the same field size and depth. This is attributed to the inverse-square law dependence of the photon beam which becomes less influential with depth as the source is moved further away from the surface.

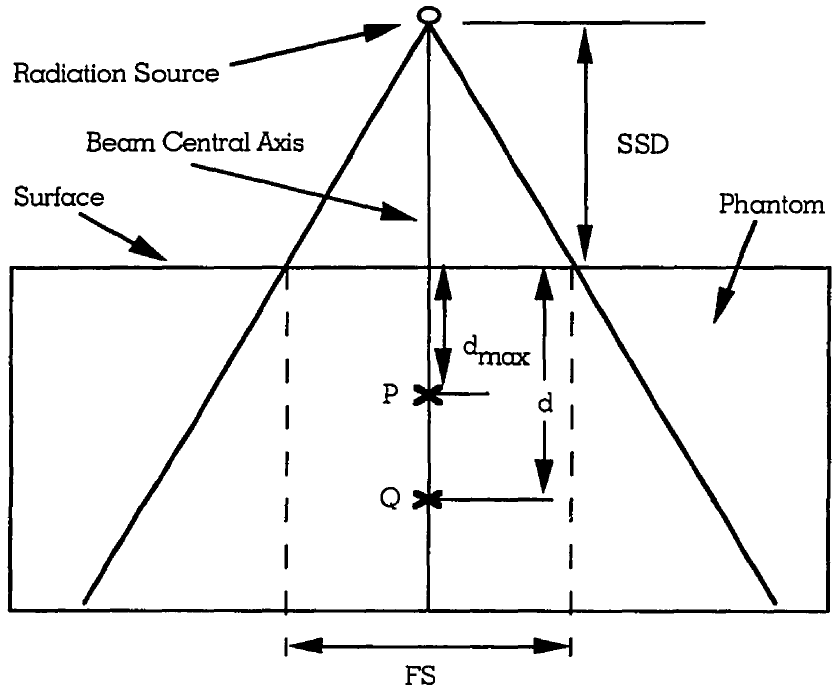

FIGURE 2.1. ***Illustration of an SSD setup that characterizes the PDD. D_Q is the dose to point Q at an arbitrary depth d and D_P is the dose to point P at the depth of maximum dose d_{max} on the beam central axis for a fixed source-surface distance (SSD). FS is the field size at SSD.***

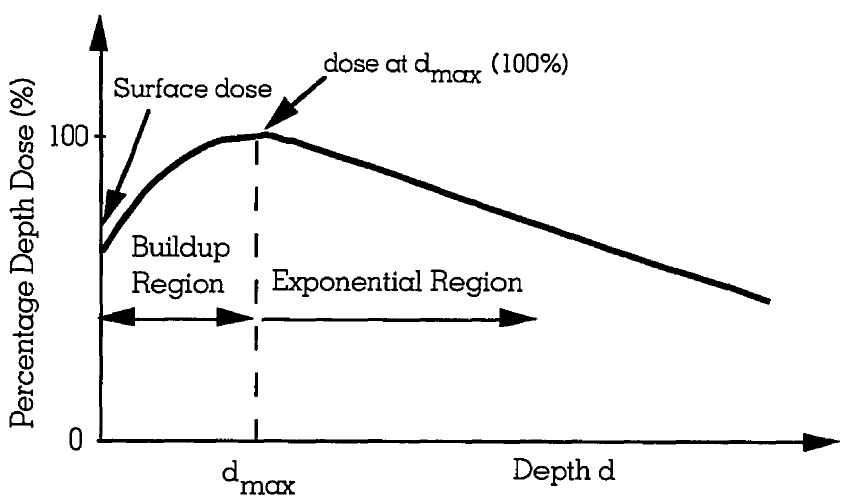

FIGURE 2.2. ***Diagram illustrating typical characteristics of a photon beam percentage depth dose curve.***

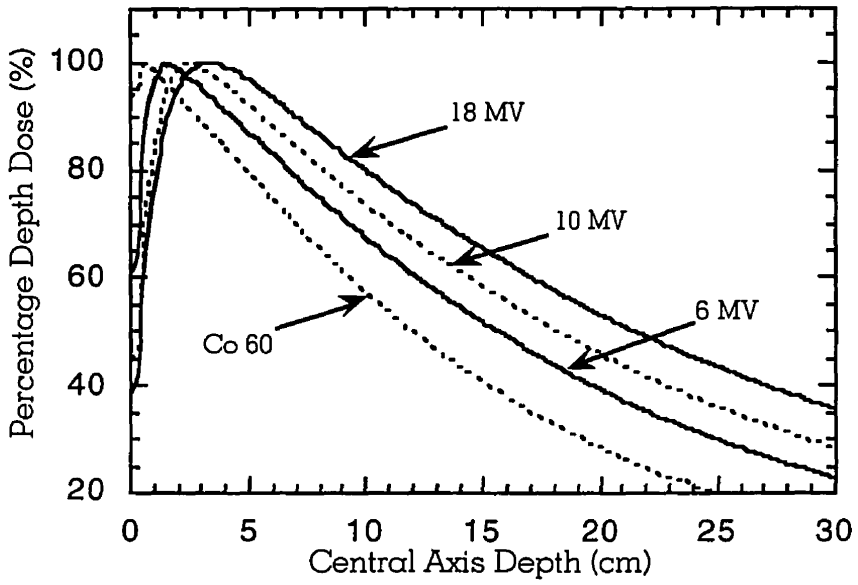

FIGURE 2.3. ***Typical PDD curves in water for of Co-60, 6 MV, 10 MV, and 18 MV photon beams for a field size of 10×10cm^2 and an SSD of 100 cm.***

The build-up region can be explained by noting the difference between *kerma* (*k*inetic *e*nergy *r*eleased in the *m*edium) and *absorbed dose*, as illustrated in Fig. 2.4. Kerma has a maximum at the surface and decreases with depth due to the decrease in photon energy fluence. The absorbed dose, on the contrary, first increases with depth due to secondary electrons set in motion that travel deeper into the medium. This leads to an electron fluence that increases with depth (i.e., electronic buildup). This electron fluence will eventually reach a maximum around the same depth as the corresponding electron range in the medium.[4] Since the absorbed dose is proportional to the electron fluence, it will also reach a maximum at this depth. After this depth the absorbed dose will decrease with kerma because of photon attenuation and the resulting reduction in electron fluence. A closer look at Fig. 2.4 reveals that the kerma curve is initially greater than the absorbed dose curve. However, the kerma curve falls below the absorbed dose after the buildup region. This discrepancy results from the fact that the areas under each curve are equal if taken to infinity.

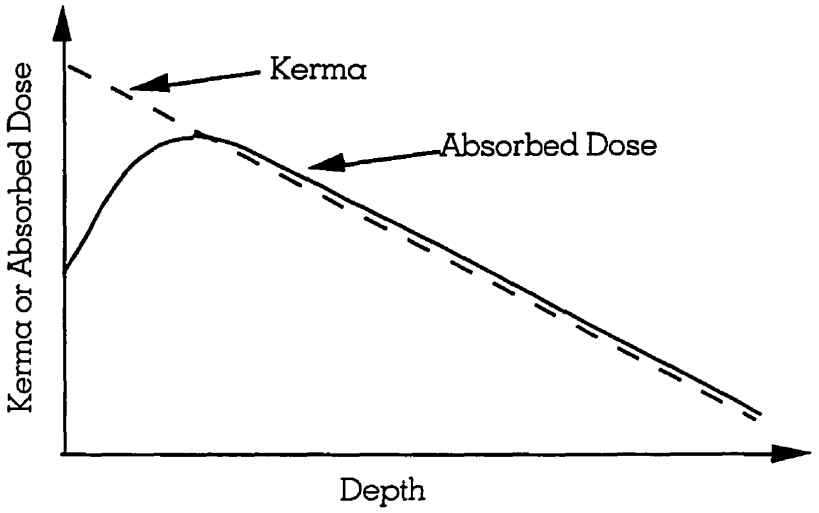

FIGURE 2.4. ***Plot of absorbed dose and kerma as functions of depth in phantom.***

2.2 Dose profile

The *dose profile* shows the variation of the dose in a particular irradiated medium perpendicularly to the beam central axis. The dose values off center are normalized to 100% of the corresponding dose value on the central axis at d_{max}. Such dose profiles are measured at the center of the field, along the field width or length, where the profile is symmetric about the beam central axis. An example of dose profiles for a 6 MV photon beam at various depths in water is shown in Fig. 2.5. As the depth in phantom increases, the edges of the dose profiles start to round off. This effect has two causes. The first is the obliquity of the photon beam at the field edges. Photons on the edge of the field have to travel greater distances in the phantom to reach the same depth as the photons on the central axis of the beam. According to the inverse square law, the points on the edge of the field receive less dose than the points on the central axis. The second reason for the rounding is the effect of the flattening filter found inside the head of the linear accelerator. The flattening filter is a nearly conical-shaped filter made out of iron, tungsten, or copper, that is used to shape the photon beam to produce an approximately flat dose profile at a depth of 10 cm in a tissue equivalent phantom. It is thickest along the central axis of the photon beam and therefore preferentially attenuates lower energy photons at the center. The photons at the field edges have a greater number of low energy photons that are easily attenuated at the field edges, causing noticeable rounding of the dose profiles as the depth increases. The dose profile is a function of beam energy, field size, depth in phantom, and *SSD*.

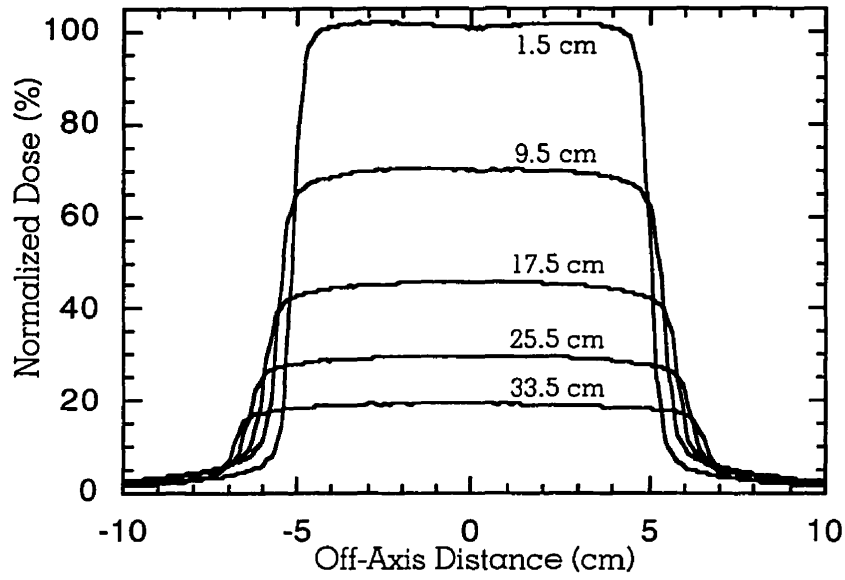

FIGURE 2.5. ***Dose profiles for a 6 MV 10 ×10 cm^2 photon beam at depths of 1.5 cm, 9.5 cm, 17.5 cm, 25.5 cm, and 33.5 cm in water. The SSD is 100 cm.***

2.3 Absolute dosimetry and beam output

There are three types of absolute dosimetry techniques that can be used to determine the output of radiotherapy machines. These are: *calorimetry*, *chemical dosimetry*, and an exposure calibrated *ionization chamber*.

Calculation of machine output using calorimetry techniques takes advantage of the fact that when a medium is irradiated, most of the energy absorbed will give rise to heat resulting in an increase in temperature. This increase in temperature, with knowledge of the specific heat and mass of the absorbing medium, can be directly related to the absorbed dose in the calorimeter. The change in temperature is found with the help of thermistors, which are semiconductor devices that exhibit a substantial change in resistance for temperature increases on the order of 1 degree. Even though calorimeters are an elegant means for determining the dose to a medium, they are limited in their clinical use because the heat generated in a medium by typical clinical doses of radiation is minute, and the resulting increase in temperature is much too small to be measured with precision without highly sophisticated and cumbersome techniques available only in standards laboratories.

In chemical dosimetry the energy absorbed by irradiation of a chemical substance may produce a chemical change in the absorbing medium. One of the most common chemical radiation dosimeters is the Fricke dosimeter which depends upon the change of an aqueous solution ferrous sulphate (Fe^{2+}) to ferric sulphate (Fe^{3+}) ions. The amount of ferric sulphate ions produced in the solution can be measured by absorption spectrometry techniques in which the amount of ultraviolet light (304 nm) absorbed by ferric ions can be directly related to the absorbed dose in the Fricke solution. The Fricke solutions exhibit radiological properties very similar to those of human tissue. However, Fricke solutions are not useful for measuring doses lower than about 10 Gy because at these doses only small amounts of ferric ions are produced making it difficult to measure precisely the differences in ultraviolet absorption of the irradiated and unirradiated solutions.[3]

The most practical method for determining the dose in an absolute manner is based on an exposure calibrated ionization chamber. In order to calibrate an ionization chamber to be used in the clinic, it must be sent to a standardization laboratory which possesses a standard free-air ionization chamber. The standard free-air ionization chamber enables one to determine the exposure calibration factor N_x of the ionization chamber. Once N_x is found, any reading M obtained with the ion chamber, corrected for temperature, pressure, and ionization recombination loss, will yield the exposure X. Using an appropriate protocol, such as the TG21[5], this calibrated exposure reading can be used to calculate the absolute dose imparted to a medium at a suitable depth in a tissue equivalent phantom.

Of the three techniques listed above only calorimetry is absolute in the sense of true absoluteness. Both Fricke dosimetry and ionization chambers depend on agreed upon values for various physical parameters; Fricke dosimetry upon the G-value (number of Fe^{3+} ions produced per 100 eV of absorbed energy) and ionization chambers upon $\overline{W}_{air}$ (average energy required to produce an ion pair in air). Since these values are subject to change with refinements in measurement techniques, they put the "absoluteness" of Fricke and ionization chamber dosimetry in question.

The *beam output* of a radiotherapy machine is defined as the absolute dose measured at d_{max} in phantom with the phantom surface placed at the nominal machine SSD of 100 cm. The radiotherapy machine used in our experiments is calibrated, using the TG21 protocol, to deliver 1 cGy per monitor unit (MU) at the depth of d_{max} for a reference field of 10×10 cm^2. The output increases as beam energy and field size increase. The Varian Clinac 2300 C/D linear accelerator installed in our department is calibrated twice a week to ensure that the beam output used in patient dose delivery is accurate.

2.4 References

1. E. Segre: Nuclei and Particles, W.A. Benjamin, Inc., New York (1965).

2. M. Yaffe, K.W. Taylor, H.E. Johns: *Spectroscopy of diagnostic x rays by a Compton-scattered method*, Med. Phys. **3**, 328-334 (1976).

3. H.E Johns, J.R. Cunningham: The Physics of Radiology, 4th edition, Charles C. Thomas, Springfield, Illinois, U.S.A. (1983).

4. F.M. Khan: The Physics of Radiation Therapy, 2nd edition, Williams & Wilkins, Maryland, U.S.A. (1994).

5. TG21, *A new protocol for the determination of absorbed dose from high-energy photon and electron beams*, Med. Phys. **10**, 741-771 (1983).

CLINAC 2300 C/D ELECTRON LINEAR ACCELERATOR

3.1 Introduction

The computerized Varian C-Series, high energy Clinac model 2300 C/D radiotherapy linear accelerator (linac) used at our institution has the capability of generating 6 MV and 18 MV megavoltage photon beams in addition to electron beams ranging from 4 MeV to 22 MeV. It is isocentrically mounted and can produce photon field sizes ranging from 0.5×0.5 cm^2 to 40×40 cm^2 at a source-axis distance (*SAD*) of 100 cm. The therapy dose rates vary from 100 MU (Monitor Units) to 600 MU per minute in six fixed steps for photon and electron beam treatments.

The C-Series integrated control system makes the machine simple to operate and monitors the overall performance of the Clinac 2300 C/D. Under the direction of the C-Series Control system, a color video monitor displays a series of screens that guide the operator through the appropriate steps to set up and perform patient treatment. This control system also continuously monitors the overall operation of the machine. If the machine is not operating properly, one of the interlocks is enabled that terminates the photon beam or prevents the beam from firing.

3.2 Major linac components

The major components of the high energy Clinac 2300 C/D are: the operator console, console electronics cabinet, modulator cabinet, drive stand, and gantry.

3.2.1 Operator console

The operator console is used to input all operator commands and consists of a high resolution color monitor and a dedicated keyboard. The monitor displays the treatment parameters that have been entered via the dedicated keyboard. Some of the important parameters shown are the selected photon energy, dose, dose rate, time, gantry angle, field size, and other pertinent information. The dedicated keyboard is also used to start and terminate the beam and control the mechanical motions. In addition, the keyboard incorporates an emer-

gency button which, when pressed, will shut down all system power. If the operator chooses to use the Clinac 2300 C/D in the service mode, a separate alphanumeric keyboard must be used to control the linac operation. In the service mode the operator may disable specific interlocks and servo mechanisms.

3.2.2 C-Series control electronics cabinet

The electronics cabinet houses the console computer, control processors, signal conditioning electronics, and the Varian card rack. The console computer processes the commands from the keyboards and outputs data on the video monitor. The control processors execute commands that are downloaded from the console computer, update machine status information, and prevent beam generation if interlocks are enabled. The control processors send and receive information through the signal conditioning electronics, while the Varian card rack contains the energy program boards for mode control and calibration.

3.2.3 Pulse modulator cabinet

The modulator cabinet contains the high voltage power supply (HVPS), the pulse forming network (PFN), a voltage regulator (deQing circuit), and thyratron tubes. The PFN is charged to a voltage and then released by the deQing circuit. This high voltage is sent to a step up transformer in the drive stand and applied to the klystron amplifier.

3.2.4 Drive stand

The drive stand (Fig. 3.1) contains the radio-frequency (rf) driver, klystron, and the PFN pulse transformer. It also contains the waveguide system that transports the rf power from the klystron to the accelerator structure through a rotary joint. The stand also includes the dielectric gas system, a water tank and pump for water cooling, as well as various power supplies. There is also an auxiliary electronics chassis at the top of the stand that contains the circuitry to drive the motor for all system motions. The drive stand is also used to support the gantry.

3.2.5 Gantry

The gantry (Fig. 3.1) contains the Clinac 2300 C/D accelerator structure, electron gun, energy switch, vacuum system, automatic frequency control (AFC) system, bending magnet electron transport system, and the beam shaping system.

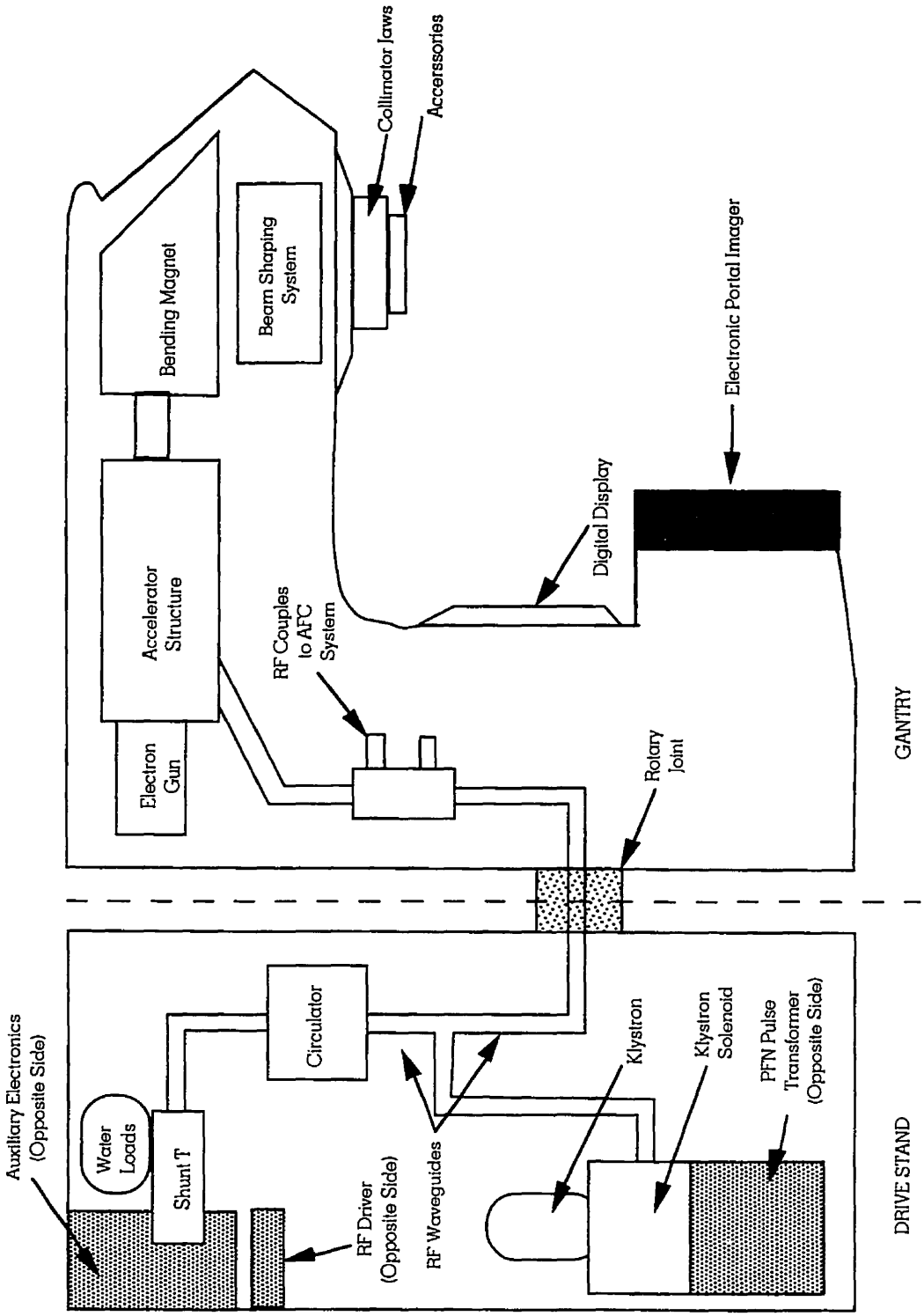

FIGURE 3.1. ***Schematic diagram of the Clinac 2300 C/D drive stand and gantry.***

The gantry can be rotated 180° clockwise or counterclockwise from the vertical position for a total of a 360° rotation. Therefore, the treatment head may be positioned at any desired angle during treatment. The gantry angle is displayed, along with the collimator angle and field size, on a digital display on the center of the gantry and also on the console computer video monitor. The lower part of the gantry comprises of a counter-weight and also holds a Varian electronic portal imager.

3.3 Functional systems

The Clinac 2300 C/D has to execute many functions in order to produce a megavoltage photon beam with a specific energy. Electrons must be injected into the accelerator structure at exactly the right moment to ensure that they will be accelerated by the standing wave field patterns created by the Clinac 2300 C/D accelerator structure. The kinetic energy acquired by these accelerated electrons is used to create a photon beam by placing a target into the electron beam path. Once this photon beam is created, it must be collimated and accurately directed towards the patient. For dosimetric purposes, the beam intensity must be constant and uniform throughout the prescribed treatment field. Also, the dose delivered to the patient must be precisely monitored and an easy method for terminating the beam when the desired dose has been given should be employed.

The Clinac 2300 C/D accomplishes the above treatment goals with the use of the primary and support systems discussed below. The C-series control electronics system monitors and coordinates the interaction among the various system components and orchestrates the overall operation of the machine.

3.4 Generation of triggers

The process of accelerating injected electrons from the gun through the accelerator is by no means a simple one. In order for the electrons to be accelerated efficiently, certain system component activities must take place. All of these activities cannot occur at the same time. For this reason the various components responsible for the operation of the Clinac 2300 C/D are synchronized by timing signals, otherwise known as *triggers*, that are sent by the control processor. These pulses are 5 μs wide and occur at a specific time interval after the system clock pulse which has a frequency of 360 Hz.[1]

3.5 Energy selection control signals

When the operator selects the desired x-ray beam energy on the Clinac 2300, the Control processor outputs the required energy selection control signals. The primary output is a binary-coded decimal (BCD) code which uniquely defines the chosen photon energy. A BCD code of 1 (i.e., 001) will select the 18 MV photon mode, and a BCD code of 2 (i.e., 010) will select the 6 MV photon mode.[1] Each BCD code selects a program board found in the Varian card rack. There is a unique program board for each chosen energy. The BCD also programs the carrousel control microprocessor, housed in the auxiliary electronics chassis, to insert the appropriate target into the beam for a given photon mode. The carrousel controller is also responsible for the alignment of the appropriate flattening filter in the beam path. It also oversees the positioning of the shunt T and reduces the beam steering current limit when the 6 MV mode is chosen.

3.6 Electron injection

Electrons are injected into the accelerator structure from a triode electron gun which consists mainly of a heater, cathode, focusing electrode, a control grid, and an anode, as shown in Fig. 3.2. Electrons are thermionically emitted from the heated cathode surface and then accelerated through a potential difference between the cathode and the anode. The cathode is kept at a very high negative DC voltage. The accelerator guide itself, which

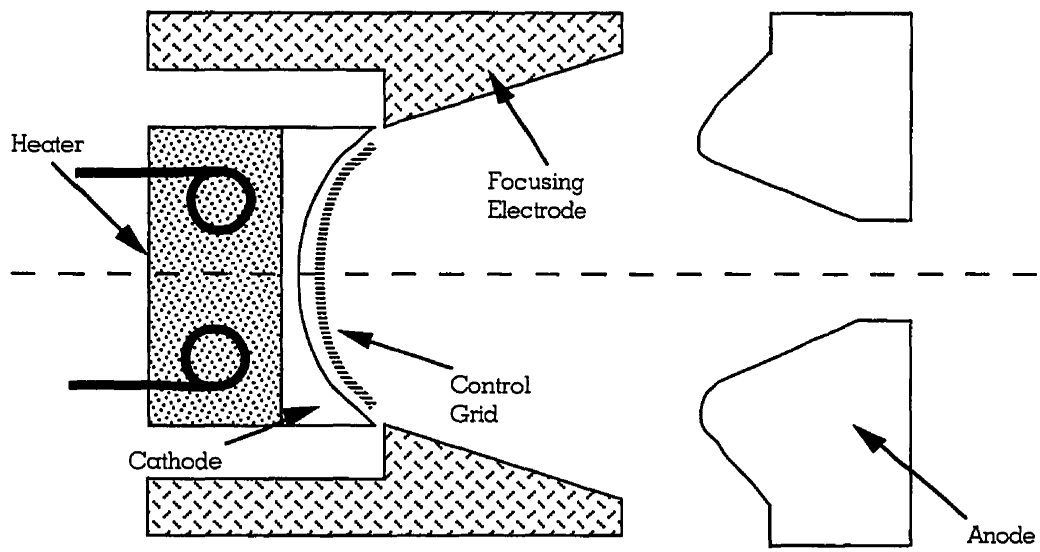

FIGURE 3.2. ***Schematic diagram of the triode electron gun structure used in the Clinac 2300 C/D.***

stays at ground potential, acts as the anode. As the electrons are accelerated between the cathode and the anode they experience electrostatic repulsion. The electron beam thus experiences a divergence and a resulting decrease in current density.[2] For this reason, electrostatic focusing is employed through the use of a focusing electrode. The focusing electrode is designed to counteract the electron beam divergence and helps focus the beam through the exit hole found in the anode. The control grid prevents the electrons emitted from the cathode from reaching the anode and is kept at -100 V with respect to the cathode. Electron injection is allowed only when the control grid is triggered by a 3.5 μs pulse that is positive with respect to the -100 VDC gun grid bias.[1] The trigger pulse ranges in magnitude from -80 V to +150 V, depending on the gun current required for the selected energy. Typical beam currents in electron guns are 30 mA to 50 mA. The control grid can be triggered by a klystron-coincident pulse or a gun delay pulse.

The mode BCD that is received from the Control processor is decoded on a board found in the gun driver. The decoded signal is used to select the appropriate cathode voltage. This DC voltage will range from -3.5 kV to -20 kV. The control grid voltage is controlled by a different board also found in the gun driver. The 18 MV and 6 MV beams require different cathode voltages and filament current levels to produce the necessary beam current.

3.7 Radio-frequency (rf) generation

The Clinac 2300 C/D standing wave accelerator structure uses pulses of high power rf energy (i.e., 2856 MHz microwaves) to create an electric field distribution that will accelerate injected electrons to a specific kinetic energy. The klystron, which uses a high voltage pulse from the pulse modulator, generates the rf pulses by amplifying low level rf signals produced by the rf driver. The magnitude of the rf signals necessary to establish the required field strength depends upon the selected beam energy. The rf generation process is made possible by the use of the pulse modulator, rf driver, and klystron. Since these systems play such a crucial role in the injected electron acceleration process, they will be discussed separately.

3.7.1 Pulse modulator

The pulse modulator (Fig. 3.3) generates a pulsed high voltage (HV) waveform that is sent to the klystron. This pulse is formed by a pulse forming network (PFN) housed in the modulator cabinet. The HV pulsed waveform is then directed to a transformer found in the

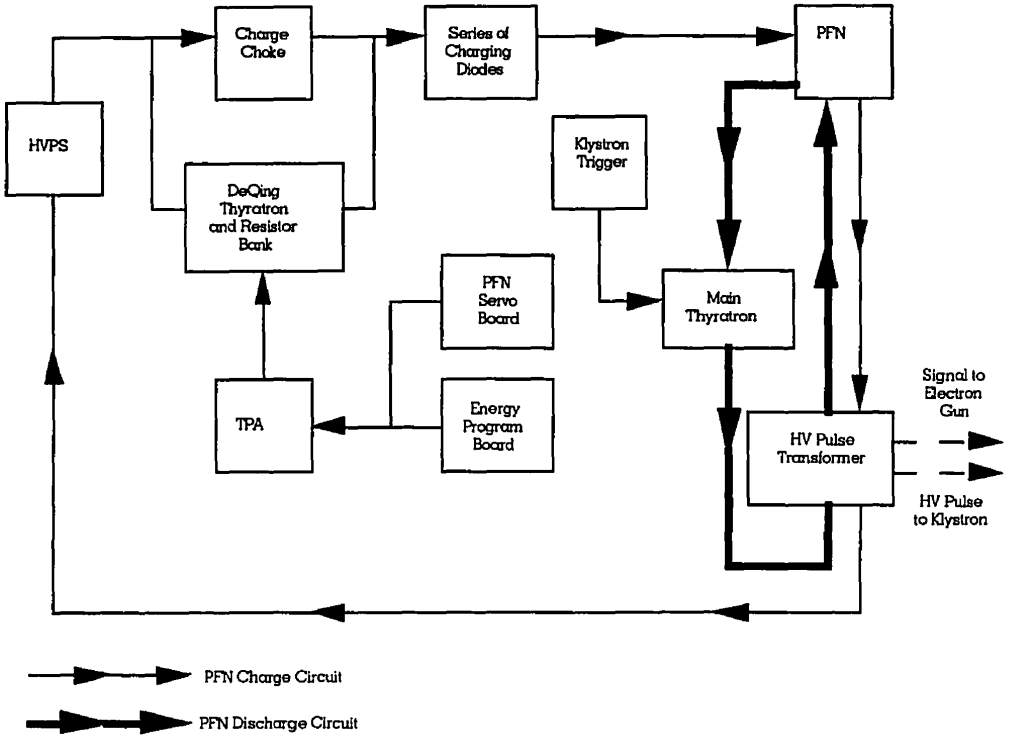

FIGURE 3.3. ***Block diagram of the Clinac 2300 C/D pulse modulator.***

drive stand. This transformer will step up the voltage and send it to the cathode of the klystron amplifier.

The PFN is charged by a high voltage power supply (HVPS). The HVPS is formed by sending the 3-phase (3-ϕ) input line voltage through a 3-ϕ power transformer which produces a rectified and filtered 6-ϕ output with a negligible ripple voltage. Since the ripple voltage is extremely small, the output can be considered essentially DC. For the Clinac 2300 C/D this output is 11 kVDC (at 2 A) for the 6 MV mode and 13 kVDC (at 1.3 A) for the 18 MV mode. When the desired beam energy is chosen, the C-series Control processor selects the appropriate HVPS output by sending a mode command (Mode A for 6 MV and Mode B for 18 MV) to the 3-ϕ high voltage transformer. These mode commands will set the position (high or low) of the high voltage transformer tap which allows the selection of different line voltage inputs.

The current from the HVPS is sent to an array of inductors and capacitors in the *PFN* through a charging choke. Initially, the inductive reactance of the charge choke prevents

current flow and all of the HVPS voltage is dropped across the charge choke. As the inductive reactance is overcome, current starts to flow through the choke creating a strong magnetic field in the core of the choke and charging the capacitors in the PFN. When the PFN charge voltage is equal to the HVPS, the current flowing through the charge choke becomes steady state and the magnetic field in the core of the choke starts to collapse.[3] This choke magnetic field collapse induces a voltage across the choke which adds to the HVPS voltage. This new voltage keeps current flowing into the PFN capacitors and essentially doubles the HVPS voltage. A series of charging diodes prevents the energy stored in the capacitors from flowing back into the HVPS. The capacitor array is charged to a certain limit which is determined by commands sent from the energy program board. When the PFN reaches this limit it abruptly reduces the "*Q*" of the circuit. The *Q* is a measure of the relationship between the stored energy and the rate of dissipation. This reduction of *Q* is commonly called "deQing" and is achieved by triggering a thyratron (i.e., deQing thyratron). The trigger pulse sent to the deQing thyratron is amplified by a trigger pulse amplifier (TPA) to produce a high voltage firing pulse. When the deQing thryraton is fired, the current that charges the capacitor array is diverted to a resistor bank that is in parallel with the charge choke. As a result, the charge choke voltage becomes less than the potential on the charging diodes, thereby preventing the PFN from charging. This method sets the Clinac C/D PFN voltage within a range of 18 to 24 kVDC.

At a specified time a klystron timing pulse is sent by the Control processor. This trigger pulse is amplified by the trigger pulse amplifier (TPA) and then used to fire the main thyratron. When this occurs the energy stored in the PFN is discharged through a step up klystron pulse transformer. This transformer steps up the voltage by a factor of 11. The klystron transformer delivers a 5.8 μs pulse with an amplitude that varies with the stored PFN energy.

3.7.2 RF driver

The rf driver is used to produce medium power rf pulses (50 - 350 W_{peak}) at the klystron input port. These pulses are injected at almost the same time as the *HV* klystron transformer pulse is received at its cathode. The rf driver is triggered before the klystron to make sure its output is stable when the klystron is triggered. The rf driver pulse is 12μs in duration.[1] This implies that the rf driver remains on during the entire klystron pulse which has a shorter duration. The driver operates on a center frequency of 2856 MHz. If the frequency of the rf power entering the accelerator structure deviates from the resonant frequency of the accelerator guide because of changes due to temperature effects, the rf

driver frequency will be servoed by the AFC (automatic frequency control) to within ±1 MHz to compensate.[1]

The driver output depends upon the selected energy mode. For 6 MV photons (Mode A) the output power is 160 W to 220 W. For 18 MV photons (Mode B) the output power is 80 W to 120 W.[1] The rf driver output is adjusted so as to ensure that the klystron is operating in its saturation region.

3.7.3 Klystron amplifier

The Clinac 2300 C/D klystron amplifier consists of three separate sections: the electron gun, rf section, and the collector section. The klystron electron gun works on the same principle as the Clinac 2300 C/D electron gun. In the operation of a klystron, accelerated electrons pass through a series of resonator cavities. The Clinac 2300 C/D uses a four cavity klystron, shown schematically in Fig. 3.4. The resonator cavities are separated from each other with zero field metal tubes known as *drift tubes*. In the klystron, a waveguide is used to couple a low level rf input with the first resonator cavity (i.e., buncher cavity). This rf input will induce an oscillating electric field inside the buncher cavity which alternates at the rf frequency. For one half cycle the electric field will speed up electrons; on the other half of the cycle it will slow down electrons. This process is known as *velocity modulation.*[4]

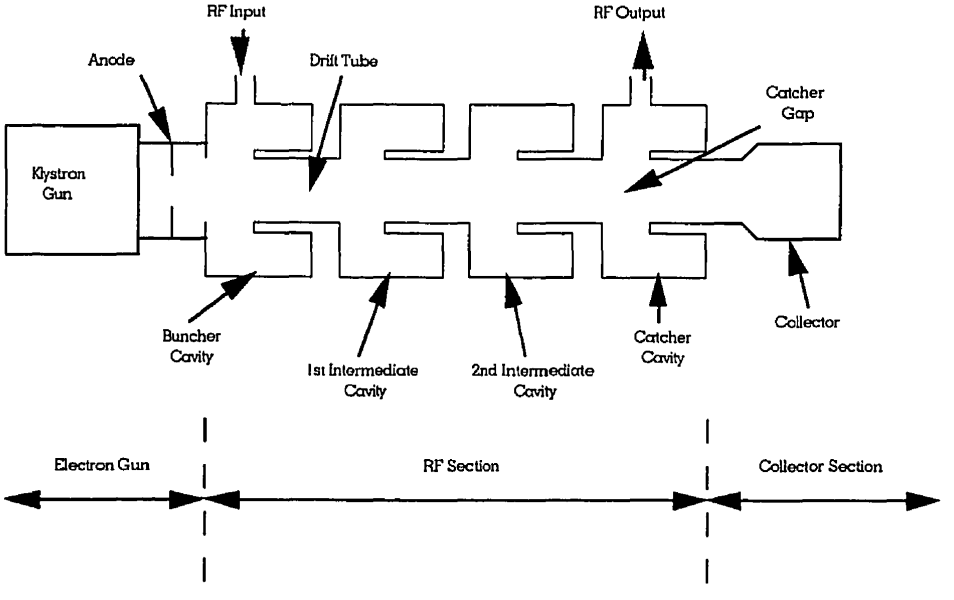

FIGURE 3.4. ***Schematic diagram of the Clinac 2300 C/D four-cavity klystron amplifier.***

After exiting the buncher gap the electrons enter into the drift tube region. In the drift tube the electrons that are traveling faster will overtake the electrons that have been previously slowed down. Since some electrons are overtaking other electrons, *bunches* will be formed. The electron bunches will then traverse the two intermediate cavities which improve the bunching process thereby increasing amplification and efficiency. The bunches then cross the output cavity gap where they generate large oscillating currents within its walls. This results in an amplified rf output that is coupled to the output waveguide from the klystron.

3.8 RF transmission

The rf system used in the Clinac 2300 C/D is shown in Fig. 3.5. Initially, the power derived from the klystron is sent to the accelerator structure through a hollow rectangular waveguide. This forward rf is directed through a four-port circulator where it is sent to a magic T assembly. The magic T deflects a preset portion of rf into a water load and reflects the rest of the rf back to the four-port circulator. The rf is then channeled to the accelerator structure for use in producing the electron beam. Any reflected rf power from the accelerator structure is sent back to the circulator where it is channeled to a second water load to prevent it from going back to the klystron. The forward and reflected rf are monitored in the waveguide for use by the automatic frequency control (AFC) system. Since rf transmission is crucial in producing an x-ray beam, the major components that make it possible are discussed below.

3.8.1 Waveguides

Hollow rectangular (or cylindrical) pipes can be used to transport rf power by sustaining a traveling electromagnetic field wave pattern. These hollow pipes are known as *waveguides* and are used to transport microwave power delivered from the klystron amplifier to the accelerator structure. Waveguides are resonant cavities in which electric and magnetic energy are interchanged at a resonant frequency f. At microwave frequencies, waveguides will support two types of resonant modes: the transverse magnetic (*TM*) mode and the transverse electric (*TE*) mode. In the *TM* mode the magnetic field distribution is established in transverse planes that contain the x and y axes and perpendicular to the z axis of the waveguide as in Fig. 3.6. In the *TE* mode the electric field distribution lies in the transverse planes that contain the x and y axes.

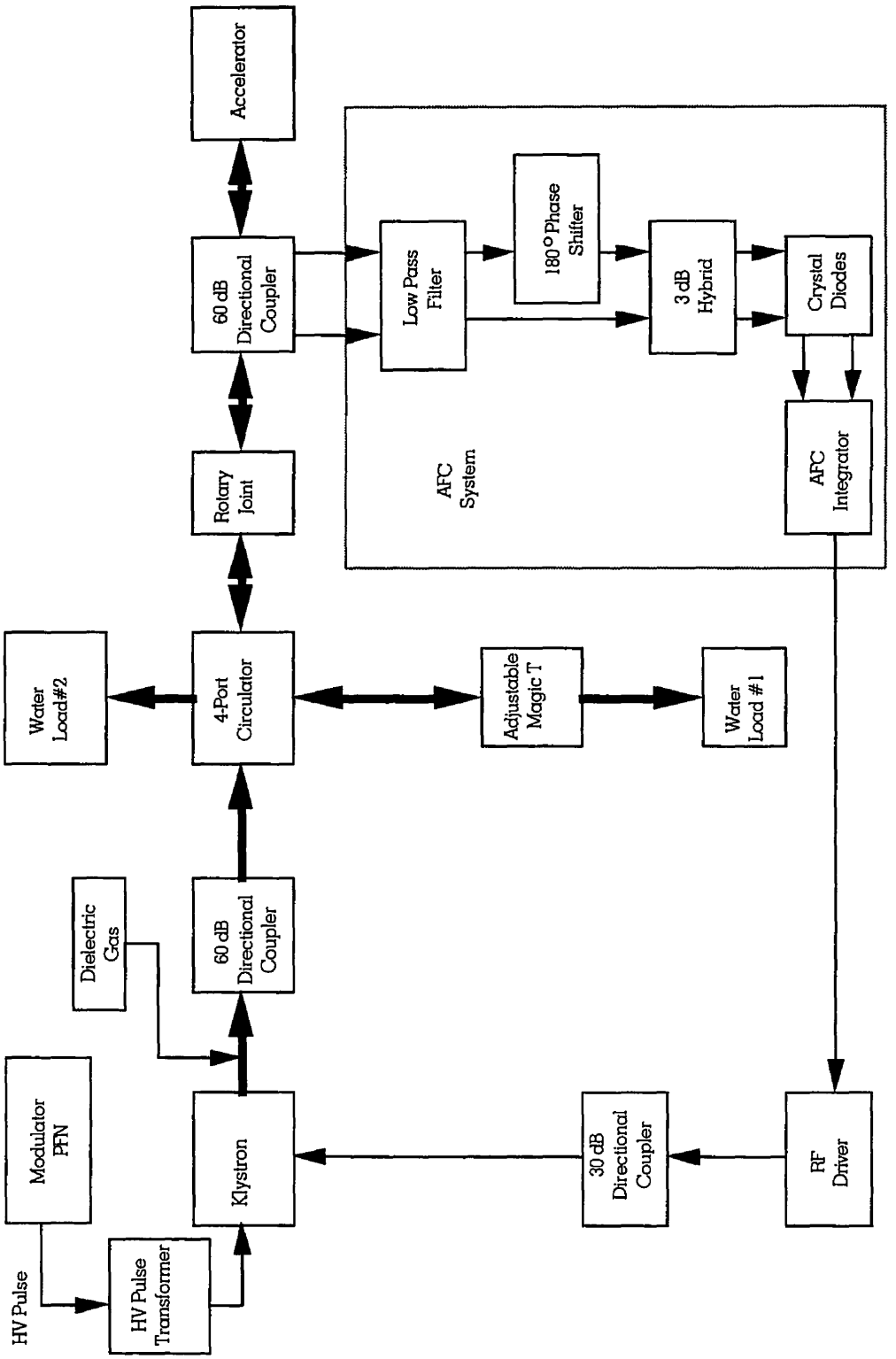

FIGURE 3.5. ***Block diagram showing the Clinac 2300 C/D rf transmission system.***

It is possible to transport many different types of electromagnetic waves within the waveguide, and each wave can be characterized by a different electric and magnetic field configuration. These configurations are specified with the use of subscripts found after the wave resonant mode. For example, in accelerating waveguides the TE_{10} mode is the one most commonly used. The first number after the mode states the number of half-wavelength ($\lambda/2$) undulations in the transverse part of the waveguide. While the second number states the number of $\lambda/2$ undulations in the longitudinal (z axis) part of the waveguide. Also associated with each wave type is a cutoff frequency below which rf transmission is not possible. The wave with the lowest cutoff frequency is referred to as the *dominant mode*.[5] To transport the dominant mode, a rectangular waveguide must have a width of at least one half the free space wavelength of that particular rf wave. The height of the waveguide is not important and is usually made about one half the width.

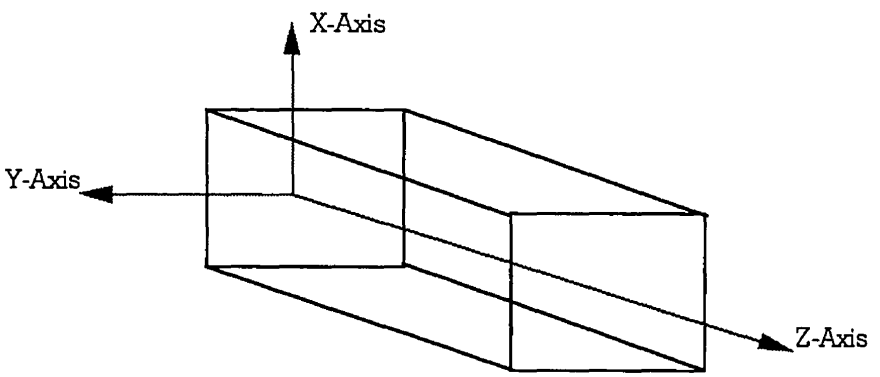

FIGURE 3.6. ***A typical rectangular waveguide with coordinate system used to define the rf mode.***

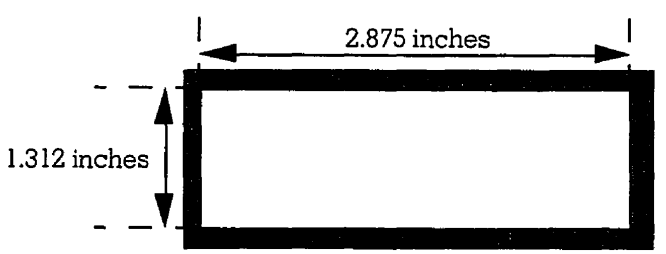

WR-284 Rectangular Waveguide

FIGURE 3.7. ***WR-284 rectangular waveguide used in the Clinac 2300 C/D to transport rf power.***

The Clinac 2300 C/D uses *WR-284* rectangular waveguides (Fig. 3.7) which are used to transport the TE_{10} waves in the *S*-band frequency range (2.6 to 3.95 GHz). The cutoff frequency of the TE_{10} dominant mode occurs at 2.5 GHz. Since the S-band is higher than the cutoff frequency, rf power will always be transported in this waveguide.[1]

3.8.2 Magic-T drive

The magic-T (Fig. 3.8), or shunt-T, is a metal plunger that is inserted into the waveguide and acts as a variable short. The plunger is seated on top of a group of metal studs. The studs each have a different length and are arrayed on a turret that can be rotated to place a chosen stud under the plunger. As the height of the plunger changes, different amounts of rf will be reflected back into the waveguide. Which plunger height is selected will depend upon the chosen beam energy. The position of the magic-T drive will be selected by the mode BCD outputs from the Control processor.

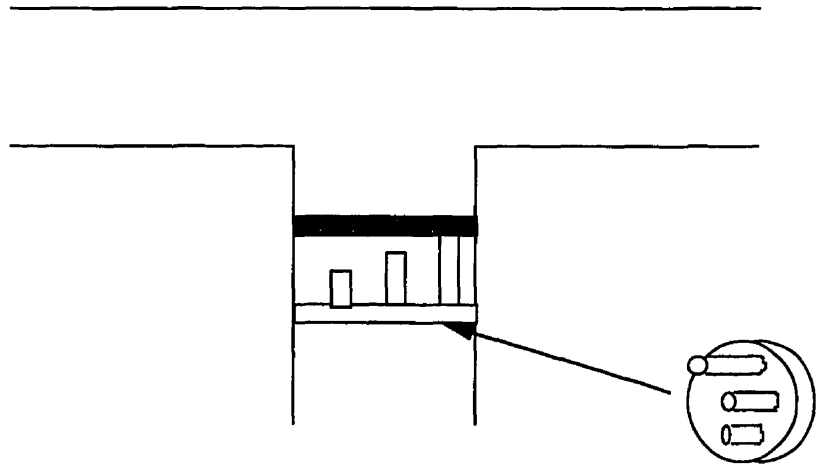

FIGURE 3.8. ***The magic-T drive in the Clinac 2300 that is used to select the amount of rf sent to the accelerator structure depending upon the selected beam energy.***

3.8.3 Directional couplers

A directional coupler is a four-port device that connects one waveguide to another and provides the ability to monitor the forward and reflected rf power within the waveguide. When the input forward rf power travels from port 1 to port 2, a predetermined portion of this signal will appear at port 4. The signal at port 4 is used to monitor the forward rf,

while there is no output at port 3. When a reflected rf signal travels from port 2 to port 1, output will appear at port 3, while none appears at port 4. The output on port 3 will be used to monitor the reflected rf power. The collected forward and reflected rf power signals can be compared to make sure that the waveguide is always operating at the resonant frequency (i.e., that the forward and reflected rf power are in phase with each other).

The directional couplers are characterized by a coupling coefficient which is the ratio of the input power at port 1 to the coupled output power at port 4, expressed in decibels (dB). For example, a 60 dB directional coupler will couple 0.0001% of the input power to port 4 and send the rest to port 2, while a 30 dB directional coupler will couple 0.1% to port 4 and send the rest to port 2.[5]

Another type of directional coupler used is a 3 dB quadrapole hybrid which has the capability of dividing an input signal at port 1 into two isolated quadrature phased output signals at ports 3 and 4. The term quadrature phased means that the two output rf signals are 90^{o} out of phase with eachother.

3.8.4 Circulator

The Clinac 2300 C/D uses a four-port circulator to protect the rf source from the reflected rf power sent back to the source. The circulator is constructed from a ferrite material that rotates electromagnetic fields. A four-port circulator has the property that a wave that enters port 1 will be coupled only into port 2 only; a wave in port 2 will be coupled only into port 3 only; and a wave into port 3 will be coupled into port 4 only.

3.8.5 Automatic frequency control (AFC) system

The AFC system servoes the rf driver frequency by sampling the forward and reflected rf power and comparing their phase relationship. The reflected rf is phase-shifted 180^{o} out of phase with respect to the forward rf at resonance. These signals are then sent to a 3 dB quadrature hybrid. When the forward and reflected signals are 180^{o} out of phase at the hybrid couplers inputs, the outputs have a minimum difference in amplitude. If there is any change in the 180^{o} phase relationship between the input signals, the 3 dB hybrid produces outputs that have noticeable differences in amplitude. The 3 dB hybrid outputs are converted to voltage pulses with the use of crystal diodes. In turn, these voltage pulses are converted to DC voltage and sent to the C-series control electronics where the difference in voltage signal amplitude is integrated and sent back to the rf driver as an AFC error voltage.[1]

3.9 Electron acceleration

The Clinac 2300 C/D consists of a standing wave (*SW*) accelerator structure composed of a series of 21 cavities that resonate at a frequency of 2856 MHz. When electrons are injected into this structure they first encounter a buncher half-cavity. This first cavity accelerates the electrons from their injected velocity to almost the speed of light. In addition, the electrons are formed into compact bunches. As the electron bunches pass through the rest of the accelerator structure cavities in synchronism with the *SW* accelerating field, they gain the required amount of kinetic energy to produce x rays.

3.9.1 Electron accelerator structure

The electromagnetic field distributions in a circular cylindrical cavity (i.e., pill-box cavity) can be found by solving Maxwell's equations with the appropriate boundary conditions taken into consideration. In a pill-box cavity cylindrical coordinates (ϕ,r,z) are used so that the solutions to Maxwell's equations may be written in terms of Bessel functions. The resonant frequency of a cylindrical cavity is a function of geometry and the resonant mode.

In cylindrical waveguides a *TM* wave with m half-Bessel variations in the ϕ direction and n half-Bessel variations in the r direction is referred to as a TM_{mn} wave. The TM_{01} is a very important resonant mode. It possesses the unique property that the electric field is parallel to the waveguide axis and has a maximum intensity at the axis (see Fig. 3.9). Therefore, TM_{01} is the most suitable mode for the acceleration of electrons.

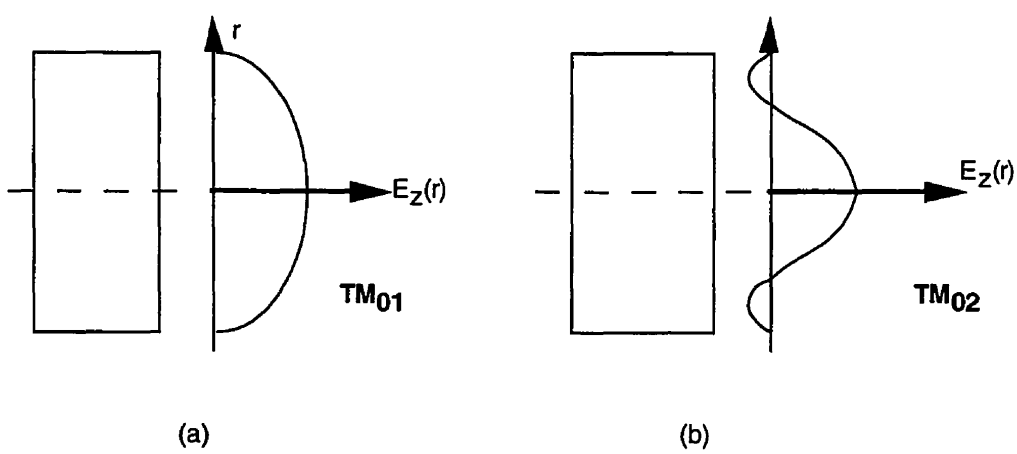

FIGURE 3.9. ***Radial variation of the axial electric field $E_z(r)$ for (a) the TM_{01} resonant mode and (b) the TM_{02} resonant mode.***

There is one practical problem when dealing with the TM_{01} mode. The electric field that accelerates the electrons has a velocity (i.e., phase velocity) that exceeds the speed of light. This makes a uniform waveguide unsuitable for continuous acceleration of electrons. This problem is rectified by inserting a series of annular disks into the accelerator waveguide to modify the electric field pattern, as shown in Fig. 3.10. These disks slow down the electric field phase velocity so that the wave stays in step with the accelerated electrons. In addition, the disks divide the pill-box cavity into a series of discrete cylindrical cavities that are coupled through their apertures. Since the aperture is located near the axis, the accelerating electric field intensity is maximum (TM_{01}). Such accelerating waveguides are known as *slow wave structures* or *loaded waveguides.*[5,6]

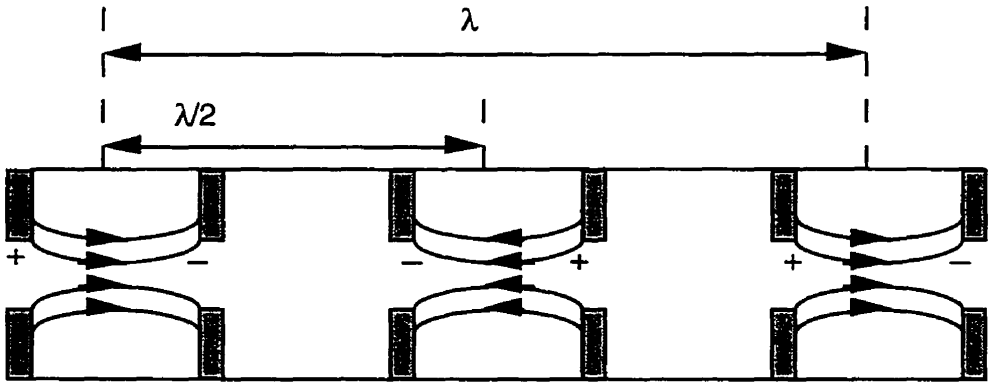

FIGURE 3.10. ***Electric field pattern and charge distribution at an instant in time along the axis of a disk loaded cylindrical waveguide.***

As electrons are injected into the accelerator guide, their velocity is less than the speed of light. To ensure that phase stability exists between the electrons and the accelerating field, the initial portion of the accelerating structure consists of a half-cavity. This section of the accelerator structure is called the buncher section since the continuum of injected electrons from the gun is concentrated into discrete bundles as well as accelerated along the waveguide axis. After the buncher section is traversed, the electron velocity is approximately equal to the speed of light. The subsequent accelerator cavities will therefore be uniform for further acceleration of the electrons.

A standing wave (*SW*) accelerating structure is created by the interaction of a forward moving and a backward moving electric field distribution, each of which is reflected at the ends of the accelerator structure to produce standing wave patterns that oscillate with time. The two moving electric field maxima and resulting net electric field distribution is shown in Fig. 3.11. It can be noticed that the net electric field distribution is a result of constructive interference of the forward and backward wave components. An important feature in standing wave structures is that every other accelerator cavity has a zero net electric field intensity at all times because at times the forward and backward components are each zero, and at other times the components have equal amplitude but opposite in direction (i.e., destructive interference).

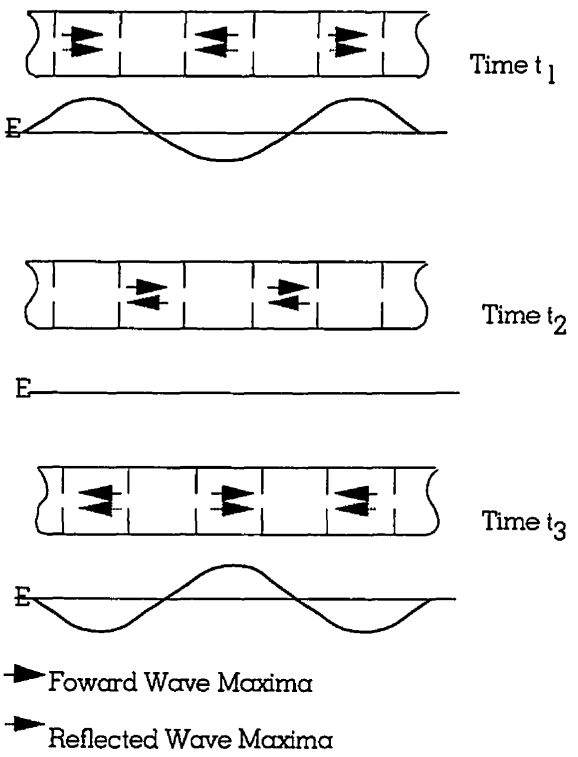

FIGURE 3.11. ***Standing wave electric E field patterns in a disk loaded accelerator structure for combined forward and reflected waves at three instants of time. At time t_2, the E field is zero in all cavities.***

The zero-field cavities described above couple the microwave power between adjacent accelerator cavities but do not participate in the acceleration process. For this reason, the

zero-field cavities may be placed off the acceleration axis to form a side coupled *SW* accelerator structure.[7] This offers the advantage of shortening the overall length of the accelerator structure. Figure 3.12 illustrates the side coupled *SW* structure.

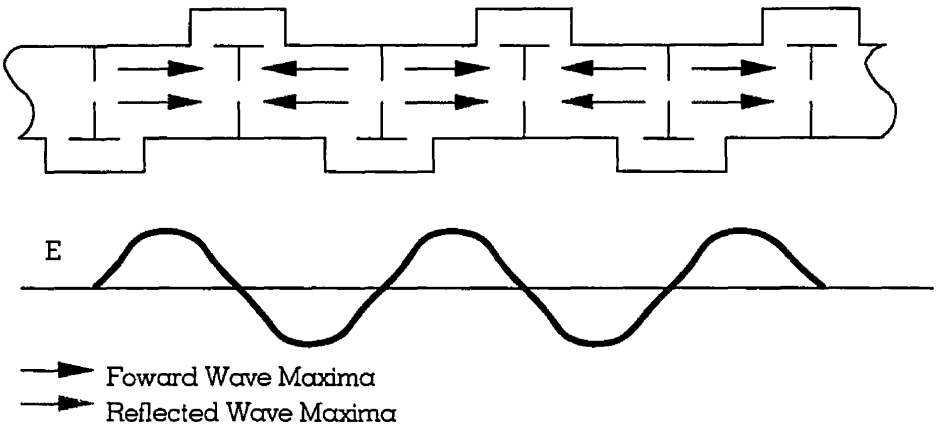

FIGURE 3.12. ***A typical side-coupled acclerator structure and related electric E field pattern along the waveguide axis.***

3.9.2 Energy switch

The Clinac 2300 C/D uses the same electron yield for both 18 MV and 6 MV photon production. However, to produce the 6 MV beam an energy switch (i.e., copper plug) is inserted into one of the coupling cavities and prevents the generation of *SW* rf acceleration fields from the switch to the end of the accelerator. This process prevents the electrons from accelerating any further when they reach this fieldless region, thus lowering the energy of the beam. This energy switch is controlled by mode BCD signals sent by the Control processor.

3.10 Beam transport magnet system

When electrons are injected into the accelerator structure they experience electrostatic repulsion due to their like charges. For this reason steering coils are employed to guide these electrons on the accelerator axis and prevent them from diverging into the walls of the accelerator. In addition, when the electron beam emerges from the accelerator exit window, it must be redirected to strike an x-ray target perpendicularly at a specific loca-

tion in order to achieve a symmetrical dose distribution. This is accomplished with the use of focusing quadrupoles and bending magnets. So, in general, the beam transport magnet system (Fig. 3.13) confines, guides, steers, and focuses the electron beam from the injection to the x-ray target.

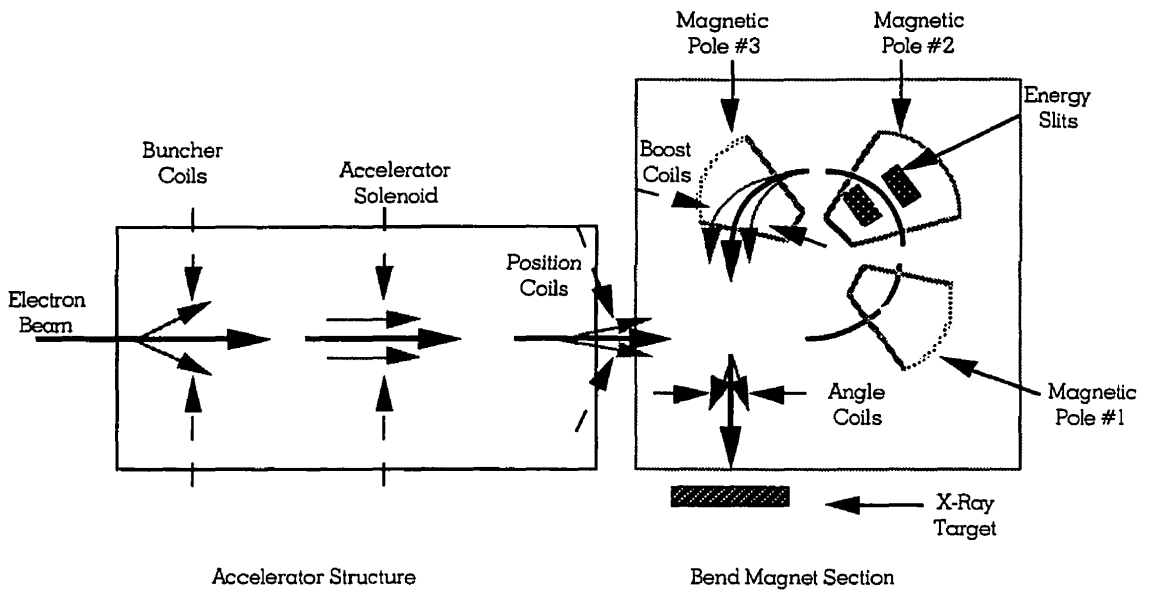

FIGURE 3.13. ***Schematic diagram of the Clinac 2300 C/D beam steering system.***

3.10.1 Steering coils

In the Clinac 2300 C/D there are four sets of steering coils. They are the buncher coils, position coils, angle steering coils, and the boost coils. Steering coils induce magnetic fields that counteract the Coulombic repulsion between electrons as they enter or exit the accelerator structure. With the exception of the boost coils, each of these sets has a pair of coils for the radial plane and another pair for the transverse plane. The amount of current that flows through these coils, and the resulting magnetic field magnitude, are determined by the energy program board. This provides the appropriate amount of electron steering needed for 18 MV and 6 MV photon beam production.

3.10.2 Three sector 270° bending magnet

Figure 3.13 shows a cross sectional view in the central orbit bending plane of the achromatic 270° bending magnet system used in the Clinac 2300 C/D. *Achromatic* is a term used to describe transport systems that bring paraxial electrons of different energies to the same focal point.[5] This particular design uses three uniform field pole sets separated by zero field drift space. The trajectories of all the electrons in this system are symmetric about a line of symmetry located at an angle of 135° with respect to the entrance beam. Since the electron beam enters the bending magnet system with a range of energy, the beam must be restricted in energy. For this reason energy selection slits are implemented in between the second pole face which remove electrons that differ from the nominal energy by more than ±3%.[1]

The coils used to produce the bending magnets are made of thin hollow copper tubing.[8] Since an extremely large current is passed through the coils, temperature increase can be a problem. To solve this problem, water flows through the interior of the hollow tubing to provide cooling. The large bending magnet currents are produced by a 5 kW power source found in the drive stand. The amount of current to be sent to the bending magnet coils is determined by the BCD mode outputs from the C-Series Control processor. The C-Series control electronics checks to verify that the correct magnetic field strength intensity is used for the chosen energy. If the field strength is incorrect, an interlock is activated.

3.11 X-ray production

To produce x rays the electron beam is directed at a copper target after leaving the beam magnet transport system. When electrons impinge upon this target, they slow down and radiate energy in the form of x rays according to the Larmor equation:

$$P = \frac{e^2}{6\pi\varepsilon_o m^2 c^3}\left|\frac{dp}{dt}\right|^2 \tag{3.1}$$

where P is the radiated power, e is the charge of the electron (1.602×10^{-19} C), ε_0 is the permittivity of free space (8.854×10^{-12} F/m), m is the mass of an electron (9.109×10^{-31} kg), c is the speed of light in vacuum (2.998×10^{8} m/s), and dp/dt is the rate of change of the electron momentum.

The x rays that are produced by the deceleration of electrons are known as *bremsstrahlung* (braking radiation). The bremsstrahlung has a continuous energy spectrum with a maximum energy equal to that of the incident electron kinetic energy. The bremsstrahlung produced by high energy electrons is peaked in the forward direction, the higher the electron energy, the more forward peaked the photon distribution becomes.

The copper target used in the Clinac 2300 C/D has two thicknesses. The thin part of the target is used for the 6 MV photon mode and the thick part of the target is used for the 18 MV photon mode. The drive mechanism that positions the x-ray target in front of the electron beam to yield x rays is controlled by the mode BCD outputs of the C-Series control processor. The target drive is actuated by the electronics and microprocessor found in the carrousel.

3.11.1 Beam shaping systems

The purpose of the beam shaping system, shown schematically in Fig. 3.14, is to define the x-ray field size that will be used to treat the patient. The beam shaping system also ensures that the field is homogenous throughout the specified field size. The steps in which the x-ray beam is shaped are described as follows:

1. The x-ray beam emitted from the target is directed through a series of primary collimators (made of tungsten) that define the maximum angular spread of the x-ray beam. The opening through these collimators is in the shape of a truncated cone, with an angle of 30^{o}.

2. After leaving the primary collimators, the photon beam will impinge upon a flattening filter. The flattening filter is thicker at the center than it is at the edges. This attenuates the x rays along the beam central axis more than those near the edge resulting in dose profiles that are uniform to within ±3% of the central axis dose over 80% of the longitudinal and transverse axis of a 10×10 cm^2 field at a depth of 10 cm and an *SSD* of 100 cm.

3. The beam then passes through two independent ionization chambers to monitor the output and symmetry of the radiation beam. The two ionization chambers are sandwiched together with their collector plates at 90^{o} from each other, allowing for the detection of beam intensity and beam displacement.

4. After passing through the ionization chamber, the x-ray beam passes through a secondary collimator whose function is the same as that of the primary collimator.

5. The x-ray beam then passes through two pairs of adjustable collimators placed one above the other and at right angles to each other. They may be opened or closed to define the treatment field size needed. In essence, they give the x-ray field its final shape, which can vary from any square or rectangle with sides from 0.5 cm to 40 cm.

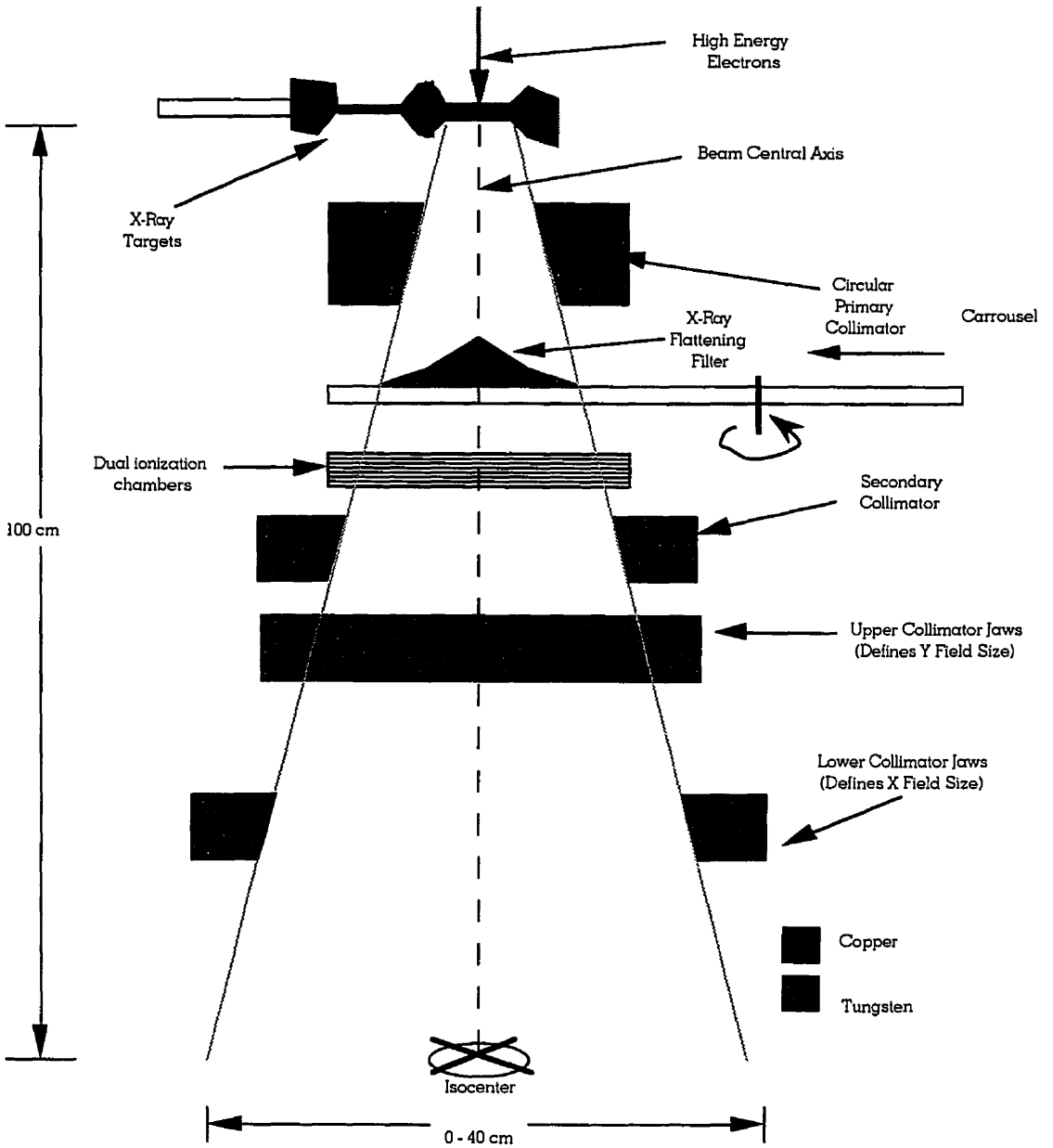

FIGURE 3.14. ***Schematic diagram of the Clinac 2300 C/D beam shaping system.***

3.12 References

1. Clinac 2300 C/D maintenance manual, Varian Associates, Palo Alto, California (1992).

2. T. S. Curry, J. E. Dowdey, R. C. Murry: Christensen's Physics of Diagnostic Radiology, 4th edition. Lea & Febiger, Philadelphia, U.S.A. (1990).

3. Private communication with Joe Larkin, Medical Physics Department, Montreal General Hospital, Montreal, Canada.

4. R.H. Varian, S.F. Varian: *A high frequency oscillator and amplifier*, J. Appl. Phys. **10**, 321-327 (1939).

5. C. J. Karzmark, C.S. Nunan, E. Tanabe: Medical Electron Accelerators, McGraw-Hill, Inc. (1983).

6. H.E. Johns, J.R. Cunningham: The Physics of Radiology, 4th edition, Charles C. Thomas, Springfield, Illinois (1983).

7. E. A. Knapp, B. C. Knapp, J. M. Potter: *Standing wave high energy linear accelerator structures*, Rev. Sci. Instr. **39**, 979-991 (1968).

8. Private communication with Paul Lefebvre, Medical Physics Department, Montreal General Hospital, Montreal, Canada.

DOSIMETRY OF WEDGE FILTERS AND DYNAMIC WEDGES

4.1 Introduction

In many clinical situations related to radiotherapy it may be necessary to use wedged-shaped isodose distributions to compensate for missing tissue, irregular surface contours, beam intersections, or irregular tumor volumes.[1] These so called "wedged fields" can be obtained using a variety of methods. In the early years of radiotherapy wedged fields were produced by using "in-house" physical wedges[2] or by shrinking the field size during the course of therapy through moving a lead block across the field. Today, linear accelerators are delivered with physical wedges as standard accessories. With the advent of computer-controlled linear accelerators, such as the Varian Clinac 2300 C/D installed in our department, it has become possible to generate these wedged fields dynamically making the physical wedges obsolete.

The optimal use of wedge beams in radiotherapy procedures requires a precise knowledge of the dosimetric properties of the wedge technique being used. These dosimetric properties are defined and explained in this chapter, first for conventional standard physical wedge filters and then for the dynamic wedges. Parameters of wedged fields produced by physical and dynamic wedges are compared at the end of the chapter.

4.2 Conventional wedge filters

The conventional wedge filter has been the most common beam modifying device used in radiation therapy treatments for the past 40 years. It is frequently employed in treatments of breast as well as head and neck cancers. A wedge filter is usually constructed from a high density material, such as lead, steel, or brass, designed in such a way that it causes a progressive decrease in the photon intensity across the photon field, resulting in a tilt of the isodose lines from their original open field configuration. The degree of tilt depends upon the design slope and the material of the wedge filter itself. The sloping filter surface

is either straight or sigmoid in shape, and the latter is used to generate optimized isodose lines. The individual wedge filters are affixed to a suitable accessory tray and are usually stored on shelves in the treatment room where they are easily accessed when needed. When a treatment plan requires the use of a wedge filter, the appropriate filter is taken from its shelf and inserted into an accessory tray holder located on the head of the treatment unit. When mounted, the distance from the wedge tray and the patient surface is usually at least 15 cm or more to preserve the skin sparing effect.

The wedge filter design used in standard linear accelerators is referred to as a "universal wedge" system.[3] In such a system several wedges, each with a different degree of slope, are available for a maximum beam width and length. These type of wedge filters are fixed in the center of the photon beam and the field size can be varied, as illustrated in Fig. 4.1. In such a wedge system, for a given field width W not all of the wedge filter material is useful in producing the desired wedge angle. Only the shaded region ABC is effective in tilting the isodose lines, while the remainder of the wedge material (ACDE) only decreases the photon beam intensity for field widths smaller than the maximum field width W_{max}.

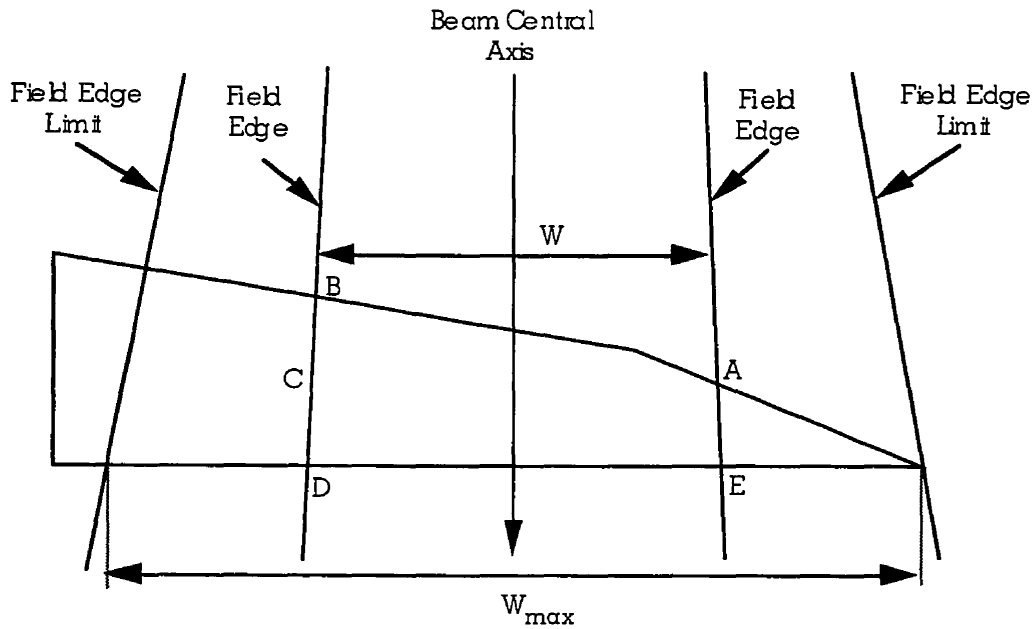

FIGURE 4.1. ***Universal wedge system used with linear accelerators in which the central axis of a sigmoid shaped wedge filter is fixed at the beam axis and the field size can be varied.***

4.2.1 *Wedge angle*

The decrease in intensity across the photon beam resulting from the presence of the wedge filter in the beam causes a tilt in the isodose distribution. For each wedge field the isodose curves are normalized to 100% at the depth of maximum dose d_{max} on the central axis for the energy and field size being measured. As shown in Fig. 4.2, the isodose lines will be tilted away from the thin end of the wedge. This results in isodose lines that penetrate deeper into tissue under this end. Conversely, the point on the isodose lines under the thick end of the wedge will be less penetrating than the central axis points. The degree of the tilt depends on the physical construction of the wedge filter itself. This isodose tilt is described quantitatively by the *wedge angle* which is generally defined as the angle between the 80% isodose curve and the normal to the beam central axis at the 80% isodose curve intercept with the central axis, as depicted by ϕ in Fig. 4.2.[2] Sometimes other isodose values, such as for example 50%, are used for the wedge angle definition.

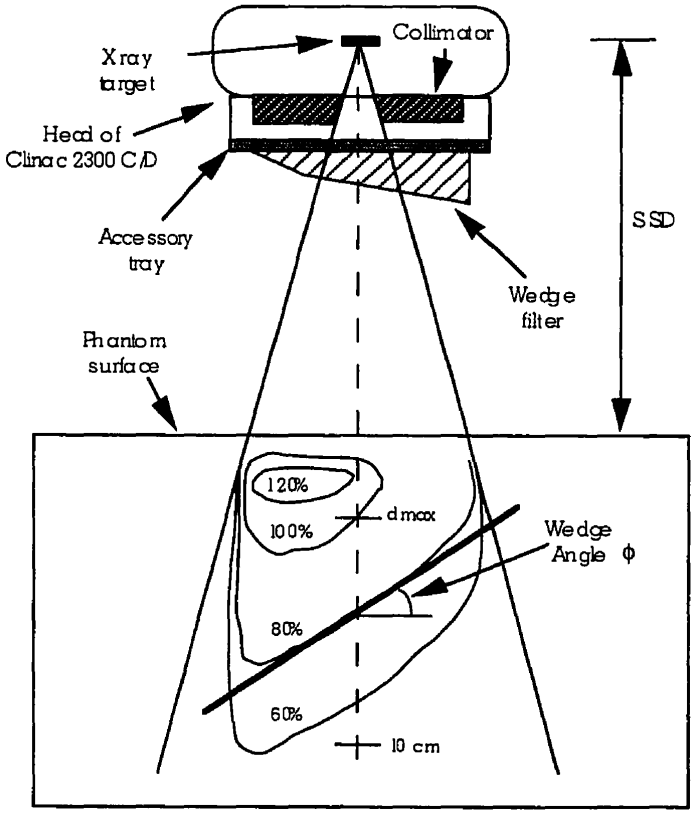

FIGURE 4.2. ***Definition of wedge angle for conventional physical wedges.***

The Clinac 2300 C/D linear accelerator is equipped with four sigmoidal, stainless steel physical wedges as standard accessories. The wedge set consists of wedges with nominal wedge angles of 15°, 30°, 45°, and 60°. The 15°, 30°, and 45° wedge filters are optimized to accommodate maximum field sizes of (width × length) 20 × 20 cm^2, whereas the 60° wedge filter can accommodate a maximum field size of 15 × 20 cm^2.

4.2.2 Wedge factor

The presence of the wedge filter in the path of the photon beam results in various attenuation processes which reduce the intensity of the photon spectrum and subsequently decrease the beam output as measured on the central axis at depth of d_{max} with respect to the open beam. This attenuation must be taken into account in treatment dose calculations. The term *wedge factor* is used to quantify this reduction in intensity on the beam central axis. For a given field size the wedge factor is defined as the ratio of the beam outputs in phantom with and without the wedge filter present at the depth of maximum dose on the central beam axis.[4,5,6] This can be seen mathematically in the following equation:

$$WF = \frac{D_{dmax}^{wedge}}{D_{dmax}^{open}} \quad , \tag{4.1}$$

where D_{dmax}^{wedge} is the output at depth d_{max} on the beam central axis with the wedge filter in place and D_{dmax}^{open} is the output at depth d_{max} on the beam central axis with no wedge filter. Therefore, the wedge factor equals the factor by which the calculated number of monitor units must be divided in order to deliver the same dose on the beam central axis at d_{max} with a wedged beam as with an unfiltered open beam. Since the wedge filter attenuates the primary photon beam and contributes a significant amount of scattered photons to the treatment beam, the wedge factor is a function of both the field size and the depth of measurement in the phantom.[7,8]

4.2.3 Central axis percentage depth dose

When a wedge filter is placed in the photon beam, a number of photons will interact with the filter and be removed from the beam. A measure of how many of these incident photons will interact per unit thickness of attenuator material is described by the *linear attenuation coefficient* μ. It should be noted that μ depends in a complex way on the composition of the attenuator itself and on the energy of the incident radiation. A more fundamental absorption coefficient is the *mass attenuation coefficient* which is calculated

by dividing the linear coefficient by the physical density ρ of the attenuator material. This coefficient, represented by μ/ρ, is independent of the attenuator density.

The Varian wedge filters are made of nickel plated AISI #1020 steel and have a composition of 0.10% to 0.23% carbon (C), 0.30% to 0.60% manganese (Mn), 0.04% phosphorous (P), 0.05% sulphur (S). The balance of the mixture is iron (Fe).[9] The averaged mass attenuation coefficient as a function of energy for this particular wedge composition is shown in Fig. 4.3. It is apparent that lower energy photons have a much higher probability of interacting with the wedge filter relative to higher energy photons. The effect that the wedge filter has on the incident photon beam is illustrated schematically with respect to a typical photon spectral distribution in Fig. 4.4. As the beam traverses the wedge filter, lower energy photons are preferentially attenuated by the beam resulting in an overall reduction in beam intensity and an increase in the effective energy of the beam. This implies that the beam becomes harder and more penetrating after passing through a wedge. At high photon energies the beam can also be softened to a lesser extent by pair-production interactions depending on the photon beam energy and the material the wedge is constructed from.[7] It should be noted that the difference in areas under the spectral distribution before and after traversing the wedge filter is representative of the wedge factor.

For lower energy photon beams (e.g., 6 MV) the wedge filter generally causes an overall increase in the percentage depth dose at all depths as seen in Fig. 4.5. The noticeable increase in the *PDD* values at all depths in phantom can be attributed to two factors: (1) beam hardening effects and (2) differences in scatter produced from the thin and thick sides of the wedge filter.[10,11] If the amount of scatter produced on one side of the wedge filter increases more than it is reduced on the other side, as is the case with sigmoidal shaped wedges, a larger portion of scatter will be measured on the beam central axis. This increase in scatter generated from the wedge filter, combined with an increasing amount of phantom scatter with depth, yields a higher percentage depth dose compared with the open field photon beam. Wedge filters with a straight profile will most likely not manifest this increase in scatter, therefore only beam hardening is involved in such radiation beams. The variation in percentage depth dose has the tendency to increase with increasing wedge angle[2], since higher angle wedge filters have more physical material that the photons must traverse. Therefore, photons traversing large angle wedge filters will experience more attenuation and scatter as compared to lower angle wedge filters.

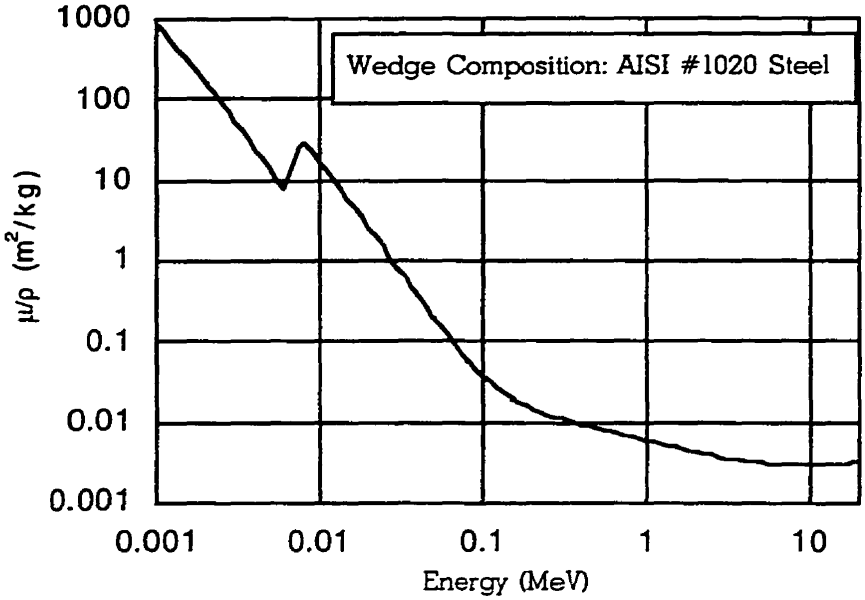

FIGURE 4.3. ***Average mass energy absorption coefficient as a function of energy for the Varian AISI #1020 steel physical wedge filters.***

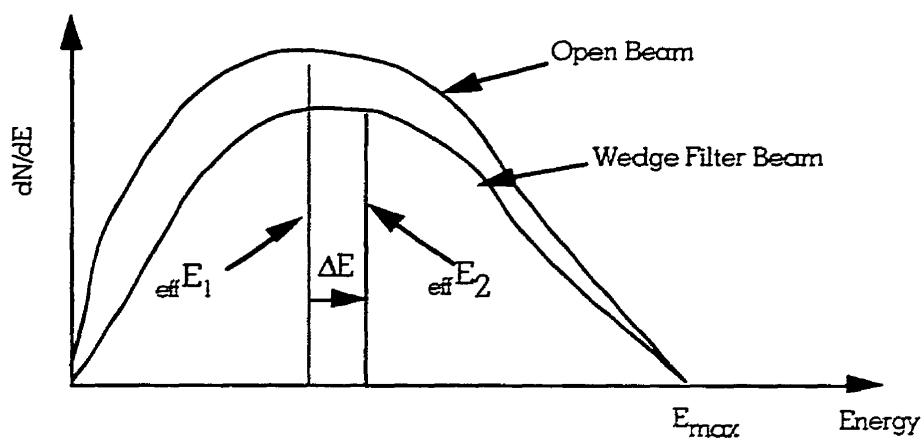

FIGURE 4.4. ***A typical photon spectral distribution and the attenuation effects seen as the photon beam penetrates a wedge filter. As a result of preferential attenuation of low energy photons, there will be an increase (ΔE) in the effective energy ($_{eff}E$) of the photon beam.***

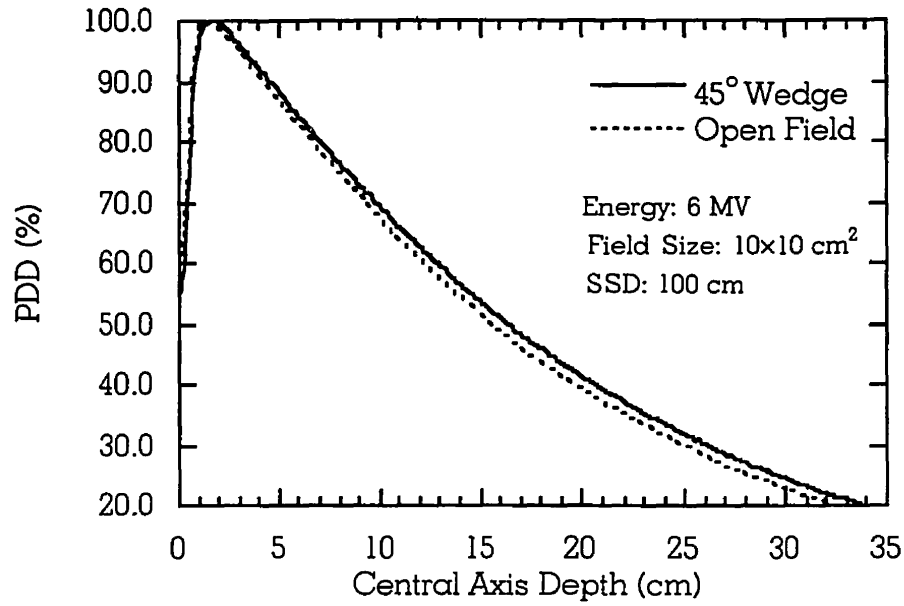

FIGURE 4.5. ***Demonstration of the beam hardening effects caused by a 45° physical wedge filter on a 6 MV photon beam. Field size: 10×10 cm², SSD: 100 cm.***

4.2.4 Wedge profile

The term *dose profile* or off-axis ratio is used to describe the dose at a point off the central axis of the beam relative to the dose on the central axis at the same depth. When wedge filters are used, they drastically decrease the machine output and alter the open beam profile of the photon beam. Figure 4.6 illustrates the difference in beam profiles from the Clinac 2300 C/D in the 6 MV mode for open and wedged fields. Photons that pass through the thick end of the wedge (i.e., cold side) have to travel a greater distance through the wedge material to reach the same depth in phantom as photons on the wedge central axis. The result is that more lower energy photons will be filtered out of the beam by the wedge, which then causes a decrease in absorbed dose, relative to the central axis, under the thick end of the wedge. In contrast, the thin end (i.e., hot side) attenuates fewer lower energy photons with respect to the thick side since there is not as much material present. Therefore, the absorbed dose under the thin end of the wedge increases relative to the dose measured on the central axis of the wedge. To compensate for the decrease in machine output,

the wedge factor is incorporated into the treatment protocol so as to deliver the same relative dose to the beam central axis as shown in Fig. 4.6.

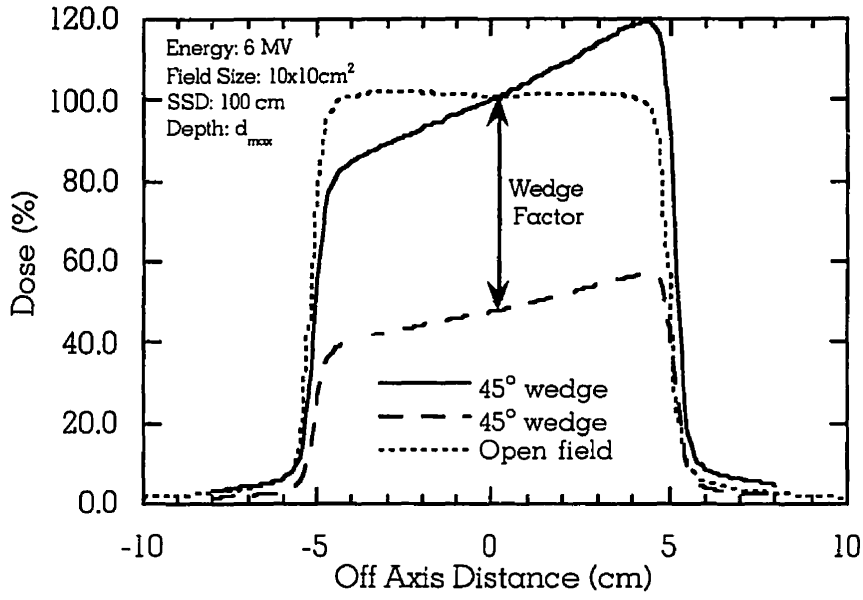

FIGURE 4.6. ***Comparison of open and 45° beam profiles for a 10x10 cm² 6 MV photon beam.***

In the non-wedged direction (i.e., perpendicularly to the wedge gradient) wedge filters add a homogeneous thickness of material to the flattening filter. Due to beam divergence (beam obliquity) this excess metal over-attenuates the photons at the edge of the beam since these photons travel greater distances through the wedge material than the photons at the center of the field, as shown in Fig. 4.7 with $d' > d$. This effect is exacerbated by the fact that photon energy is lower at distances away from the central axis as a result of the production of bremsstrahlung in the target and attenuation of the radiation beam by the flattening filter. These effects combine to influence the overall beam flatness, and as a result the radial symmetry of the open beam is degraded.

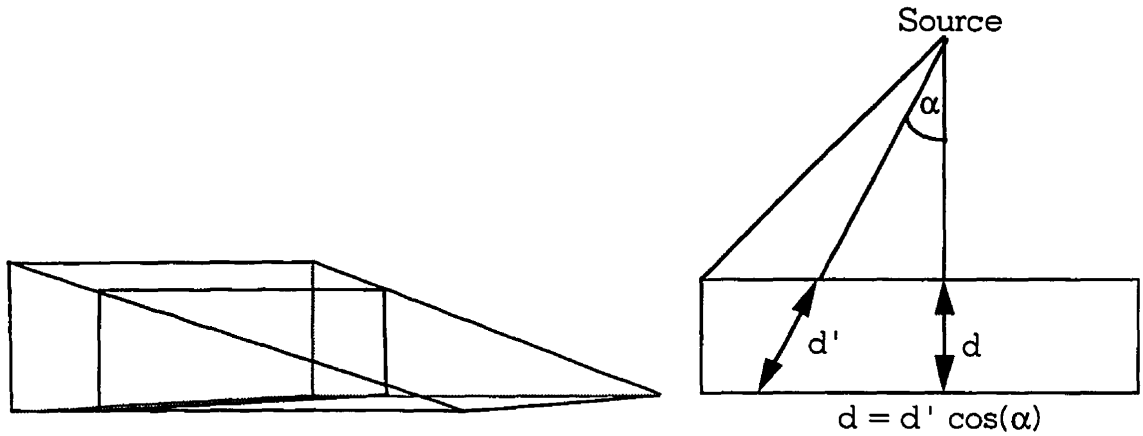

FIGURE 4.7. ***In the non-wedged direction photons at the edge of the field will be over-attenuated since they must travel a greater distance through the wedge material (d') than photons at the center of the field (d).***

4.3 Dynamic wedge

Conventional physical wedges have several practical and dosimetric problems. They are limited in size, are relatively heavy, and must be manually lifted overhead when placed onto the machine. They also block the optical distance indicator and can sometimes be misalinged or move slightly during the course of treatment. This can alter wedge factors especially for higher angle wedges, since they have more material and steeper slopes than lower angle wedges. If placed slightly off center in the accessory tray, the photon beam traverses more (or less) material than it would if aligned properly, resulting in a noticeable change in the wedge factor. Dynamic wedges obviate these problems.

The current use of computer-controlled collimator motion to create wedged shaped fields in modern linacs is by no means a new idea. It was investigated as early as 1978 by Kijewski et al.[12] However, it was not until the early 1990s, when the computer was commercially linked with the linear accelerator control unit, that the practical use of the "dynamic wedge" became feasible for clinical applications.

4.3.1 Basic operation

Our Clinac 2300 C/D linac has the capability of moving independently any of the four collimator jaws (two lower X-jaws and two upper Y-jaws) found in the treatment head. These

movements can be activated not only during the patient setup on the treatment machine in preparation for treatment, but also during the actual treatment delivery. In the dynamic wedge mode, one of the upper collimator jaws (Y1 or Y2) moves in a continuous fashion to create a continuously decreasing field width while the radiation beam is on. Because of this Y-collimator motion, different segments of the treatment field are exposed to the primary beam for different periods of time. Additionally, as the field size decreases the Y-collimator velocity and dose rate are modulated. The amount of dose that is delivered as the Y-collimator closes is uniquely specified by a segmented treatment table (STT). A unique STT table exists for each nominal dynamic wedge angle (15°, 30°, 45°, and 60°) and field width (4.0 cm to 20.0 cm in 0.5 cm increments), which results in 256 tables in total for each of the 6 MV and 18 MV photon beam energies. This process of shrinking the field width while modulating the Y-collimator velocity and dose rate creates the desired wedge shaped isodose gradient across the treatment field in the patient.

4.3.2 Dose delivery procedure

In order to generate the dynamic wedge distributions in the patient the dose delivered to specific reference points within the treatment field must be known precisely. These reference points, which define the dynamic wedge beam weights, must be accurately calculated. This requires knowledge of changes in open beam intensity, collimator scatter, phantom scatter, and primary transmission through the independent Y-collimator jaw.

When the prescribed number of MUs, wedge angle, and energy are entered into the C-series computer through the Varian dedicated keyboard, beam weight reference points are automatically distributed along a line that will generate the idealized wedge isodose angle. The total number of these reference points is equal to the number of collimator jaw positions found in the STT used to generate the specified, dynamically wedged field.[13] These reference points are distributed in such a way that the first reference point, corresponding to the thick end of the wedge, receives only the open field dose. All other successive reference points will receive additional dose from a continuously shrinking field width. The last reference point, corresponding to the thin end of the wedge, will be exposed for the entire treatment time.

At the beginning of the dynamic wedge treatment the collimators are opened to the full open field width and MUs are delivered until a desired baseline dose is given to all reference points. When this desired dose is achieved either the Y1 or Y2 collimator begins to close, depending upon the orientation chosen. The dose rate and the jaw velocity are mod-

ulated in such a way that the desired cumulative dose is given to the first reference point. When the collimator reaches the next predefined STT collimator position, MUs and Y-collimator velocity are once again modulated so as to deliver the differential between the full desired dose to the second reference point and the dose already received by this point thus far. This process is repeated for all the generated reference points, ending with the last reference point. These optimal field weights are used to dynamically create the desired wedge shape isodose distributions. It should be noted that the Varian dynamic wedge uses reference points spaced in 0.25 cm increments for dynamic field widths ranging from 4.0 cm to 9.5 cm. For dynamic field widths from 10 cm to 20 cm, the reference points are spaced in 0.5 cm increments.

4.3.3 Calculation of dose to reference points

The method in which the dose rate and Y-collimator velocity are modulated to deliver the desired dose to the beam weight reference points strongly depends upon the dynamic wedge field width at a given moment in time. As the treatment field becomes smaller during the dynamic wedge operation, there is a resulting change in collimator scatter and phantom scatter which must be accounted for.

For static symmetrical open fields, the *collimator factor* and the *scatter factor* are defined to account for subsequent changes in collimator and phantom scatter, respectively, as a function of field size. As the field size is increased, the output of the machine also increases due to a rise in collimator scatter which is added to the primary beam. When the collimators are opened to produce a larger field size, more collimator surface area is exposed to the photon beam causing a measurable increase in scatter. The collimator scatter is represented by the collimator factor which is defined as the ratio of output in air for a given field to the output in air for a 10×10 cm^2 field at the nominal machine *SAD*. Mathematically speaking:

$$CF(FS_{SAD}) = \frac{D'_P(FS_{SAD})}{D'_P(10 \times 10_{SAD})} \quad , \tag{4.2}$$

where CF is the collimator factor for the given square field FS_{SAD}, $D'_P(FS_{SAD})$ is the dose to a small mass of tissue in air for the given square field FS at SAD, and $D'_P(10 \times 10_{SAD})$ is the dose in air for a 10×10 cm^2 field at SAD.

The scatter factor can be measured indirectly through the measurement of the *relative dose factor* (*RDF*) and the collimator factor. The relative dose factor is a quantity which reflects the dose at a point in phantom due to *both* the collimator scatter and the phantom scatter. As the field size is increased, more scatter is produced from the collimators as explained above. In addition, more phantom scatter is produced since the geometrical scatter volume in the phantom increases as the field size becomes larger. The relative dose factor is defined as the ratio of the output at d_{max} for a given field size at *SSD* to the output at the same depth for a 10×10 cm^2 field at *SSD*. The relative dose factor is thus defined as follows:

$$RDF(FS_{SSD}) = \frac{D_p(FS_{SSD})}{D_p(10 \times 10_{SSD})} \quad , \tag{4.3}$$

where $RDF(FS_{SSD})$ is the relative dose factor for an arbitrary field size at *SSD*, $D_p(FS_{SSD})$ is the dose at d_{max} in phantom for the field size *FS* at *SSD*, and $D_p(10 \times 10_{SSD})$ is the dose at d_{max} for a 10×10 cm^2 field at *SSD*.

Once the *CF* and the *RDF* are measured, one can calculate the phantom scatter factor (*SF*). Since the *RDF* describes both the collimator scatter and the phantom scatter, while the *CF* contains only the collimator scatter, the phantom scatter contribution can be found simply by dividing the *RDF* by the *CF*, both for the same field size *FS*, as seen in the following formula:

$$SF(FS_{SSD}) = \frac{RDF(FS_{SSD})}{CF(FS_{SAD})} \quad , \tag{4.4}$$

For symmetrical open fields the output factor data need only be specified at one point on the central axis of the photon beam. However, for dynamically wedged fields the output factors need to be redefined at suitable reference points since the field size is constantly decreasing and the field at a given moment in time is asymmetric. As the field width decreases in the dynamic wedge mode, the dose rate and Y-collimator velocity must be modulated to compensate for a reduction in collimator scatter and phantom scatter. These reference points are selected to be points on the central ray lines of predetermined asymmetric dynamic field widths. The output in air, $D'_P(FS_{SAD})$, at point *P* on the central ray of such an asymmetric dynamic field and a lateral distance *x* away from the original open field central axis (Fig. 5.8) is defined as[14]:

$$D'_P(FS_{SAD}) = D'_O \cdot CF(r,0) \cdot OAR(x) \quad , \tag{4.5}$$

where D'_O is the output in air for an open symmetric static 10×10 cm^2 field, *CF(r,0)* is the collimator factor in air on the central axis of a static open field that has the same size as the asymmetric dynamic field, and *OAR(x)* is the off-axis ratio measured in air at the lateral distance x from the central axis. Equation (4.5) implies that the collimator factor for such asymmetric dynamic fields can be calculated using only static symmetrical open field output factor data and one open beam profile for the largest field size available.

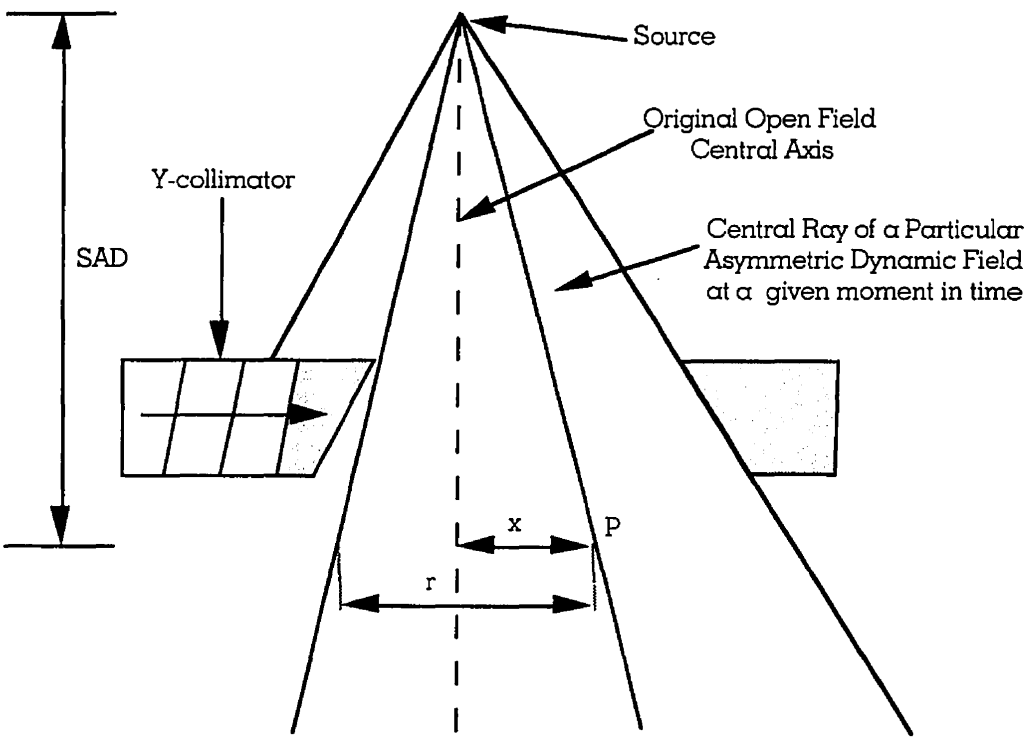

FIGURE 4.8. ***Geometry of asymmetric field blocking caused by the moving Y-collimator jaw in dynamic wedge operation, where P is a point of interest on the central ray of an asymmetric field at SAD, x is the lateral distance between the original open field central axis and the point P, and r is the size of the asymmetric field at SAD.***

The dose in phantom to the point on the central ray of a specific asymmetric dynamic field at the depth of d_{max} can be found using the following equation[14]:

$$D(d_{max}, x, r) = k \cdot MU \cdot CF(r, 0)\, SF(r, 0)\, OAR_{d_{max}}(x) \quad , \qquad (4.6)$$

where *MU* is the calculated number of monitor units, k is the calibrated dose per MU, which is typically 1 cGy/MU at the depth of d_{max} for a 10×10 cm^2 static symmetrical field, *CF(r,0)* is as defined in Eq. (4.5), *SF(r,0)* is the phantom scatter factor on the central axis of a static open field that has the same size as the chosen asymmetric dynamic field, and $OAR_{dmax}(x)$ is the beam profile measured in phantom at d_{max}. The effect of asymmetry is assumed to be described by one OAR term.

To find the dose delivered to a point at depth d below the phantom surface on the central ray of specific asymmetric dynamic field the following formula[14] can be used:

$$D(d, x, r) = k \cdot MU \cdot CF(r, 0)\, SF(r, 0)\, PDD(d, r, 0)\, OAR_d(x) \quad , \qquad (4.7)$$

where *PDD(r,d,0)* is the percentage depth dose for an open field that is the same size as the asymmetric dynamic field, and OAR_d is the beam profile measured at a depth d in phantom. Equation 4.7 shows that the dose at a point *(d,x)* on the central ray of an asymmetric dynamic field can be found by the product of the percentage depth dose for a symmetric open field and the off-axis ratio at the same depth in the medium.

4.3.4 Dynamic beam delivery system

In the Clinac 2300 C/D dynamic wedge mode, the Dynamic Beam Delivery system (DBD) modulates the dose rate and Y-collimator velocity simultaneously to create wedge shaped beam profiles. To accomplish this task, the DBD system requires that the treatment field be decomposed into linear segments in order for the dose to be uniquely specified for a specific reference point in each segment. These segments are defined as Y-collimator motor drive axis positions which are monitored by position sensitive potentiometers in the Clinac 2300 C/D treatment head. These axis drive positions determine when the dose rate should change. The segments are predefined in the STTs for the dynamic wedge, selected by the operator, and the STTs are stored permanently in the Varian C-Series computer hard drive.

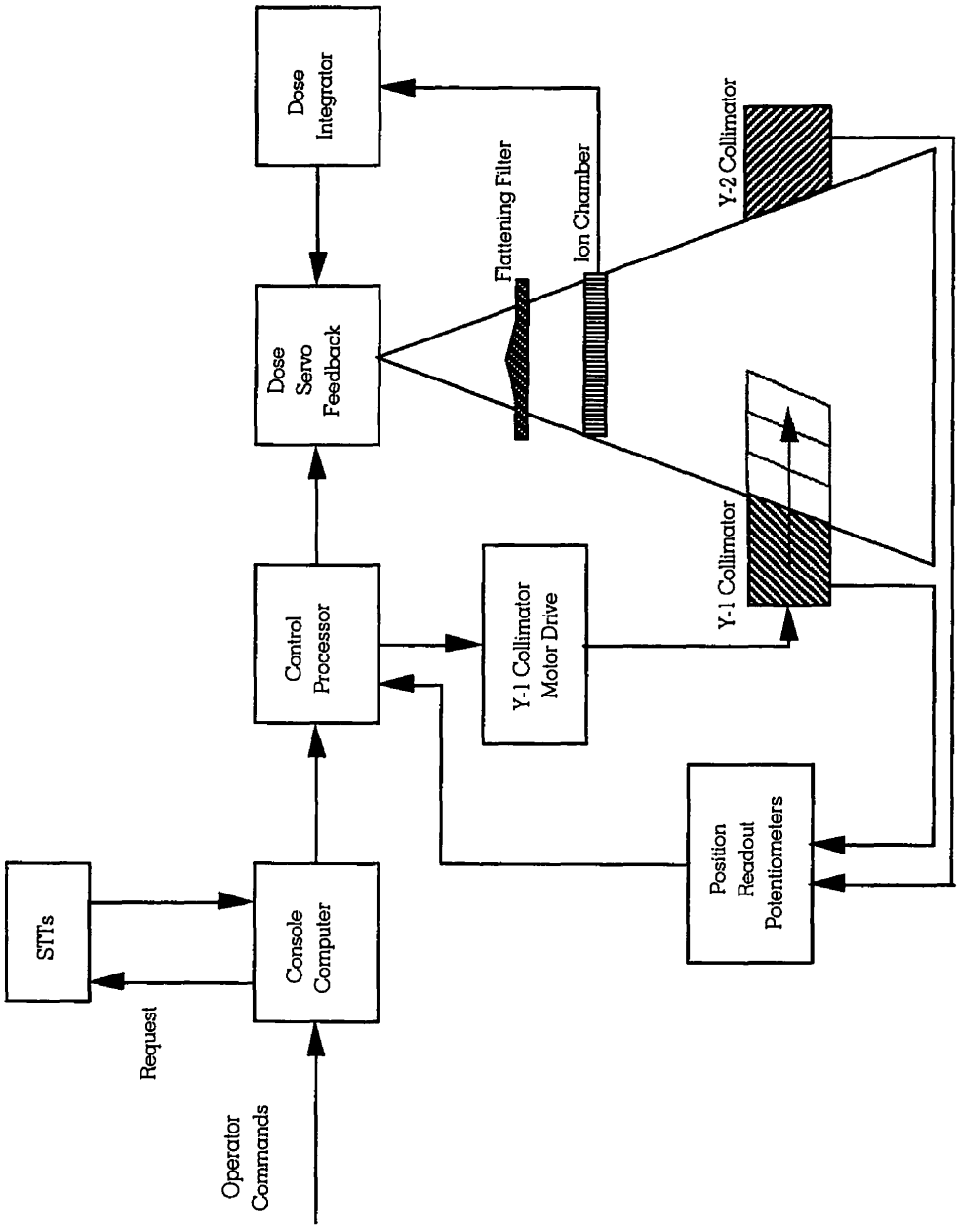

FIGURE 4.9. ***Block diagram of the Varian Dynamic Beam Delivery (DBD) System.***

The dynamic wedge operation can be summarized in the following series of steps:

1. *The operator selects the dynamic wedge treatment mode on the console computer, which engages the DBD system software.*

2. *The operator chooses the desired treatment parameters such as beam energy, field size, wedge angle, and number of delivered monitor units.*

3. *The console computer selects the correct STT from the hard disk. The monitor units per field segment are calculated and sent to the control processor.*

4. *Following the initiation of "beam on", the control processor modulates the dose rate and collimator velocity concurrently while minimizing the treatment time.*

Figure 4.9 shows a block diagram of the dynamic wedge operation. Once the DBD system starts, the appropriate segmented treatment table is retrieved from the hard drive. Since the STT only specifies the cumulative percentage of the total dose delivered for each field segment, the absolute dose per segment is calculated in the console computer. This information is then sent to a microprocessor which controls the dose rate and jaw velocity and ensures that the appropriate dose per field segment is delivered and that the treatment time is optimized. If the control microprocessor cannot maintain the needed dose per segment an interlock is triggered that prevents any further beam output. If the treatment is interrupted before the prescribed dose has been delivered, the DBD has the capability of delivering a partial treatment. The operator must specify the number of monitor units needed to deliver the remaining portion of the prescribed dose and the DBD system, with the help of the SST, will determine where the collimator motor axis must be placed to resume treatment. There will be no radiation output until the motor axis reaches the appropriate point and the remaining treatment is then delivered as planned.

4.3.5 Segmented Treatment Tables

The segmented treatment tables (STTs) play an important role in the delivery of dynamic wedge treatments. The STTs specify the fraction of the total dose delivered as a function of jaw position needed to generate the operator-selected wedge beam profile. Table 4.1 is an example of a typical STT text file for a 20 cm wide, 45° dynamic wedge field. The header contains the information needed to read and implement the data contained in the STT and designates the dynamic wedge selected by the operator. The numbers in the left-hand column represent the delivered monitor units in binary form. The right-hand column

TABLE 4.1. ***A typical segmented treatment table for a 20x20 cm^2 45° dynamically wedged 6 MV photon beam. The numbers in the left-hand column represent the delivered monitor units in binary form. The right-hand column represents the Y-collimator position.***

60C6
DWEDGE\WA1403.STT
VRNDW
MNF DWMA 2300C/D 6MV 132
UofU 2100C 6MV-->2300C/D 15-60 Deg CNVTD 6/3/92
6 MV 200 mm 45 deg
1
2
39

0	-400
20298	-400
20298	-392
20724	-372
21162	-352
21605	-332
22059	-312
22519	-292
22990	-272
23476	-252
24009	-232
24532	-212
25084	-192
25592	-172
26174	-152
26792	-132
27430	-112
28120	-92
28847	-72
29632	-52
30458	-32
31353	-12
32179	12
32997	32
33899	52
34811	72
35849	92
36992	112
38241	132
39616	152
41138	172
42928	192
44936	212
47172	232
49697	252
52584	272
55936	292
59795	312
65535	320

represents the Y-collimator position. It is more illustrative to use a normalized STT table, as shown in Table 4.2. The dose in this table represents the cumulative dose in MU, so this STT is for a dynamic wedge treatment delivering a total of 100 MU. Additionally, the first two rows specify an initial open field dose of 40.27 MU, as indicated by the fact that the dose is incremented from 0 MU to 47.27 MU while the collimators remain in the same position. Also, during this particular treatment, the Y-collimator sweeps from its starting position at -10 cm and closes to a final position of +9.5 cm (i.e., it travels a total of 19.5 cm).

The final field opening is always 0.5 cm regardless of the STT selected from the Clinac 2300 C/D hard drive. The STT data of Table 4.2 can be manipulated to give further insight into the dynamic wedge. Examples of this are shown in Figures 4.10 and 4.11. Figure 4.10 is a graphical representation of the STT, in integral form, showing the cumulative fractional dose in MU delivered for each jaw position. Figure 4.11 is another graphical representation of the STT, this time in differential form, showing the difference in dose between adjacent field segments. From these two figures, some important characteristics may be noticed. First, a large amount of dose is delivered to the open field *before* the jaw starts to move. This represents the baseline dose delivered in the open field portion of the dynamic wedge treatment. Second, after this open field dose, very little dose is delivered until the jaw closes to about 90% of the original open field size. It should be noted that with different differential arrangements, isodose distributions with different nominal wedge angles will be produced.

4.3.6 Modulation of dose rate and collimator speed

During dynamic wedge treatments dose delivery and collimator motion are continuous. However, the collimator speed and dose rate change according to a pre-calculated pattern. The Varian Clinac 2300 C/D control system calculates the necessary dose rate and Y-collimator velocity to be used at each point in the treatment field before the treatment process begins. The result is that the dose rate and Y-collimator velocity always follow the same pattern for the same dynamic wedge setup (i.e., same photon beam energy, monitor units, field size, and wedge angle).

The control system modulates the dose rate and Y-collimator velocity for each particular field segment in such a way that the segments are delivered in the least amount of time. The dynamic wedge treatment time is minimized by using the maximum Y-collimator velocity for each field segment that permits the delivery of the necessary MUs within that

TABLE 4.2. ***A normalized segmented treatment table for a 20x20 cm^2 45^o dynamically wedged 6 MV photon beam.***

Dose (MU)	Collimator Position (cm)
0	-10
40.27	-10
40.27	-9.8
40.27	-8.8
40.55	-8.3
41.05	-7.8
41.63	-7.3
42.21	-6.8
42.84	-6.3
43.55	-5.8
44.28	-5.3
45.02	-4.8
45.91	-4.3
46.80	-3.8
47.73	-3.3
48.72	-2.8
50.14	-2.3
51.44	-1.8
52.57	-1.3
53.61	-0.8
54.83	-0.3
56.06	0.3
57.27	0.8
58.68	1.3
59.95	1.8
61.16	2.3
62.42	2.8
63.76	3.3
65.28	3.8
66.94	4.3
68.83	4.8
70.90	5.3
73.22	5.8
75.59	6.3
78.17	6.8
80.95	7.3
83.90	7.8
87.80	8.3
92.88	8.8
100.00	9.0

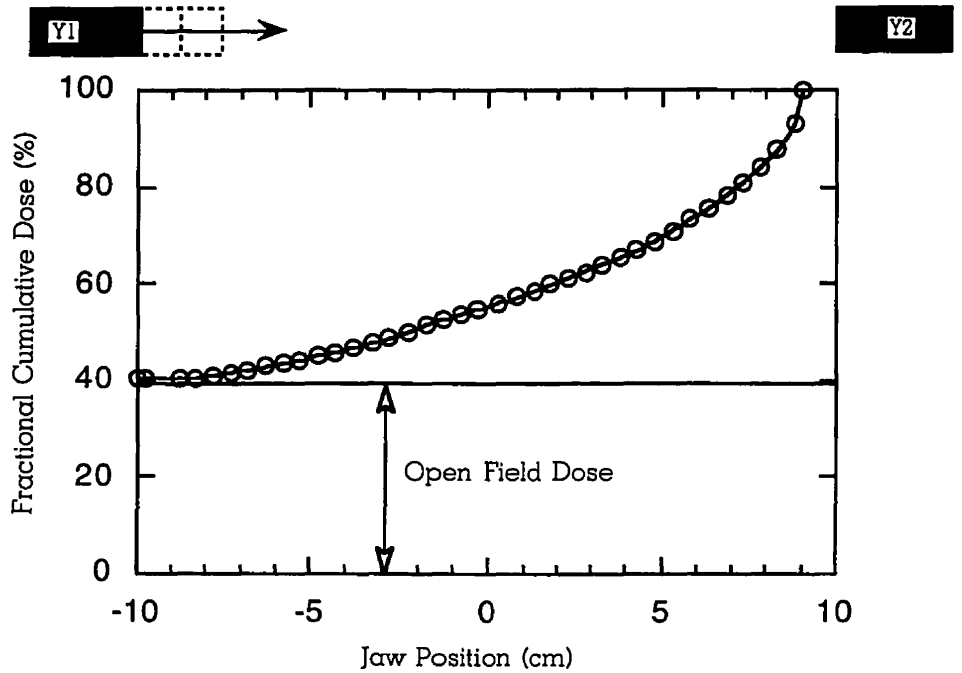

FIGURE 4.10. ***Integral representation of the STT found in Table 4.2.***

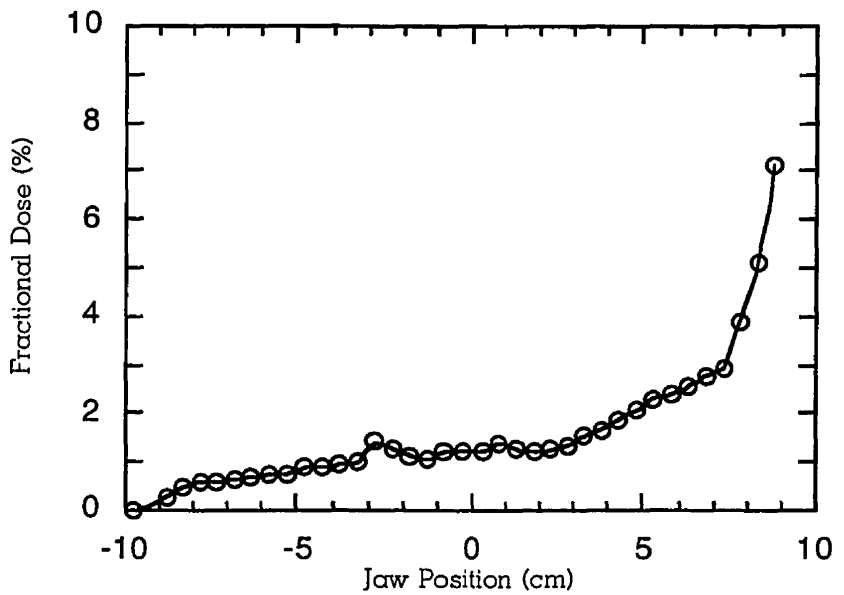

FIGURE 4.11. ***Differential representation of the STTfound in Table 4.2.***

segment. For segments that require a small amount of MUs to be delivered, the Y-collimator is set to move at maximum velocity, while the set dose rate is set below the maximum selected by the operator. For segments which require a large amount of delivered MUs, the Y-collimator is set to move at a slower velocity, while the set dose rate is changed to the maximum selected by the operator.

4.3.7 *Effective wedge factor*

Although the dynamic wedge does not attenuate the photon beam like conventional physical wedges do, there still is an *effective wedge factor (EWF)* which has to be accounted for, when a particular treatment plan calls for dose delivery with a dynamic wedge. As the Y-collimator moves, increasing amounts of the original open field are shielded causing an overall reduction in beam output. The *EWF* for the dynamic wedge is defined as the ratio, at depth of 10 cm on the beam central axis, of the integrated dose reading D_{10cm}^{wedge} for the dynamic wedge to the integrated dose reading D_{10cm}^{open} of the open field, for a fixed number of monitor units.[6] Mathematically speaking:

$$EWF = \frac{D_{10cm}^{wedge}}{D_{10cm}^{open}} \tag{4.8}$$

The *EWF*s are greater (closer to unity) than physical wedge factors and depend on field size, beam energy, and wedge angle.

4.3.8 *Dynamic wedge angle*

The dynamic wedge angle is specified by a straight line that is drawn through two points on an isodose line a quarter of the field size on each side of the central axis. The two points are on the variable isodose line that crosses the central axis at a fixed depth of 10 cm (see Figure 4.12).[6,15,16] This is in contrast to the convention used with physical wedges for which the wedge angle is defined as a line tangent to the 80% or 50% isodose contour at a variable depth on the central axis.

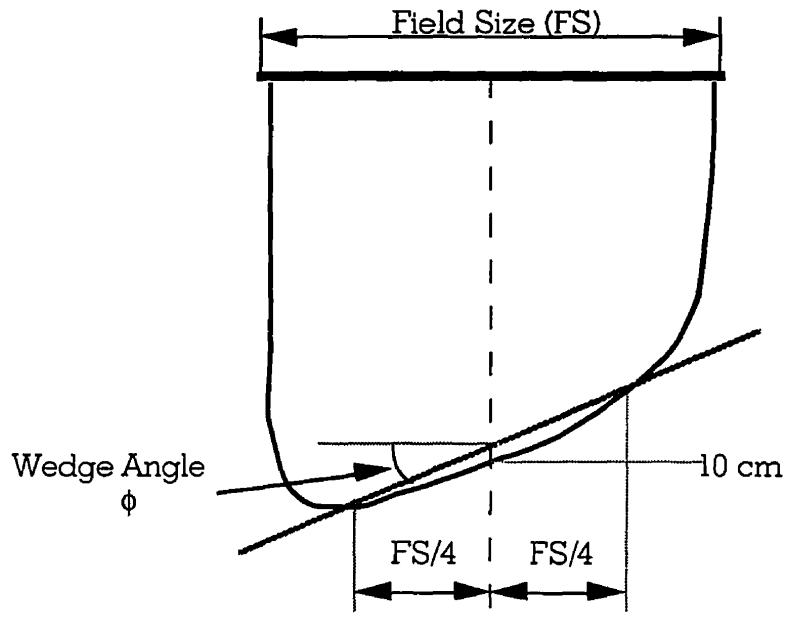

FIGURE 4.12. ***Definition of the dynamic wedge angle.***

4.4 Summary

The dynamic wedge is a modality of the Clinac 2300 C/D in which one of the upper collimator jaws (Y1 or Y2) moves in a continuous fashion to create a continuously decreasing field width while the beam is on. Since the field is continuously shrinking, different segments of the treatment field are exposed to the primary beam for different periods of time. During the entire procedure the dose rate and Y-collimator velocity are both modulated in accordance with a segmented treatment table (STT) in order to minimize the treatment time and create the desired wedge shaped isodose gradient.

The dynamic wedge offers the practical clinical advantage that no installations are necessary on the treatment head of the Clinac 2300 C/D. This makes it less cumbersome for the technicians who no longer have to lift the heavy physical wedge filters. Additionally, there is no longer a possibility of table collisions, and the optical display indicator is not blocked when the dynamic wedge is used. Future improvements will also allow the operator to select from a wider selection of wedge angles.

When considering the treatment of a patient, the dosimetric nature of the dynamic wedge offers improvements over the physical wedge filter. Before any radiotherapy treatment can be administered with the help of a wedge, the wedge factor must be accounted for.

4.5 References

1. E. Klein, D. A. Low, A.S. Meigooni, J. A. Purdy: *Dosimetry and clinical implementation of dynamic wedge*, Int. J. Radiation Oncology Biol. Phys. **31**, 583 -592 (1995).

2. F.G. Abrath, J. A. Purdy: *Wedge design and dosimetry for 25 MV X rays*, Radiol. **136**, 757-762 (1980).

3. F. M. Khan: The Physics of Radiation Therapy, 2nd edition. Williams & Wilkins, Maryland, U.S.A. (1994).

4. D.B. Hughes, C.J. Karzmark, R.M. Levy: *Conventions for Wedge Filter Specifications*, Br. J. Radiol. **45**, 868-872 (1972).

5. C.J. Karzmark, D. Angelo, R. Loevinger, P. Steed: *Notation and formulae for dose specification and calculations in radiotherapy*, Br. J. Radiol. **39**, 476-482 (1966)

6. ICRU report # 24, *Determination of Absorbed Dose in a Patient Irradiated by Beams of X or Gamma Rays in Radiotherapy Procedures*, International Commission on Radiation Units and Measurements, Washington, DC (1976).

7. J. R. Palta, I. Daftari, N. Suntharalingam: *field size dependence of wedge factors*, Med. Phys. **15**, 624-626 (1988).

8. E. C. McCullough, J. Gortney, C. R. Blackwell: *A depth dependence determination of the wedge transmission factor for 4-10 MV photon beams*, Med. Phys. **15**, 621-623 (1988).

9. Private communication with Calvin Huntzinger, Varian Oncology Systems, Varian Associates, Inc., Palo Alto, California.

10. T. Knoos, L. Wittgren: *Which depth dose data should be used for dose planning when wedge filters are used to modify the photon beam?*, Phys. Med. Biol. **36**, 255-266 (1991).

11. M. B. Podgorsak, S. S. Kubsad, B. R. Paliwal: *Dosimetry of large wedged high-energy photon beams*, Med. Phys. **20**, 369-372 (1993).

12. P. K. Kijewski, L. M. Chin, B. D. Bjarngard: *Wedge-shaped dose distributions by computer-controlled collimator motion*, Med. Phys. **5**, 426-429 (1978).

13. D. D. Leavitt, M. Martin, J. H. Moeller, W. L. Lee: *Dynamic wedge field techniques through computer-controlled collimator motion and dose delivery*, Med. Phys. **17**, 87-91 (1990).

14. F. M. Khan, B. J. Gerbi, F. C. Deibel: *Dosimetry of asymmetric x-ray collimators*, Med. Phys. **13**, 936-941 (1986).

15. IEC Performance Standard 976, *Medical Electron Accelerators - Functional Performance Characteristics*, International Electrotechnical Commission, Geneva (1989).

16. C. J. Huntzinger: *Dynamic Wedge: A Physicist's Perspective*, Varian Dynamic Wedge Users' Meeting Proc. (Calgary 1992).

MEASUREMENT OF DOSIMETRIC DATA

5.1 Introduction

In the application of ionizing radiation to medical problems, it is necessary to measure the amount of radiation delivered to the patient undergoing a particular procedure. In diagnostic procedures, such as low energy x-ray examinations, Computed Tomography (CT) scans, and Positron Emission Tomography (PET), radiation is measured to ensure optimal image quality and to provide information needed for radiation protection purposes. In radiotherapy procedures, on the other hand, a large dose of radiation is delivered to the tumor volume with an intent to cure the disease, and the efficacy of the treatment depends upon delivering the dose with a typical accuracy of ±5% or better.[1]

One of the major roles of medical physicists working in radiotherapy is to ensure an accurate delivery of the prescribed dose to the tumor, while sparing the healthy surrounding tissue. This chapter discusses the typical dosimetric equipment and measurement techniques that are used in a standard radiotherapy clinic to measure the amount of radiation delivered to the patient.

5.2 Dosimetric phantoms

Generally, it is not possible to measure dose distributions directly in patients that are being irradiated. Therefore, the data required to produce the dose distributions in patients is derived from measurements in water phantoms. Water is the most commonly used phantom material, since it closely approximates the absorption and scattering properties of soft tissue and muscle (the human body being 75% of water by weight[2]). Since water is naturally abundant and cost effective, and has universally reproducible radiation properties, it has become a standard phantom material for radiotherapy measurements.[3]

Even though water is the standard phantom for the dosimetry of photon and electron beams, it is not always feasible or practical to perform dosimetric measurements in a water phantom. For example, ionization chambers can experience severe leakage effects when submerged in water. It is also difficult to make surface dose measurements near the water surface because of its surface tension, resulting in uncertainty in chamber positioning.[4] Furthermore, water is not suitable for use with film dosimetry. Therefore, solid dry phantoms with attenuation and scattering properties resembling those of water have been developed as practical alternatives to water phantoms.

If a phantom is to be acceptable as a water equivalent substitute for photons, the radiation absorption and scattering properties for a given thickness of the substitute should be the same as those of the same thickness of water. This requires that the substitute and water have matched mass attenuation coefficients and matched electronic densities. One way to match the mass attenuation coefficients is to use a technique called the *basic data* method.[5] In this method, basic interaction data are used to form a combination of weighted mass attenuation coefficients. For example, if the mass attenuation coefficient at a specific photon energy for water $(\mu/\rho)_{water}$ is to be matched in a two-component substitute made up of a primary material A and a corrective filler B with mass attenuation coefficients $(\mu/\rho)_A$ and $(\mu/\rho)_B$, respectively, the *basic data* mixture rule will give:

$$\left(\frac{\mu}{\rho}\right)_{water} = w_A \times \left(\frac{\mu}{\rho}\right)_A + w_B \times \left(\frac{\mu}{\rho}\right)_B \quad , \tag{5.1}$$

where w_A and w_B are the proportions by weight of the substitute materials A and B, respectively. If required, one can use as many elements as needed to create a substitute material. Therefore Eq. (5.1) can be generalized as:

$$\left(\frac{\mu}{\rho}\right)_{water} = \sum_i w_i \times \left(\frac{\mu}{\rho}\right)_i \quad , \tag{5.2}$$

where w_i is the proportion by weight of the i^{th} element with the corresponding mass attenuation coefficient $(\mu/\rho)_i$. Using this method Constantinou et. al.[6] fabricated an epoxy resin-based solid water substitute called *Solid Water* currently commercially available from RMI, Middleton, Wisconsin. The radiation characteristics of Solid Water are very close to those of water. So close, in fact, that the immersion of massive slabs of Solid Water into a water phantom results in negligible change in the reading of a dosimeter in front of or behind the phantom irradiated by a photon beam.[7] Thus, Solid Water has been

proven to be a more reproducible and satisfactory water substitute than any other material used previously.[8] Additionally, Solid Water is convenient to work with, easy to machine, and does not exhibit any charge storage effects.[9,10]

5.3 Ionization dosimeters

The most common instrument for measuring the radiation properties of a radiotherapy beam is an ionization dosimeter. Frequently, the ionization dosimeter is thought of as a single instrument. However, it actually consists of three distinct components: an ionization chamber, a connecting cable, an electrometer, and a cable connecting the two.

5.3.1 Ionization chambers

Ionization chambers take advantage of the fact that an x-ray beam, in passing through a medium, sets electrons in motion via one of several possible effects, most notably the photoelectric effect, Compton effect, and pair production. These high-velocity electrons generally possess enough energy to generate ion pairs along their path-lengths be it in a medium or in a gas-filled cavity inside the medium. With the use of an electric field in the chamber cavity, applied between ion-collecting electrodes, the positive ions migrate toward the negative electrode and the negative ions move toward the positive electrode. The result is a radiation induced current that can be measured and related to the amount of radiation absorbed in the volume of gas, usually air, between the electrodes.

5.3.2 Farmer-type chamber

The Farmer type chamber, shown schematically in Fig. 5.1, was introduced in 1955 by F.T. Farmer.[11] Since then design modifications have been made in order to improve energy response characteristics and introduce more consistency in the design. As a result, the Farmer-type chamber has gained widespread acceptance and has become the most popular ionization chamber in clinical use today.

The Farmer chamber used in our experiments is a Nuclear Enterprises model 2571 ionization chamber (Fig. 5.1). It can be used to measure dosimetric properties of photons as well as electrons at therapy level dose rates on the order of 100 cGy/min. This chamber consists of a thin wall (0.36 mm) made of high purity graphite surrounding a small (0.69 cm^3) collection volume of air. The wall is coated on the inside with a conductive material composed of "aqua-dag" to form an outer electrode. A voltage is applied between this outer electrode and a pure aluminum central electrode to collect the charge produced in the vol-

ume of air due to irradiation. In the system depicted in Fig. 5.1 the high voltage is applied via a triaxial cable whose central conductor is grounded through an electrometer and surrounded by insulator material which in turn is surrounded by the inner braid of the triaxial cable. The inner braid is connected to ground directly and surrounded by an insulator layer and the outer braid. The outer braid is used to carry the high voltage to the chamber outer electrode. With this design the central electrode is surrounded by ground at all places except in the sensitive volume where it "sees" the high voltage across the air gap. The chamber is guarded to within 30 mm of the sensitive volume, resulting in a low natural leakage current and in reduced irradiation induced stem effects.

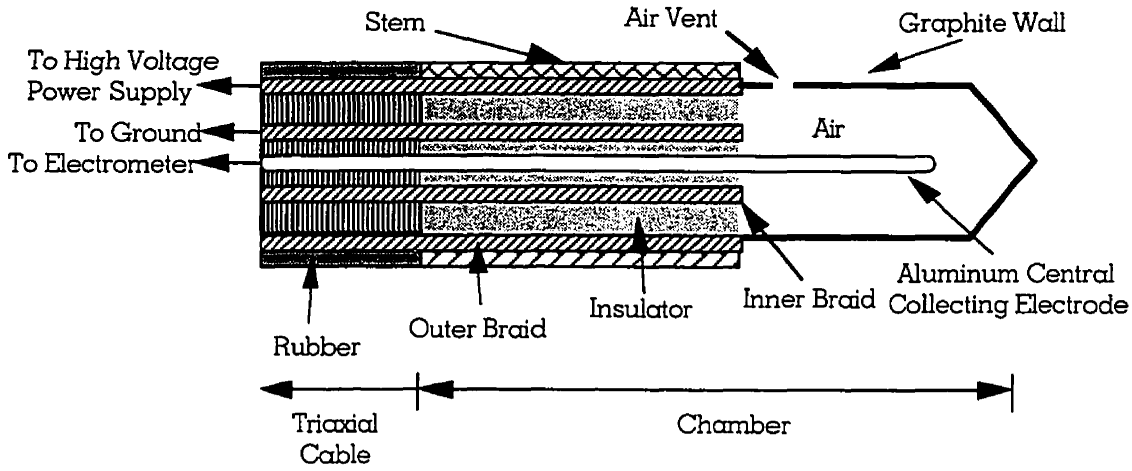

FIGURE 5.1. *Schematic diagram of the Nuclear Enterprises 2571 Farmer-type ionization chamber.*

5.3.3 Parallel plate chamber

An Attix plane-parallel ionization chamber, shown schematically in Fig. 5.2, was used to measure absorbed dose in the buildup region of the phantom. It uses two parallel electrodes spaced very closely (1 mm) to each other to create a sensitive volume with the use of electric fields. The front electrode, or end window, serves as the polarizing electrode and is made of a 0.025 mm thick Kapton conductive film. For safety, the window is kept at ground potential during operation. This is accomplished by connecting a grounded outer braid of a triaxial cable to the window. The collecting electrode is constructed from a polyethylene disk (0.1 mm x 12.7 mm diameter) coated with a minimal thickness of conducting colloidal graphite. The ionization processes that take place in the chamber sensitive volume (0.127 cm^3) create ion pairs that are acted upon by an electric field and collected.

by either the collecting electrode or polarizing electrode. The electric field lines are kept uniform throughout the sensitive chamber volume with the use of a guard ring. The high voltage supplied to the guard ring comes from the inner braid of the triaxial cable. The chamber body is constructed almost entirely from Solid Water. This provides negligible photon beam perturbation when used in conjunction with a Solid Water phantom.

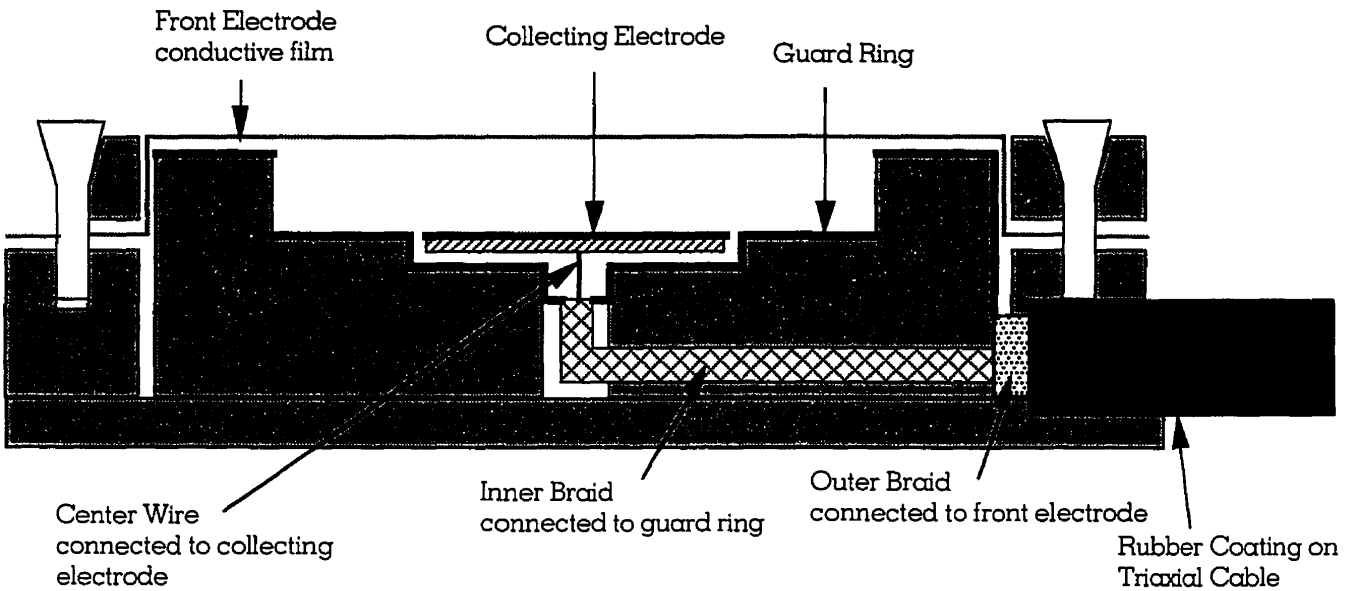

FIGURE 5.2. ***Cross sectional view of the Attix Parallel-Plate Ionization Chamber, Model 449.***

When one uses a parallel plate chamber, proper care must be taken to account for the so called *polarity effect* which occurs when a photon beam is incident upon the chamber, and electrons are ejected out of the collecting electrode with a resulting current flow to replenish these electrons. This current, sometimes referred to as *Compton current*, will be in the same direction regardless of the voltage source polarity. The total signal for a positive polarity voltage source (I_{pos}) will be a summation of the ionization current (I_{ion}) produced by the collection of ion pairs and the Compton current (I_{comp}). For the case of negative voltage source polarity (I_{neg}) the induced ionization current will oppose the Compton current. Averaging I_{pos} and I_{neg} will yield the actual current:

$$I_{ave} = \frac{I_{pos} + (-I_{neg})}{2} = \frac{(I_{ion} + I_{comp}) - (-I_{ion} + I_{comp})}{2} = \frac{2I_{ion}}{2} = I_{ion} \ , \qquad (5.3)$$

After charged particle equilibrium is attained I_{comp} is compensated by the scattered electrons ejected from the phantom material placed on top of the chamber and landing on the collecting electrode. These scattered electrons replenish the missing "Compton" electrons on the collecting electrode (electronic equilibrium) and as a result, I_{pos} and I_{neg} become equal and only one voltage source polarity is used for measurements after the depth of d_{max}.

5.3.4 Triaxial cables

Originally, each cable-connected ionization chamber was manufactured with its own attached cable. Now it has become customary to have approximately two meters of cable attached to the chamber and to install a low noise triaxial cable in the treatment room. This arrangement is practical since the cable can be made to any custom length and can be used with many different chambers. A permanently installed cable also saves time and reduces wear and tear on the chamber connector post. And most importantly, if the cable gets damaged the chamber itself will not be affected. In general, a good cable will have a fast equilibration time (< 1 min) with a change in high voltage, low radiation induced signal, and low leakage effects (< 10^{-14} A). Additionally, the cable should be flexible yet sturdy.

5.3.5 Electrometer

Typical currents produced in an ionization chamber are very small and cannot be measured readily with an ammeter. For this reason special electrometers are used which incorporate negative-feedback operational amplifiers (op amps). Op amps are solid state amplifiers with large gains (>10^4) and high input impedances (>10^{12} ohms) which maintain a very small potential difference (20-100 mV) across the inputs. This is an important feature, since all of the voltage will be dropped across the feedback element. Figure 5.3 shows a total capacitive feedback circuit which is used in the electrometer to integrate current measurements resulting in measured charge. The op amp is represented schematically by the triangle and the negative and positive input designations refer to the inverting and non-inverting inputs, respectively.

In Figure 5.3, the circuit has a unity gain so that all of the charge collected by the ionization chamber collecting electrode is deposited on the feedback capacitor C. The voltage induced across C can be found using the formula:

$$Q = C \times V \quad , \tag{5.4}$$

where Q is the collected charge, C is the capacitance, and V is the voltage. This implies that if the voltage is read across the capacitor with a voltmeter, and the capacitance is known, then the product of these two values will yield the total charge collected in Coulombs.

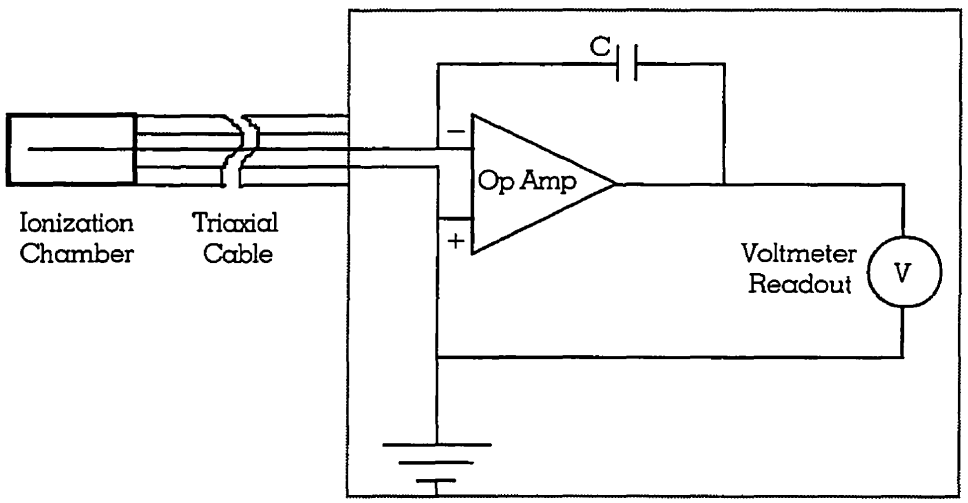

FIGURE 5.3. ***A total capacitive negative feedback circuit used in electrometers to integrate ionization measurements.***

5.4 Therapy beam analyzer

Part of the dosimetric data for the dynamic wedge was measured with a Gammex TM-3m microprocessor based therapy beam monitor, shown schematically in Fig. 5.4. It can be used to measure radiation output, beam flatness, symmetry, and beam energy. This particular detector has the unique feature that it contains five parallel-plate ionization detectors, each having a radius of 2 cm and a sensitive volume of 0.7 cm^3. The ionization chambers are embedded 4.8 mm underneath the face of a 25.4 cm × 27.9 cm × 1.6 cm acrylic plate. The maximum field size that can be accommodated is 20×20 cm^2. When the TM-3m is operated, only three detectors can be used simultaneously to collect data at the same time. The operator has the option of selecting detectors 1 and 2 or detectors 3 and 4. Once the appropriate detectors are selected, all signals will be given relative to the central reference detector. The TM-3m is connected to a special Gammex 5-channel electrometer with the use of a standard multi-coaxial cable. The electrometer has three 4.5 digit liquid crystal

displays, one for each detector in a particular setup, and can integrate measurements for all detectors selected.

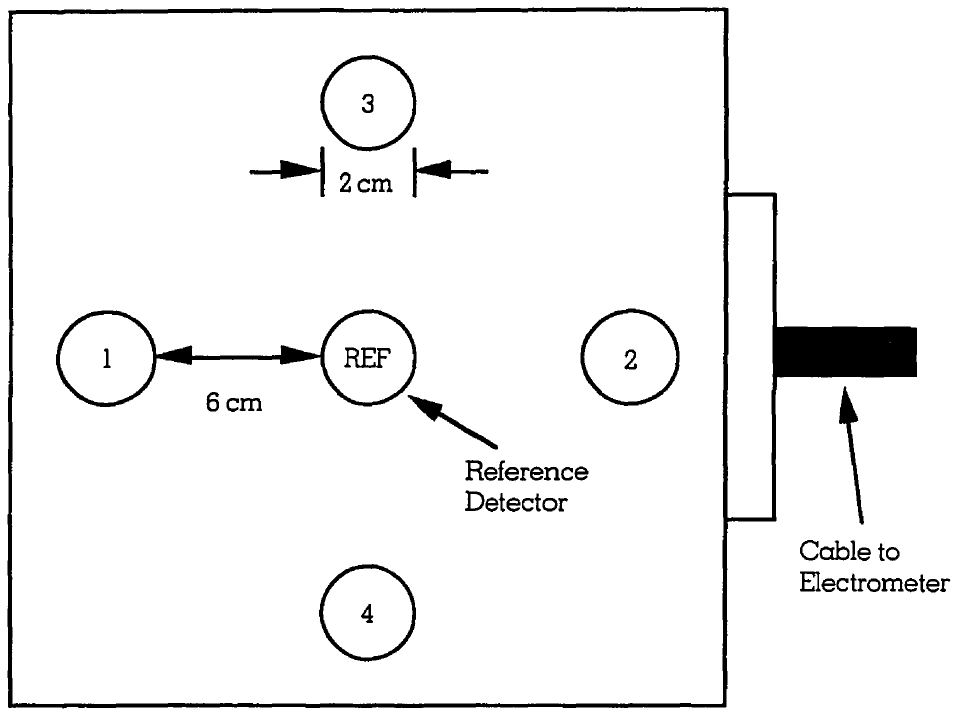

FIGURE 5.4. ***Schematic illustration of the Gammex TM-3m Radiation Beam Analyzer used to collect parts of the dynamic wedge dosimetric data.***

5.5 Three-dimensional water scanner

Beam data from the Clinac 2300 C/D linac was collected with the use of an RFA-300 Radiation Field Analyzer (Scanditronix, Upsalla, Sweden) which can perform linear scans to measure depth doses, beam profiles and two-dimensional isodose distributions. The RFA-300 can also be used as a two-dimensional film densitometer. When linear scans are carried out, a water phantom is used that consists of a water filled plastic tank and a set of very small cylindrical RK ionization detectors (0.03 cm^3). The RK ionization detector is a sealed thimble type ionization chamber that can be used in water and is suitable for electron or photon beams of energies above 1 MV.

The water tank is fitted with a positioning servo mechanism that allows for a field detector to be positioned anywhere in the 50x50x50 cm^2 three dimensional scanning volume. This detector is fastened in place with the help of a snap-in detector holder that ensures accu-

rate positioning. Since the output of the Clinac 2300 C/D linac varies with time, a stationary reference detector is also used when static open and wedged fields are investigated. The relative signal between the field and reference detectors is stored by the RFA-300 computer control unit, a 486 based PC compatible with a 16-bit math co-processor.

5.6 Film dosimetry

Film dosimetry is an attractive alternative to ionization chamber measurements for measuring megavoltage beam characteristics. It provides a quick and convenient method for obtaining a complete set of isodose curves in the plane of the film with a distinct advantage over the information yield of one data point per measurement which characterizes ionization chamber techniques. Film also has the highest spatial resolution of any practical dosimeter used in radiotherapy departments.[12] On the other hand, film only serves as a relative dosimeter because the radiation sensitive photographic emulsion does not approximate the atomic composition of biological tissues. For this reason film is calibrated with the use of sensitometric curves which relate the measured optical film density to known radiation doses. In addition, the process by which the absorption of energy is transformed into blackening of the film is controlled by many physical and chemical steps that complicate further the approach to absolute dosimetry.[13]

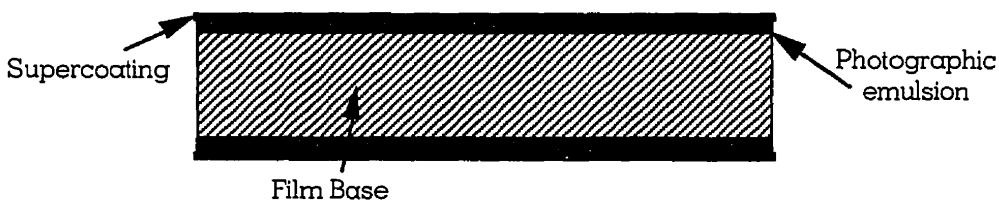

FIGURE 5.5. ***Cross section of a Kodak X-Omat V Radiotherapy Verification Film.***

Kodak X-Omat V Radiotherapy Verification Film (Fig. 5.5) was used for film dosimetry experiments. The X-Omat V film is composed of a thin (~0.1 mm) gelatin base-layer, covered on both sides with a radiosensitive photographic emulsion (~0.01 mm thick). As radiation is incident upon this photographic emulsion, chemical changes occur so that when the film is developed the exposed sections appear opaque and the unexposed sections appear translucent.

The amount of blackening of the irradiated film is expressed in terms of the optical density (*OD*), which is a function of the amount of light transmitted through a darkened portion of the film. The *OD* is defined mathematically as follows:

$$OD = \log\left(\frac{I_o}{I_t}\right) \quad , \tag{5.5}$$

where I_o and I_t are the intensities of a light beam incident upon and transmitted through the film, respectively.

There are two main reasons for representing the optical density as a logarithm. Firstly, with logarithms large differences in numerical values can be represented accurately on a small scale. For example, a change in optical density from 2 to 1 represents a factor of 10. Secondly, the physiological response of the human eye to differences in light intensity is essentially logarithmic in nature.[14]

The variation in the observed optical density as a function of dose is represented by the *sensitometric curve*. Sensitometric curves are found by giving a film a series of known doses, developing the film, and plotting the resulting optical density against the known dose to the medium in the absence of film.[15] The shape of this curve depends upon the type of photographic emulsion used by the film.

Typical processing requires passing the film through a developer mixture, fixer solution, and water bath. The slope of the sensitometric curve is also a function of processing conditions such as developer temperature and development time. Since these parameters can change daily, relative measurements between any series of films we used in our experiments were batch processed at the same time to reduce any minor film-to-film variations. Measurements were also restricted to films of the same batch. When films are processed at different times the error can be as large as ±5%.[15]

In order to find the sensitometric curves for the 6 MV and 18 MV photon beams generated by the Clinac 2300 C/D linac, films were placed perpendicular to the beam central axis at the depth of dose maximum d_{max} in a Solid Water phantom as shown schematically in Fig. 5.6. The surface of the Solid Water was placed at an *SSD* of 100 cm. A series of known doses was delivered to d_{max} in order to find the optical density as a function of dose. All films were batch processed in a Fuji RGII x-ray automatic film processor. After development the resulting optical densities were determined using a calibrated MacBeth densito-

meter, enabling the calculation of the sensitometric curves shown in Fig. 5.7. This figure also demonstrates that the X-Omat V film is relatively independent of the megavoltage beam energy at the depth of dose maximum d_{max} and that the optical density is linear with dose up to approximately 40 cGy.

In order to investigate whether or not the sensitometric curve is a function of depth in phantom, a series of doses were first delivered to films placed at d_{max} and the corresponding sensitometric curve was measured. Then the same doses were delivered to films at a depth of 20 cm in phantom to generate a second sensitometric curve. This process was performed for both 6 MV and 18 MV photon beams and the resulting sensitometric curves are presented in Figs. 5.8 and 5.9, respectively. It can be seen that the sensitometric curves are essentially independent of the depth of measurement in phantom, which of course can be expected since, as shown in Fig. 5.7, the film response is independent of photon beam energy.

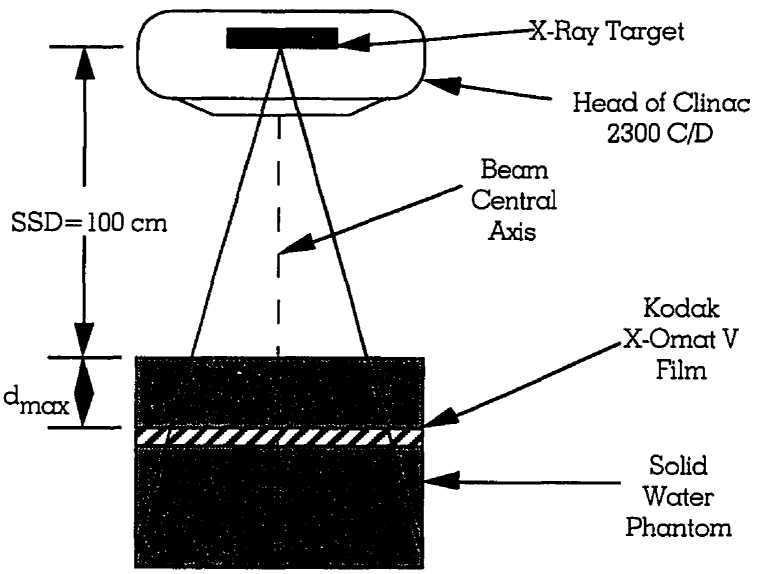

FIGURE 5.6. ***The perpendicular film geometry used to measure the optical densities needed to establish the sensitometric curve.***

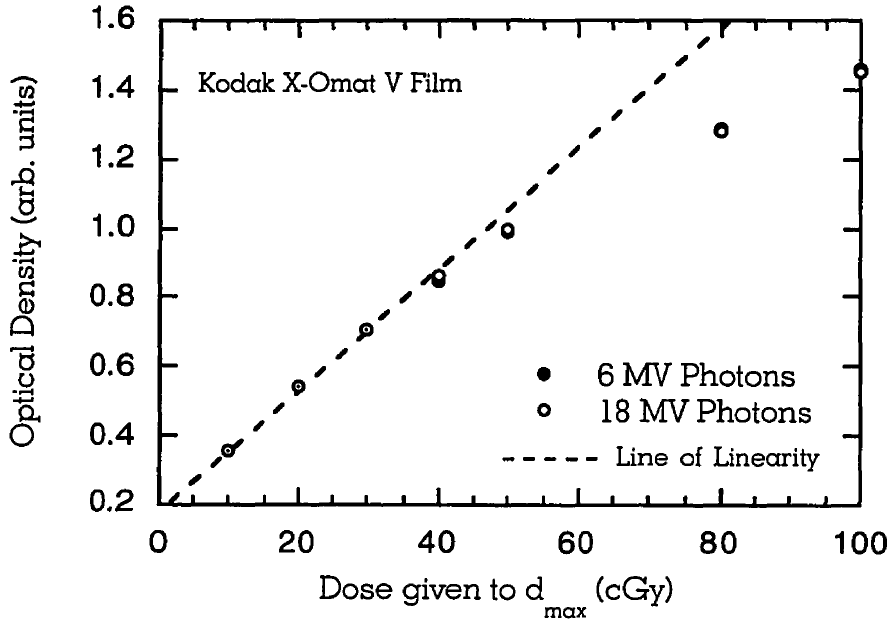

FIGURE 5.7. ***Sensitometric curves for 6 MV and 18 MV photon beams from a Clinac 2300 C/D. Also shown by the dashed line is the line along which the relative optical density is linearly proportional to the dose.***

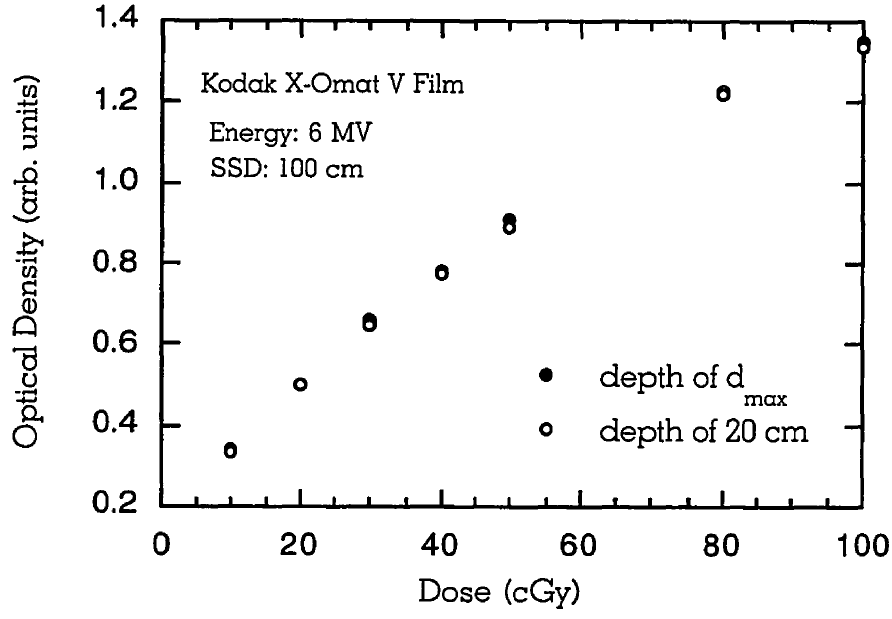

FIGURE 5.8. ***Sensitometric curves at depths of d_{max} and 20 cm in phantom for a 6 MV photon beam.***

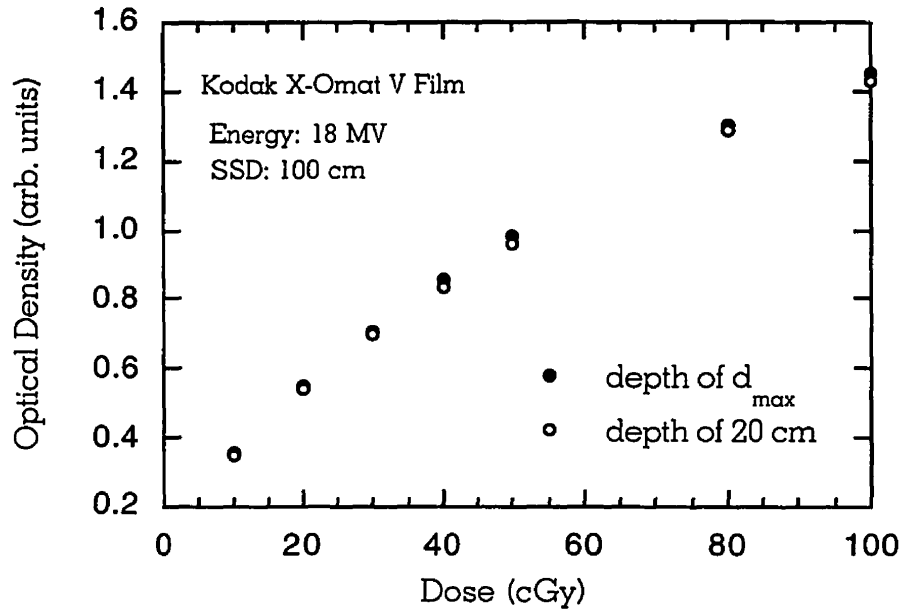

FIGURE 5.9. ***Sensitometric curves at depths of d_{max} and 20 cm in phantom for a 18 MV photon beam.***

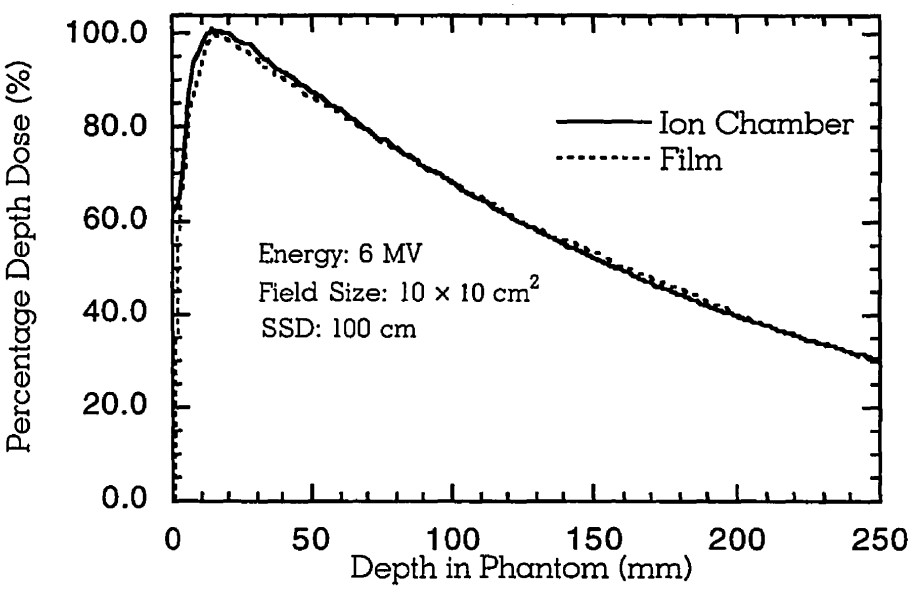

FIGURE 5.10. ***Comparison of the PDD obtained by film measurements and ion chamber measurements for a 10 × 10 cm^2 6 MV photon beam. Film was place in perpendicular geometry.***

In the linear region of the sensitometric curve the net optical densities normalized to d_{max} are equal to the percentage depth doses of the beam obtained by an ionization chamber as shown in Fig. 5.10. The net optical density is the optical density minus the emulsion base plus the background fog density, referred to as the base-plus-fog. The base-plus-fog density was determined by a non-irradiated film from the same batch and processed at the same time as the irradiated films.[15] When properly handled the film data may be within ±3% of ion chamber measurements.[12,16,17]

5.7 References

1. ICRU report # 24, *Determination of Absorbed Dose in a Patient Irradiated by Beams of X or Gamma Rays in Radiotherapy Procedures*, International Commission on Radiation Units and Measurements, Washington, DC (1976).

2. C. Zankowski: *Monte Carlo analysis of the 10 MV x-ray beam from a Clinac-18 linear accelerator*, M.Sc. thesis, McGill University, Montreal, Canada (1994).

3. TG21, *A new protocol for the determination of absorbed dose from high-energy photon and electron beams*, Med. Phys. **10**, 741-771 (1983).

4. F. H. Attix: Introduction to Radiological Physics and Radiation Dosimetry, New York, John Wiley and Sons, 1986.

5. D. R. White: *Tissue substitutes in experimental radiation physics*, Med. Phys. **5**, 467-479 (1978).

6. C. Constantinou, F. H. Attix, B. R. Paliwal: *A solid water phantom material for radiotherapy x-ray and γ-ray beam calibrations*, Med. Phys. **9**, 436-441 (1982).

7. C. S. Reft: *Output calibration in solid water for high energy photon beams*, Med Phys. **16**, 299-301 (1989).

8. A. K. Ho, B. R. Paliwal: *Stopping power and mass energy-absorption coefficient ratios for solid water*, Med. Phys. **13**, 403-404 (1986).

9. A. K. Ho, B. R. Paliwal, F. H. Attix: *Charge storage in electron-irradiated phantom materials*, Med. Phys. **13**, 99-100 (1986).

10. F. M. Kahn: The Physics of Radiation Therapy, 2nd edition. Williams & Wilkins, Maryland, U.S.A. (1994).

11. L.J. Humphries, T. W. Slowey: "Dosimetry Instrumentation" in Radiation Oncology Physics - 1986 (AAPM Monograph No. 15) (1987).

12. J. F. Williamson, F. M. Kahn, S. C. Sharma: *Film dosimetry of megavoltage photon beams: A practical method of isodensity-to-isodose curve conversion*, Med. Phys. **8**, 94-98 (1981).

13. F.M Kahn, K.P. Doppke, K. R. Hogstrom, G. J. Kutcher, R. Nath, S. C. Prasad, J. A. Purdy, M. Rosenfeld, B. L. Werner: *Clinical electron-beam dosimetry: Report of AAPM Radiation Therapy Committee Task Group No. 25*, Med. Phys. **18**, 73-109 (1991).

14. T. S. Curry, J. E. Dowdey, R. C. Murry: Christensen's Physics of Diagnostic Radiology, 4th edition. Lea & Febiger, Philadelphia, U.S.A. (1990).

15. J. Dutreix, A. Dutreix: *Film dosimetry of high energy electrons*, Ann. N.Y. Acad. Sci. **161**, 33-43 (1969).

16. L. Patten, J. Purdy, G. Oliver: Automated film dosimetry [Abstract], Med. Phys. **1**, 110 (1974).

17. D. W. Anderson, F. St. George: *Comparison of Film and Ion Chamber Systems for Depth-dose Measurements for a 25 MV Beam*, Phys. Med. Biol. **24**, 636-638 (1979).

RESULTS AND DISCUSSION

As discussed in Chapter 5, a variety of dosimetric systems was used in the measurement of the photon beam characteristics provided by the dynamic wedge operating in the 6 MV and 18 MV x-ray mode on our Clinac 2300 C/D linear accelerator. Measurements were performed to verify that the dynamic wedge is operating linearly with the prescribed dose and dose rate. Also measured were the effective wedge factors, central axis percentage depth doses, wedge beam profiles, surface doses, doses in the build-up region, and treatment times for each of the four available dynamic wedges. Results of all our experiments with the dynamic wedge are presented and discussed in this chapter. Since this chapter contains a large number of figures dealing with measured data, all figures representing the measured data are presented sequentially at the end of the chapter (pages 91-111).

6.1 Effective wedge factors for the dynamic wedge

The effective wedge factors for the Clinac 2300 dynamic wedge were measured for all square field sizes ranging from 4×4 cm^2 to 20×20 cm^2 in 0.5 cm increments for the 15, 30, 45, and 60 degree dynamic wedge angles and both 6 MV and 18 MV photon energies (256 different wedge transmission factors in total). The effective wedge factors were measured with a Nuclear Enterprises 2571 Farmer-type ionization chamber (section 5.3.2) by comparing central axis readings for each dynamically wedged field to the stationary open field with the same field size in accordance with the definition stated in Eq. (4.8). All data was taken at depth of 10 cm in the Solid Water phantom at an *SSD* of 100 cm. The geometry of the experiment is schematically illustrated in Fig. 6.1.

The results of the effective wedge factor measurements are presented in Figures 6.2 and 6.3 (page 91) for 6 MV and 18 MV photons, respectively. The dynamic wedge factors depend strongly on field size, increasing as field size decreases. Additionally, there is a discontinuity in the wedge factors between the 9.5×9.5 cm^2 and the 10×10 cm^2 square fields. This occurs because the STT beam generation algorithm switches from beam weight reference point increments of 0.25 cm to increments of 0.5 cm, as described in Chapter 4. For dynamic field widths of 4 cm to 9.5 cm, a higher number of MUs is delivered to the field edges to compensate for lateral non-equilibrium conditions.[1] For dynamic

field widths of 10 cm and beyond, not as many MUs are required at the field edges since lateral electronic equilibrium conditions exist. This implies that the dynamic wedge delivers dose most effectively at field widths ranging from 10 cm to 20 cm.

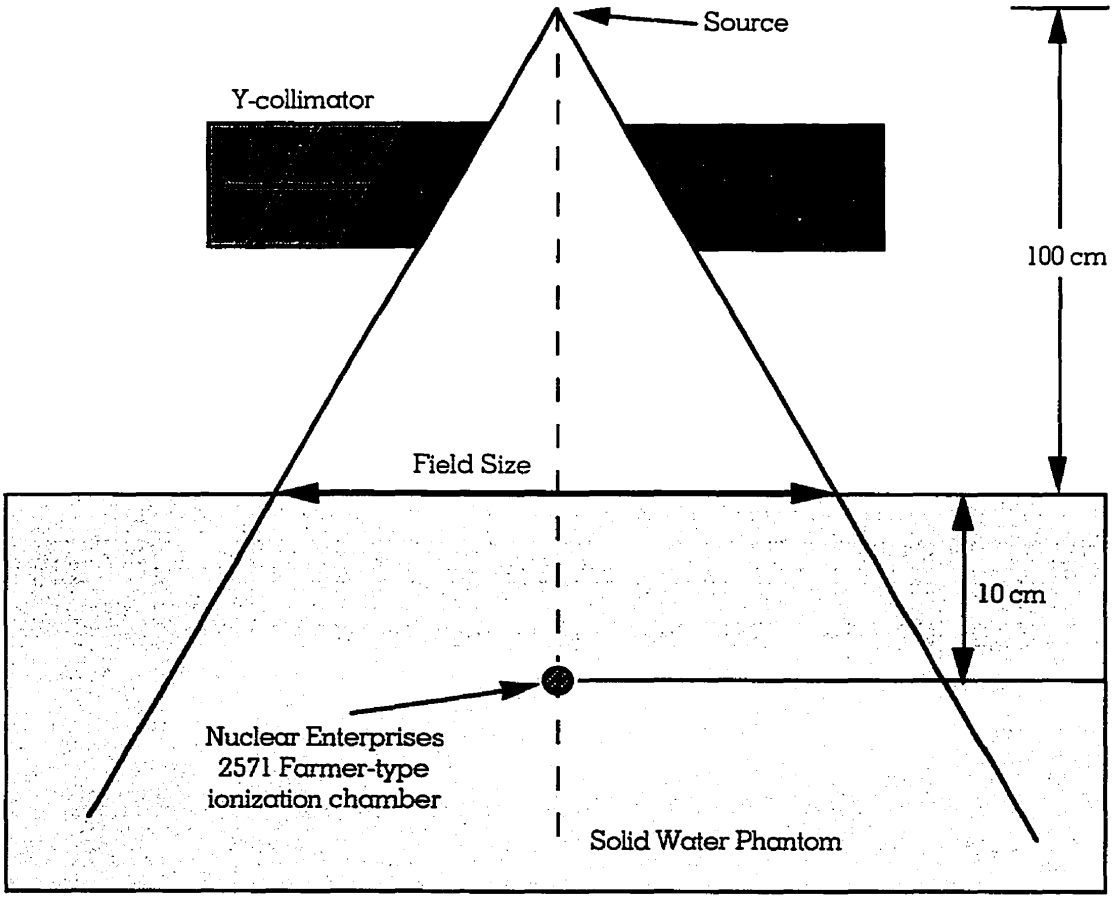

FIGURE 6.1. ***Schematic illustration of the geometry used to measure the effective wedge factors of the dynamic wedge. All measurements were performed with a Nuclear Enterprises 2571 Farmer-typed ionization chamber in Solid Water at a depth of 10 cm. Each central axis reading for the dynamically wedged field was divided by the central axis reading of the stationary open field with the same field size to find the effective wedge factors in accordance with the definition stated in Eq. (4.8). The effective wedge factors were found for all square field sizes ranging for 4×4 cm^2 to 20×20 cm^2 in 0.5 cm increments for all available dynamic wedges and both 6 MV and 18 MV photon energies. SSD: 100 cm.***

There are other small discontinuites noticeable in the measured effective wedge factors prevalent for the 60° dynamic wedge at large field sizes. Therefore, it is not possible to use simple interpolation calculations of a square field wedge factor table in order to find the number of monitor units needed to give the prescribed dose at d_{max}.

The effective wedge factor also include the decrease in scatter as the field size becomes smaller during the treatment process. This is important for large angle dynamically wedged fields, especially for the 60° wedge, which have a small initial open field duration. Measurements reveal that the effective wedge factors for the dynamic wedge are closer to unity than those for physical wedge filters suggesting that the dose is delivered more efficiently to the patient with the dynamic wedges since there is less attenuation of the photon beam. It should also be noted that the effective wedge factor is approximately equal to the fraction of MUs prescribed by the STT when the Y-collimator crosses the central axis.

The results indicate that the X-collimator setting does not influence the effective wedge factor, as shown in Tables 6.1 and 6.2, which give the measured wedge factors with variable x-collimator setting in comparison to nominal 4×4 cm^2 and 20×20 cm^2 fields for 6 MV and 18 MV photon beams, respectively. The results indicate that to within ±1%, the effective wedge factors depend only on the dynamic wedge field width (Y-setting) and not on the equivalent square of the field.

TABLE 6.1. ***Effective wedge factors for square fields of 4×4 cm^2 and 20×20 cm^2 and various rectangular fields. Photon beam: 6 MV.***

	4 × 4 cm^2	**4 × 8 cm^2**	**4 × 15 cm^2**	**4 × 20 cm^2**
15°	0.920	0.923	0.921	0.923
30°	0.889	0.893	0.893	0.893
45°	0.846	0.851	0.851	0.851
60°	0.783	0.785	0.786	0.786
	20 × 4 cm^2	**20 × 8 cm^2**	**20 × 15 cm^2**	**20 × 20 cm^2**
15°	0.752	0.752	0.753	0.753
30°	0.602	0.603	0.605	0.604
45°	0.488	0.489	0.492	0.492
60°	0.490	0.493	0.495	0.495

TABLE 6.2. *Effective wedge factor for square fields of 4×4 cm² and 20×20 cm² and various rectangular fields. Photon beam: 18 MV.*

	4 × 4 cm²	4 × 8 cm²	4 × 15 cm²	4 × 20 cm²
15°	0.828	0.830	0.830	0.831
30°	0.808	0.809	0.810	0.810
45°	0.779	0.780	0.781	0.780
60°	0.728	0.729	0.730	0.730
	20 × 4 cm²	20 × 8 cm²	20 × 15 cm²	20 × 20 cm²
15°	0.815	0.816	0.816	0.815
30°	0.698	0.698	0.698	0.698
45°	0.556	0.557	0.557	0.558
60°	0.470	0.471	0.472	0.473

6.2 Central axis percentage depth dose for the dynamic wedge

The central axis percentage depth dose (*PDD*) data for the dynamic wedge was measured using an RFA-300 water tank (described in Section 5.5), which contains a small volume RK ionization chamber that was positioned at different depths in water along the beam central axis with the use of a positioning servo mechanism. Each ionization signal was normalized to the signal at the depth of maximum dose d_{max} to yield a set of depth ionization values. Measurements were performed for all available dynamic wedges with field sizes of 4×4 cm², 10×10 cm², and 20×20 cm² for 6 MV and 18 MV photons. The geometry of this experiment is shown in Fig. 6.4.

The measured dynamic wedge central axis *PDD* data is in excellent agreement with the open field PDD data. The results of our experiments are given in Figures 6.5 through 6.10 (pages 92 through 97). All dynamic wedge data was within ±2% of the open field data. This is a significant contrast to the *PDD*s of physical wedge filters which can differ from open field data by as much as ~5% because of beam hardening effects produced by the wedges.[2,3] The similarity between the dynamic wedge *PDD* data and the open field data has the advantage of reducing the time in taking measurements, since the *PDD* data would otherwise have to be measured point by point for all dynamic wedge fields and beam energies. This is important not only for monitor unit calculations but also for treatment planning which, in some institutions, ignores the beam hardening effects caused by physical wedge filters possibly resulting in serious overdosing of patients.

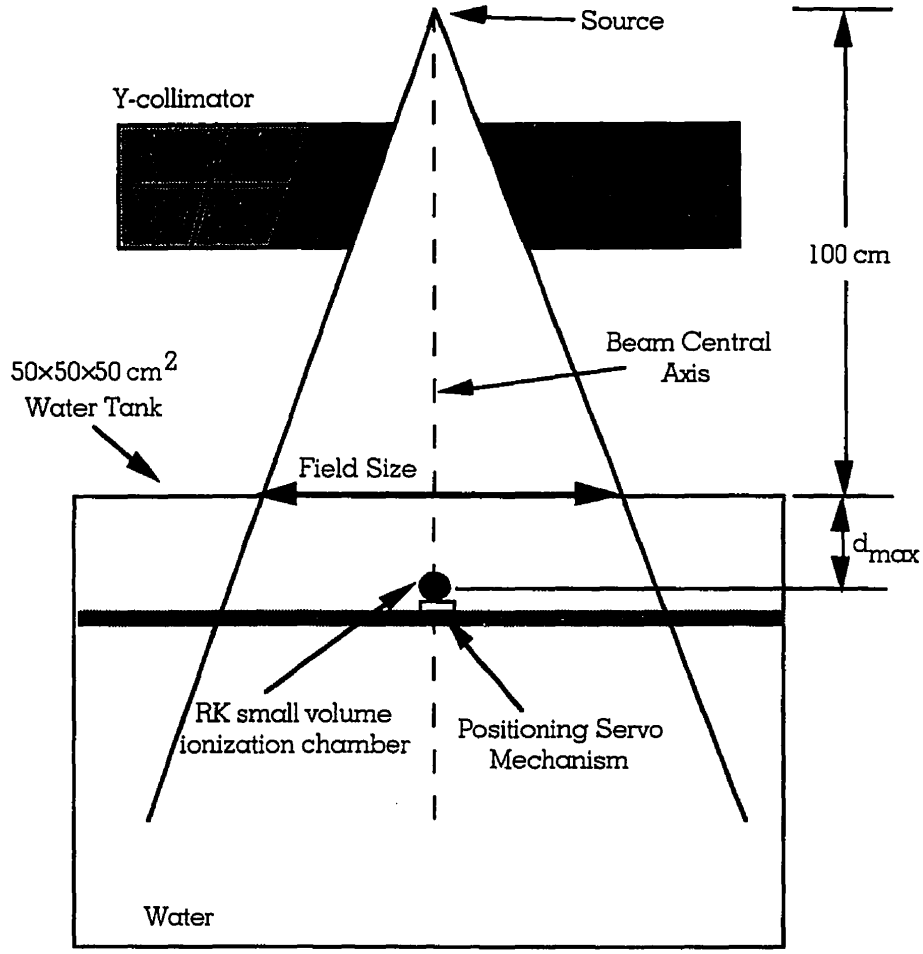

FIGURE 6.4. Schematic illustration of the geometry used to measure the percentage depth dose (PDD) data of the dynamic wedge. All measurements were performed with a small volume RK ionization chamber in an RFA water tank (Scanditronix, Upsalla, Sweden). The RK ionization chamber was positioned along the central axis of the beam using the positioning servo mechanism. Each ionization signal was normalized to the signal measured at the depth of maximum dose d_{max} to give a set of PDD values. SSD: 100 cm.

6.3 Dynamic wedge: linearity with prescribed dose

Measurements were taken to verify that each nominal dynamic wedge (15°, 30°, 45°, and 60°) operates linearly with the prescribed dose for both 6 MV and 18 MV photon beam energies and a treatment field size of 20x20 cm^2. This was accomplished by collecting data in Solid Water at the depth of maximum dose d_{max} with a Gammex TM-3m therapy beam monitor (discussed in Section 5.4) and a Gammex 5-channel electrometer. Ioniza-

tion chambers 1 and 2 were placed underneath the "thin" end and "thick" end of the wedge, respectively, and the resulting integrated signals were normalized to 100 for the integrated reference detector reading placed in the center of the dynamic wedge field. The geometry of the experiment is shown in Fig. 6.11. A series of known doses was delivered to d_{max} while the dose rate was held constant at 200 MU/min. This allowed for the calculation of relative signal readings under the thin and thick end of the dynamic wedge as a function of the prescribed dose.

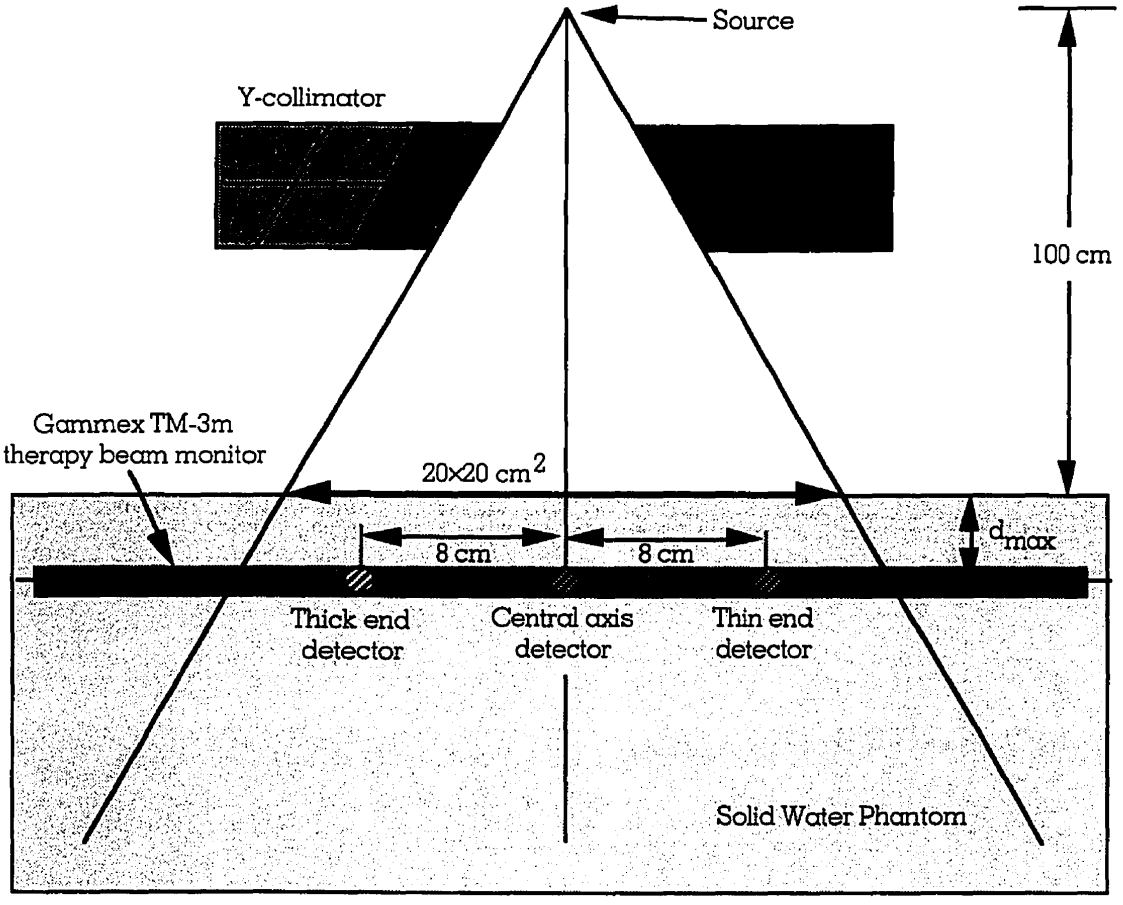

FIGURE 6.11. ***Schematic illustration of the geometry used to measure the linearity of the dynamic wedge with respect to the prescribed dose and dose rate with a Gammex TM-3m therapy beam monitor placed a depth of maximum dose d_{max} in Solid Water. Integrated signals were recorded under the thin and thick side of the dynamic wedge and normalized to the integrated reference detector reading placed at the center of dynamic wedge field at d_{max}. Field size: 20×20 cm^2, SSD: 100 cm.***

The results of the linearity tests are presented in Figures 6.12 and 6.13 for the four nominal dynamic wedges for 6 MV and 18 MV photons, respectively. The thin side measurements, designated by solid lines in each of the figures, correspond to the integrated detector signal in the region of the dynamic treatment field that is exposed to the radiation beam for a longer duration relative to the central axis and thick side detectors. Since the thin side detector is in the radiation field for a longer period of time, as compared to the central axis detector, it always measures a higher dose relative to that measured on the central axis. Conversely, the thick end detector is exposed to the dynamic radiation field for a shorter time than the central axis detector, and this results in a lower dose relative to that on the central axis.

The data of Figures 6.12 and 6.13 (pages 98 and 99) reveals that the relative dose under the thin end and thick end of the dynamic wedge remains the same regardless of the prescribed dose to the central axis. This demonstrates that all nominal dynamic wedges investigated operate linearly with prescribed dose over the prescribed dose range from 20 cGy to 400 cGy.

6.4 Dynamic wedge: linearity with dose rate

Measurements were taken to verify that every nominal dynamic wedge (15°, 30°, 45°, and 60°) operates linearly with the dose rate for both 6 MV and 18 MV energies and a field size of 20×20 cm^2. This was accomplished by collecting data in the Solid Water phantom at depth of maximum dose d_{max} with a Gammex TM-3m therapy beam monitor (described section 5.4) and a Gammex 5-channel electrometer, as shown in Fig. 6.11. Ionization chambers 1 and 2 were placed under the "thin" end and "thick" end of the wedge, respectively, and the resulting integrated signals were normalized to 100 for the integrated reference detector reading placed in the center of the dynamic wedge field. The dose rate was varied while the prescribed dose was held constant at 200 MU. This permitted the calculation of relative signal readings under the thin and thick end of the dynamic wedge as a function of the dose rate.

The results of the experiments are shown in Figures 6.14 and 6.15 (pages 100 and 101) for the four nominal dynamic wedge angles for 6 MV and 18 MV photon, respectively. The data shows that the same relative dose is delivered under the thin and thick end of the dynamic wedge for any selected dose rate in the range from 100 MU/min to 600 MU/min. We conclude that all four dynamic wedges operate linearly over the entire range of dose rates available on our linear accelerator.

6.5 Dynamic wedge profiles

The Clinac 2300 dynamic wedge profiles were measured using film densitometry techniques. Kodak X-Omat V radiotherapy film was sandwiched between slabs of Solid Water and exposed to the photon beam in a plane-parallel geometry, as shown in Fig. 6.16. After exposure and development each film was scanned perpendicularly to the beam central axis using an RFA-300 film densitometer to produce a set of beam profiles. For the photon beam with energy of 6 MV, beam profiles were measured at depths of 1.5 cm, 6.5 cm, 11.5 cm, 16.5 cm, and 26.5 cm. Beam profiles for 18 MV photons were measured at depths of 3.0 cm, 8.0 cm, 13 cm, 18 cm, and 28 cm.

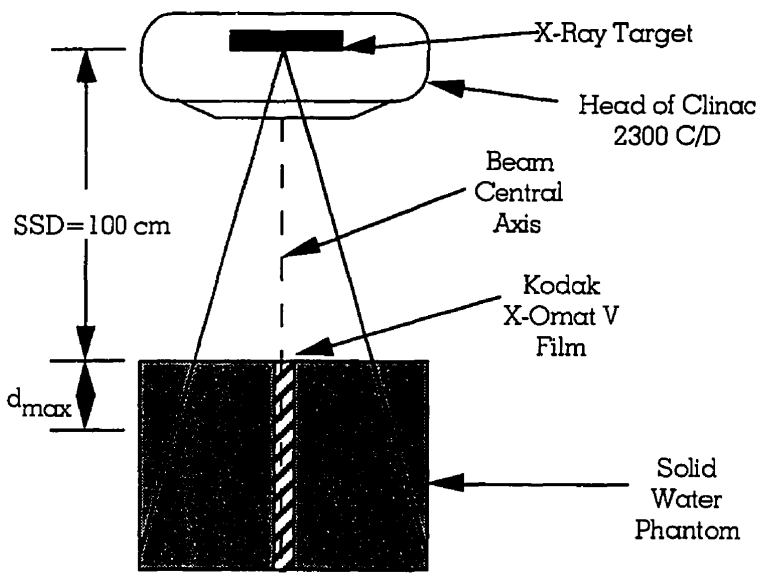

FIGURE 6.16. ***The plane-parallel film geometry used to measure the dynamic wedge beam profiles.***

The measured dynamic wedge beam profiles are shown in Figures 6.17 through 6.22 (pages 102 through 107) for the four available wedge angles and 6 MV and 18 MV photons, respectively, with field sizes of 4×4 cm^2, 10×10 cm^2, and 20×20 cm^2. Ion chamber measurements are shown for comparison on the 10×10 cm^2 dynamically wedged fields for both energies and all wedge angles to confirm the accuracy of our film dosimetry. Difficulties were encountered with film densitometry in the penumbra region, possibly due to film artifacts as a result of non-ideal film processor conditions.

A series of films was also used to measure the beam profiles in the non-wedged direction for a 45° dynamically wedged field and a 45° wedge filter. Each film was placed in perpendicular geometry (see Fig. 5.6) at depth of maximum dose d_{max} in Solid Water. The exposed films were scanned perpendicularly to the wedge-gradient axis and then compared to an open field. The maximum dynamic field size of 20×20 cm^2 for a 6 MV photon beam was investigated, since it demonstrates pronounced effects at the treatment fields edges.

The beam profiles in the non-wedged direction produced from an open field, dynamic wedge, and physical wedge filter are presented in Fig. 6.23 (page 108). The dynamic wedge closely approximates the open field dose profile; however, the physical wedge filter demonstrates a decrease in dose at the field edges due to increasing beam hardening effects.

6.6 Measurement of surface dose and dose in the build-up region for the dynamic wedge

The absorbed dose measurements in the buildup region for the Clinac 2300 dynamic wedge were performed with the Attix Plane-Parallel Chamber, Model 449 (described in Section 5.3.3). While maintaining a constant *SSD* of 100 cm, sheets of Solid Water were placed in front of the ionization chamber to measure the absorbed dose as a function of depth. A sufficient thickness Solid Water was placed behind the detector to ensure full backscatter conditions. Additionally, the lateral dimensions of the Solid Water sheets were large enough to provide lateral electronic equilibrium at all measurement depths. The surface dose was measured as a relative ionization signal produced with no phantom material on top of the chamber to the signal with d_{max} of material on top of the chamber for a 10×10 cm^2 field size and all dynamic wedge angles for both 6 MV and 18 MV photon energies. These measurements were performed for both positive and negative polarity, which were averaged to yield the actual ionization current, as shown in Eq. (5.3). The geometry of this experiment is presented in Fig. 6.24.

The measured relative surface doses, normalized to values obtained at the depth of maximum dose d_{max} are presented in Table 6.3 for a 10×10 cm^2 open field and four dynamic and physical wedge angles. The results show that the surface dose for the dynamic wedges is very close to that of the open field. There is a slight increase in surface dose for the 60° dynamic wedge for the field size measured.

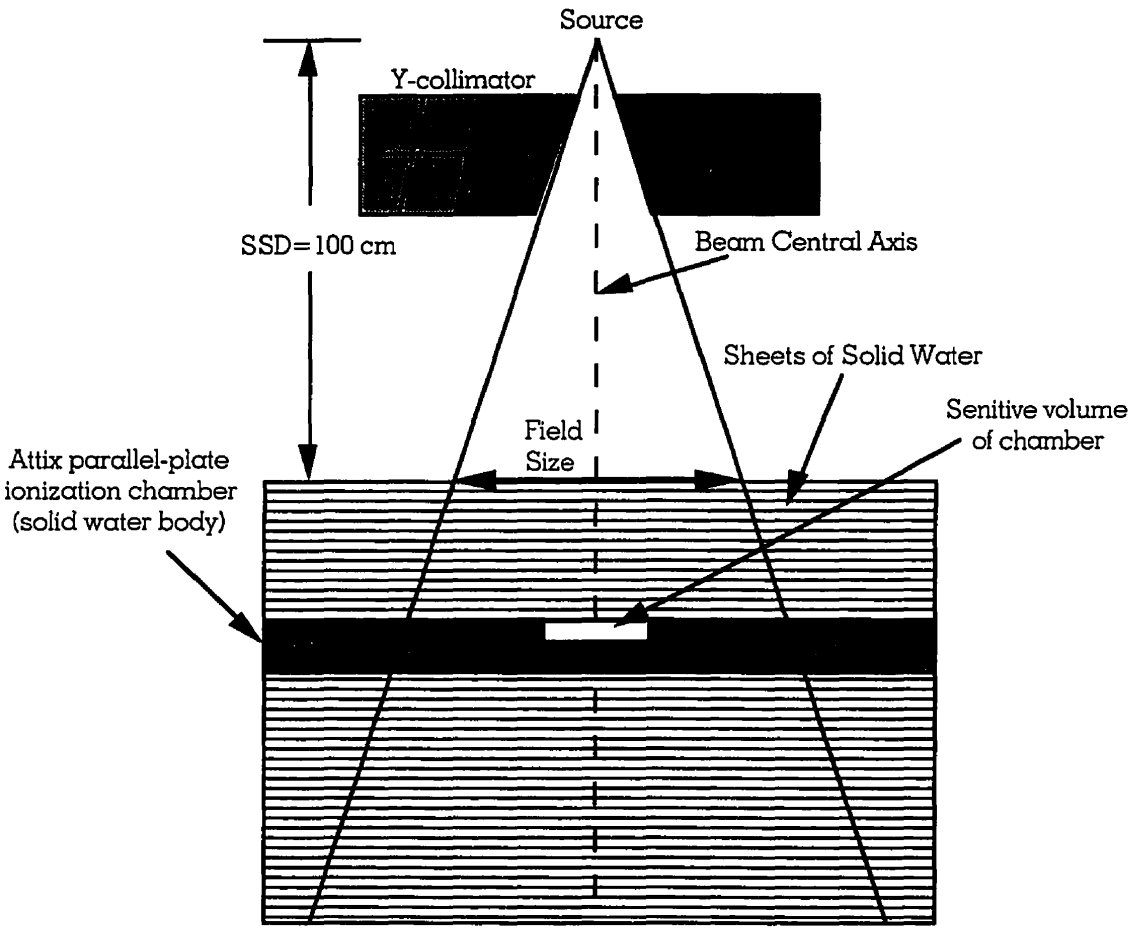

FIGURE 6.24. ***Schematic illustration of the geometry used to measure the surface dose and build-up region data of the dynamic wedges. All measurements were performed with an Attix parallel-plate ionization chamber. Sheets of Solid Water phantom were place one by on top of the ionization chamber to increase the depth within the phantom. The SSd was set to 100 cm for every measurement. This process was repeated for both the positive and negative polarity, and the average of these two values yields the actual current as shown in Eq. (5.3).***

TABLE 6.3. *Comparison of the measured surface dose for open, dynamic wedge, and static wedge fields for 6 MV and 18 MV photon beams. Field size: 10x10 cm^2.*

	6 MV Photons	18 MV Photons
Open Field	15.8%	14.4%
Dynamic 15°	15.8%	14.5%
Dynamic 30°	15.8%	14.4%
Dynamic 45°	15.9%	14.5%
Dynamic 60°	16.3%	14.8%
Physical 15°	13.8%	11.1%
Physical 30°	13.3%	11.2%
Physical 45°	12.8%	11.5%
Physical 60°	12.9%	12.0%

Table 6.3 also shows that the measured surface dose for the physical wedge filter is lower than that obtained for the open and dynamically wedge fields. This occurs for two reasons. First, due to beam hardening effects caused by the wedge filter there will be attenuation of low energy photons which would have deposited energy at the surface. Second, the wedge filter also removes low energy electrons caused by collimator scatter which would also add to the dose at the surface.

As far as the dose in the build-up region is concerned, the dynamic wedge is almost identical to the open field. All measured points were within ±2% of the open field values. Figures 6.25 and 6.26 (pages 109 and 110) present the measured build-up regions for the dynamic wedge and physical wedge fields for 6 MV and 18 MV photons, respectively, and a 10×10 cm^2 field. The dynamic wedge delivers a higher dose, relative to the physical wedge filter, in the build-up region.

6.7 Treatment time

The total time required to complete a single beam dynamic wedge treatment is equal to the addition of times needed to successfully complete each segment in the corresponding STT. The time necessary to complete each of these segments is strongly influenced by the dose rate and collimator velocity. Figures 6.27 and 6.28 (page 111) show a comparison of the

single radiation beam treatment time curves for a 10×10 cm^2 45° dynamic wedge and a conventional physical wedge for 6 MV and 18 MV photon beams, respectively.

At high prescription doses the segments become dose rate limited. This occurs since the operator cannot choose the delivery dose rate. In the dynamic wedge mode the default dose rate is 300 MU/min and cannot be surpassed. Because of this dose rate limit, the dynamic wedge treatment time approaches an asymptote line that is projected from the origin. At lower prescription doses the segments are collimator velocity limited. For this reason there will be a noticeable difference between the asymptote line and the dynamic wedge treatment time curve at low given doses. The absolute minimum treatment time is equal to the time it takes the collimator to completely cross the chosen field width. Since the maximum collimator velocity is 1 cm/s, the minimum treatment time for a 10×10 cm^2 field is 10 seconds (0.17 min), as shown in Figures 6.27 and 6.28.

It is important to note that the slope of the asymptote line in inversely proportional to the dose rate. Therefore, since the dose rate is proportional to the wedge factor, the slope is inversely proportional to the wedge factor. Thus, the ratio of slopes of the dynamic wedge asymptote line with respect to the line representing the physical wedge filter is approximately equal to the inverse ratio of the dynamic wedge factor and the physical wedge factor, as seen in Eq. (6.1).

$$\frac{DWS}{PWS} = \left(\frac{EWF}{WF}\right)^{-1} \quad , \tag{6.1}$$

where DWS is the dynamic wedge asymptote slope, PWS is the slope of the wedge filter line, EWF is the effective dynamic wedge factor, and WF is the physical wedge factor. Since the dynamic wedge does not suffer the beam hardening effects of the physical wedge, the dynamic wedge factors will be closer to unity than conventional wedges. This implies that the dynamic wedge will deliver the dose more efficiently to the patient and the ratio of wedge factors will become large. Therefore, at clinically useful doses (about 1 Gy to 2 Gy) the single beam dynamic wedge treatment time is lower than the time for the conventional wedge filter.

6.8 Summary

The four nominal dynamic wedges investigated were found to operate linearly with prescribed dose and dose rate. This ensures that a change in the prescribed dose or dose rate

parameters in subsequent dynamic wedge treatments, the same dose, relative to the central axis, will be delivered to all points in each radiation field.

The dynamic wedge factors strongly depend on field size, increasing as field size decreases. This implies that simple interpolation calculations of a square field wedge factor table in order to find the number of monitor units necessary to deliver the prescribed dose cannot be used. The X-collimator setting does not influence the dynamic wedge factors. Thus, the effective wedge factor depends only on the dynamic wedge field width and not on the equivalent square of the field.

The central axis percentage depth dose for the dynamic wedge closely approximates measured open field data. All measured dynamic wedge data is within ±2% of open field measurements, making treatment planning easier. This is a significant contrast to the *PDD*s of physical wedge filters which can differ from open field data by as much as ±5% because of beam hardening effects.

Beam profiles were measured in Solid Water using film densitometry, supported by ionization chamber measurements, for all available dynamic wedge angles and 6 MV and 18 MV photon beam energies with field sizes of 4×4 cm^2, 10×10 cm^2, and 20×20 cm^2. Profiles in the non-wedged direction were also measured and compared for open, dynamic wedge, and physical wedge fields. The dynamic wedge closely approximates the open field dose profile, but delivers a higher dose than the physical wedge filter at the field edges.

The surface dose for all available dynamic wedge angles is very close to that of the open field. A slight increase in surface dose was noticed for the 60^o dynamic wedge for the field size measured. In the build-up region the surface dose for the dynamic wedge is generally within ±2% to that measured for the open field.

The time needed to deliver a single beam dynamic wedge treatment was found to be less than the treatment time of a physical wedge treatment for the delivery of clinically useful doses. This implies that a single dynamically wedged radiation beam delivers dose more efficiently than conventional physical wedge filter techniques.

6.9 References

1. Private communication with Calvin Huntzinger, Varian Oncology Systems, Varian Associates, Inc., Palo Alto, California.

2. F. G. Abrath, J. A. Purdy: *Wedge design and dosimetry for 25 MV x rays*, Radiol. **136**, 757-762 (1980).

3. A. Wu, R. D. Zwicker, F. Krasin, E. S. Sternick: *Dosimetry characteristics of large wedges for 4 and 6 MV x rays*, Med. Phys. **11**, 186-188 (1984).

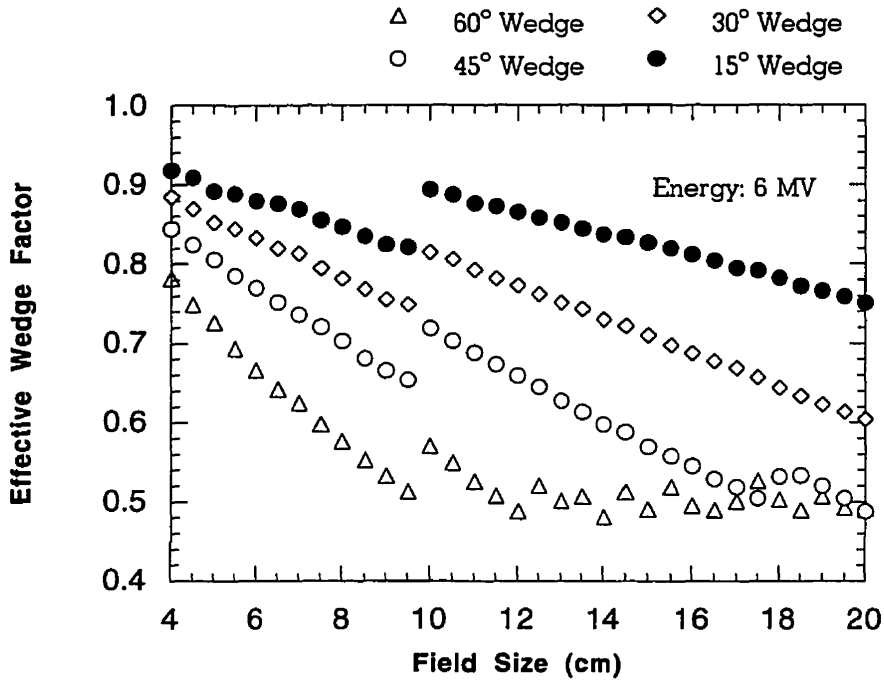

FIGURE 6.2. ***The effective wedge factor (EWF) as a function of field size and wedge angle for a 6 MV photon beam. All measurements were taken in Solid Water at a depth of 10 cm.***

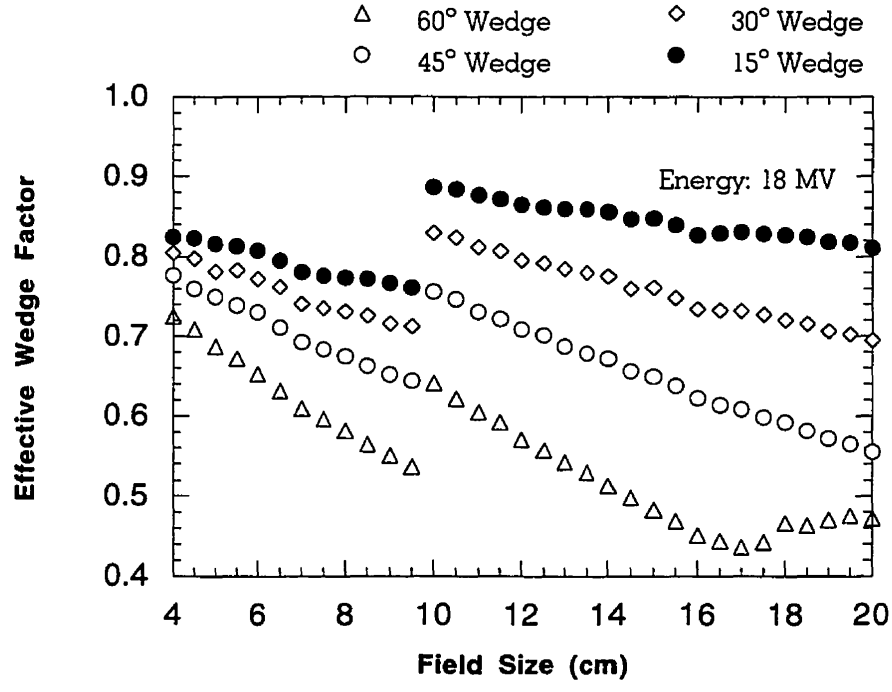

FIGURE 6.3. ***The effective wedge factor (EWF) as a function of field size and wedge angle for an 18 MV photon beam. All measurements were taken in Solid Water at a depth of 10 cm.***

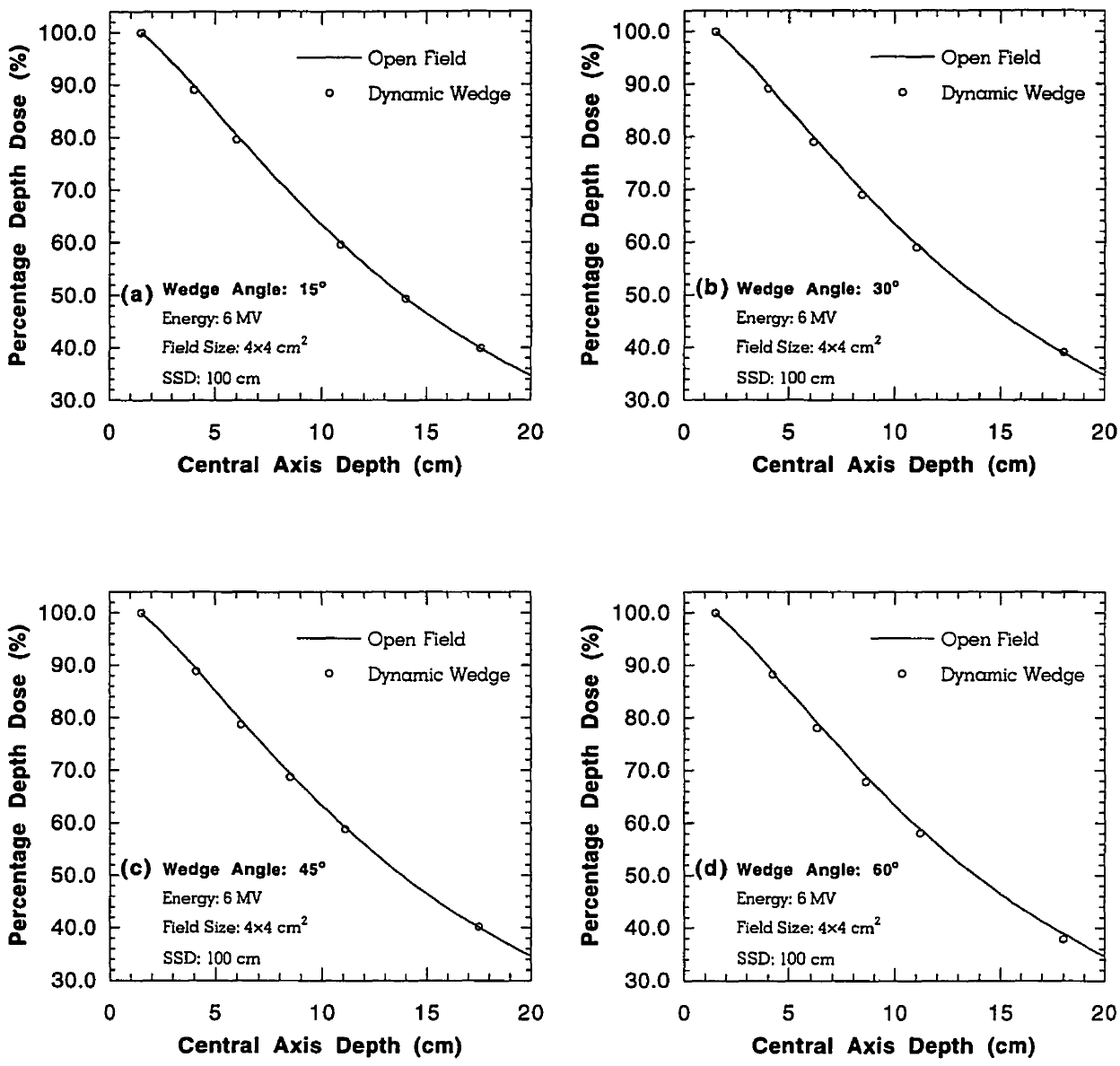

FIGURE 6.5. *The percentage depth dose (PDD) at various depths in water for the (a) 15° dynamic wedge, (b) 30° dynamic wedge, (c) 45° dynamic wedge, and (d) 60° dynamic wedge as compared to open field data for a 6 MV photon beam with a 4×4 cm² field size. SSD: 100 cm.*

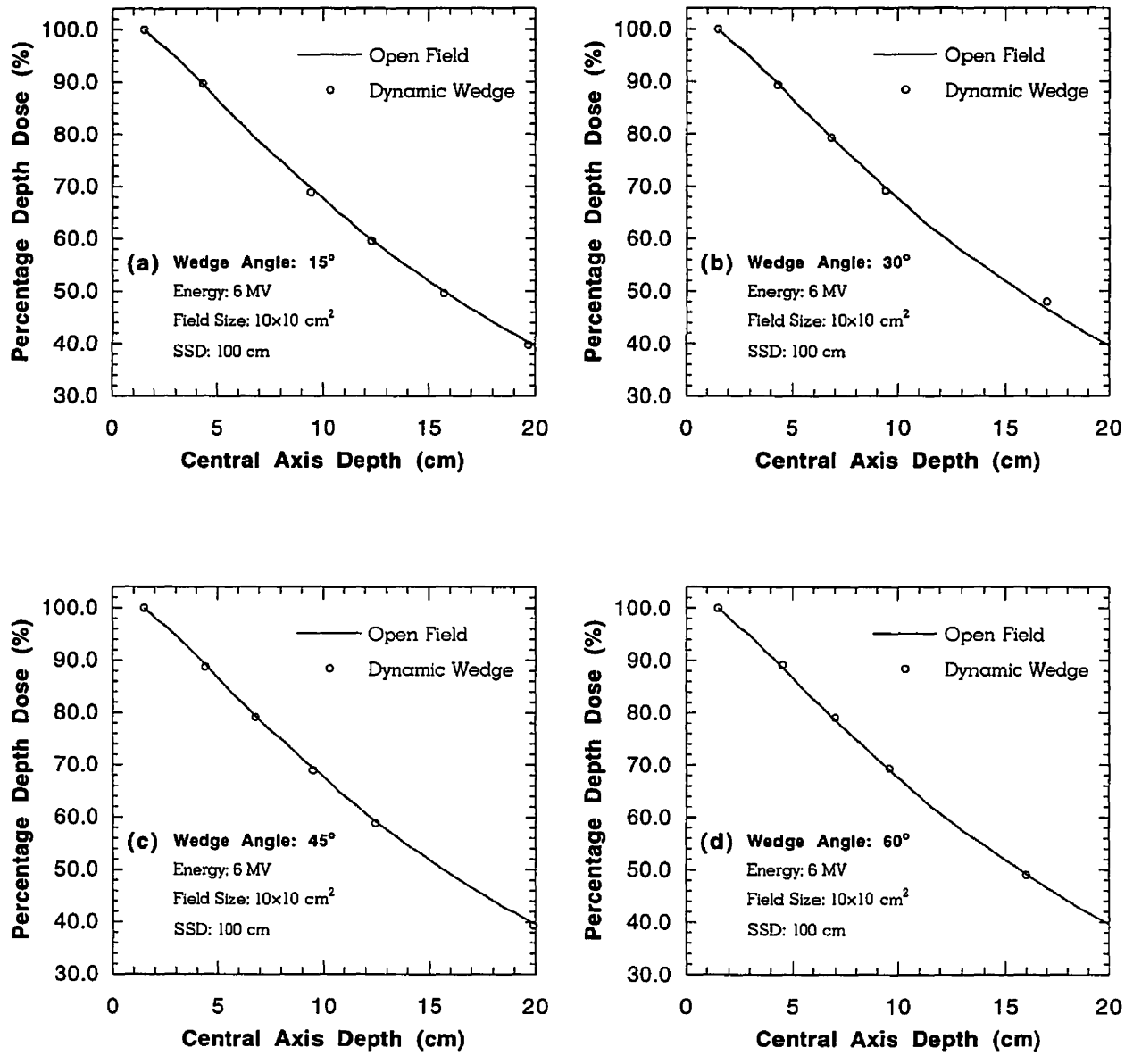

FIGURE 6.6. *The percentage depth dose (PDD) at various depths in water for the (a) 15° dynamic wedge, (b) 30° dynamic wedge, (c) 45° dynamic wedge, and (d) 60° dynamic wedge as compared to open field data for a 6 MV photon beam with a 10×10cm² field size. SSD: 100 cm.*

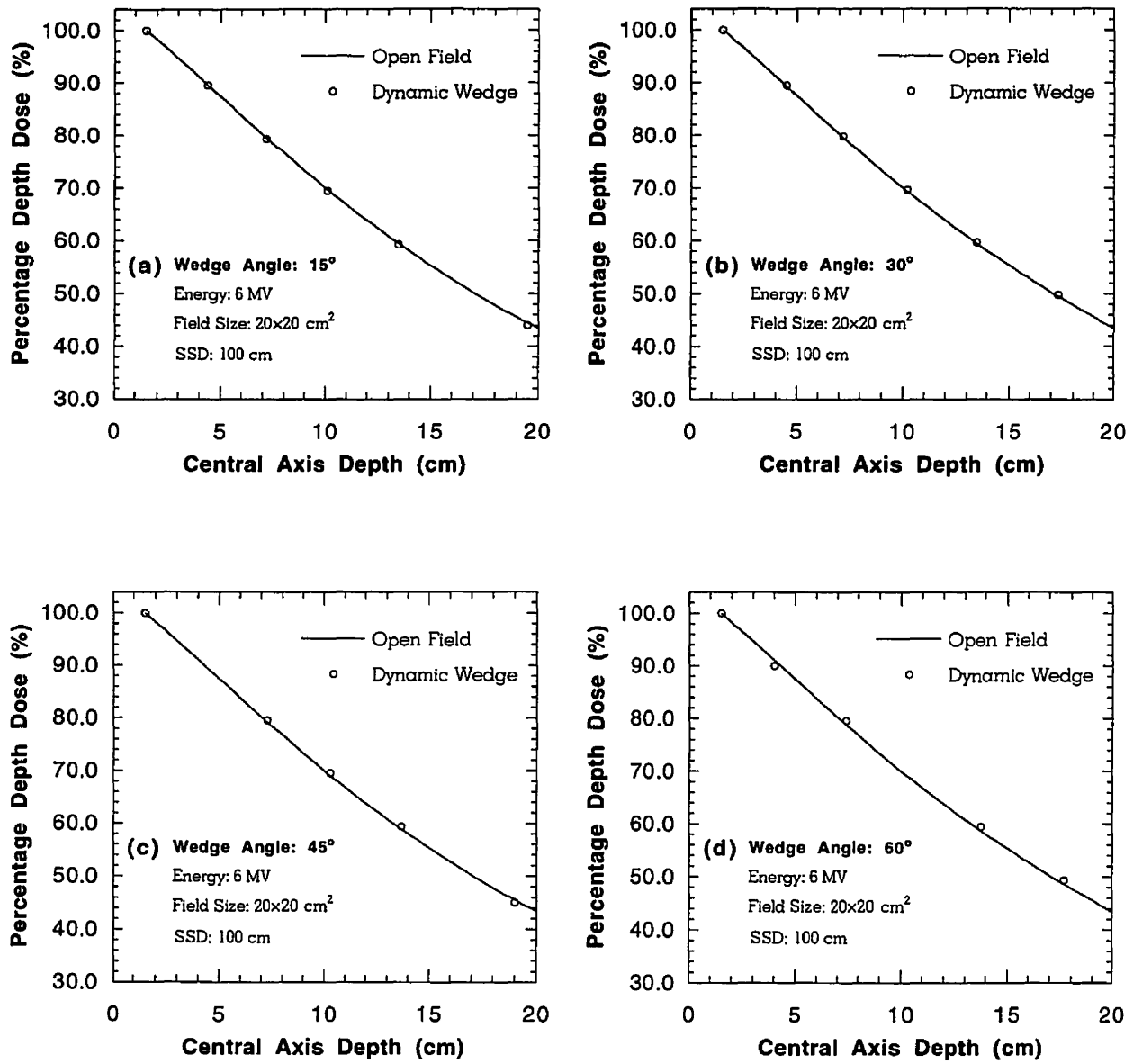

FIGURE 6.7. *The percentage depth dose (PDD) at various depths in water for the (a) 15° dynamic wedge, (b) 30° dynamic wedge, (c) 45° dynamic wedge, and (d) 60° dynamic wedge as compared to open field data for a 6 MV photon beam with a 20×20 cm² field size. SSD: 100 cm.*

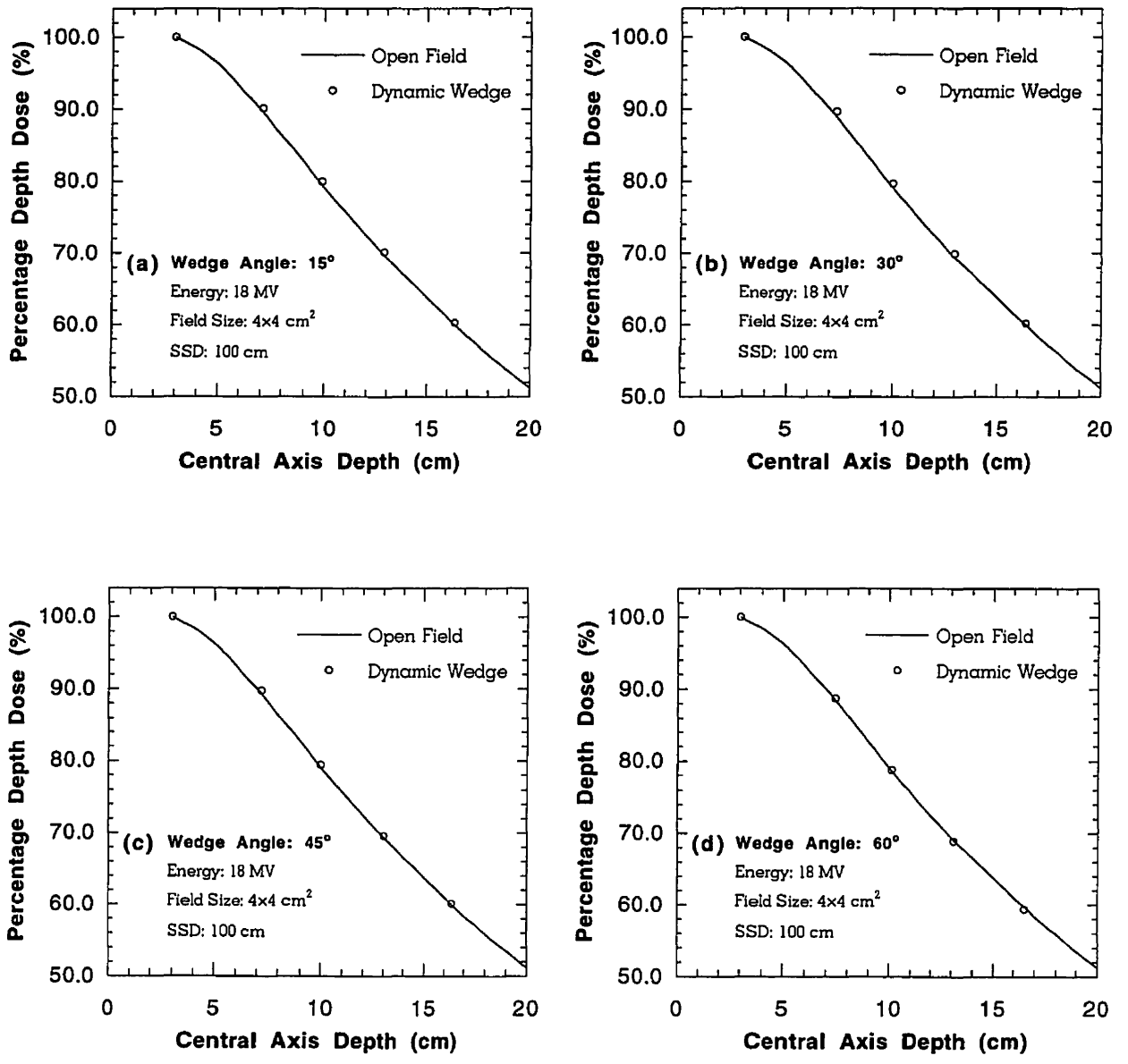

FIGURE 6.8. *The percentage depth dose (PDD) at various depths in water for the (a) 15° dynamic wedge, (b) 30° dynamic wedge, (c) 45° dynamic wedge, and (d) 60° dynamic wedge as compared to open field data for a 18 MV photon beam with a 4×4 cm² field size. SSD: 100 cm.*

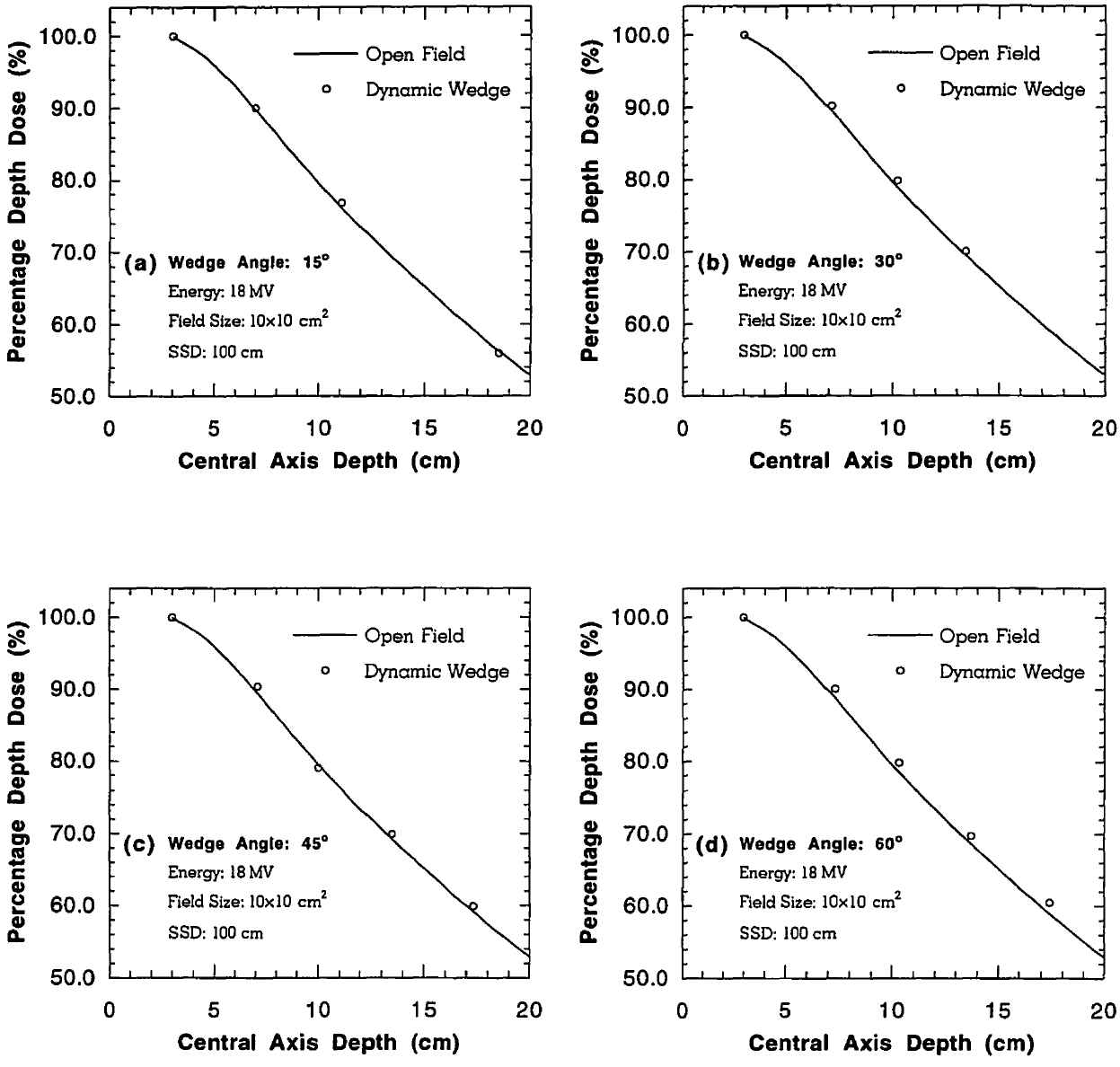

FIGURE 6.9. *The percentage depth dose (PDD) at various depths in water for the (a) 15° dynamic wedge, (b) 30° dynamic wedge, (c) 45° dynamic wedge, and (d) 60° dynamic wedge as compared to open field data for a 18 MV photon beam with a 10×10 cm² field size. SSD: 100 cm.*

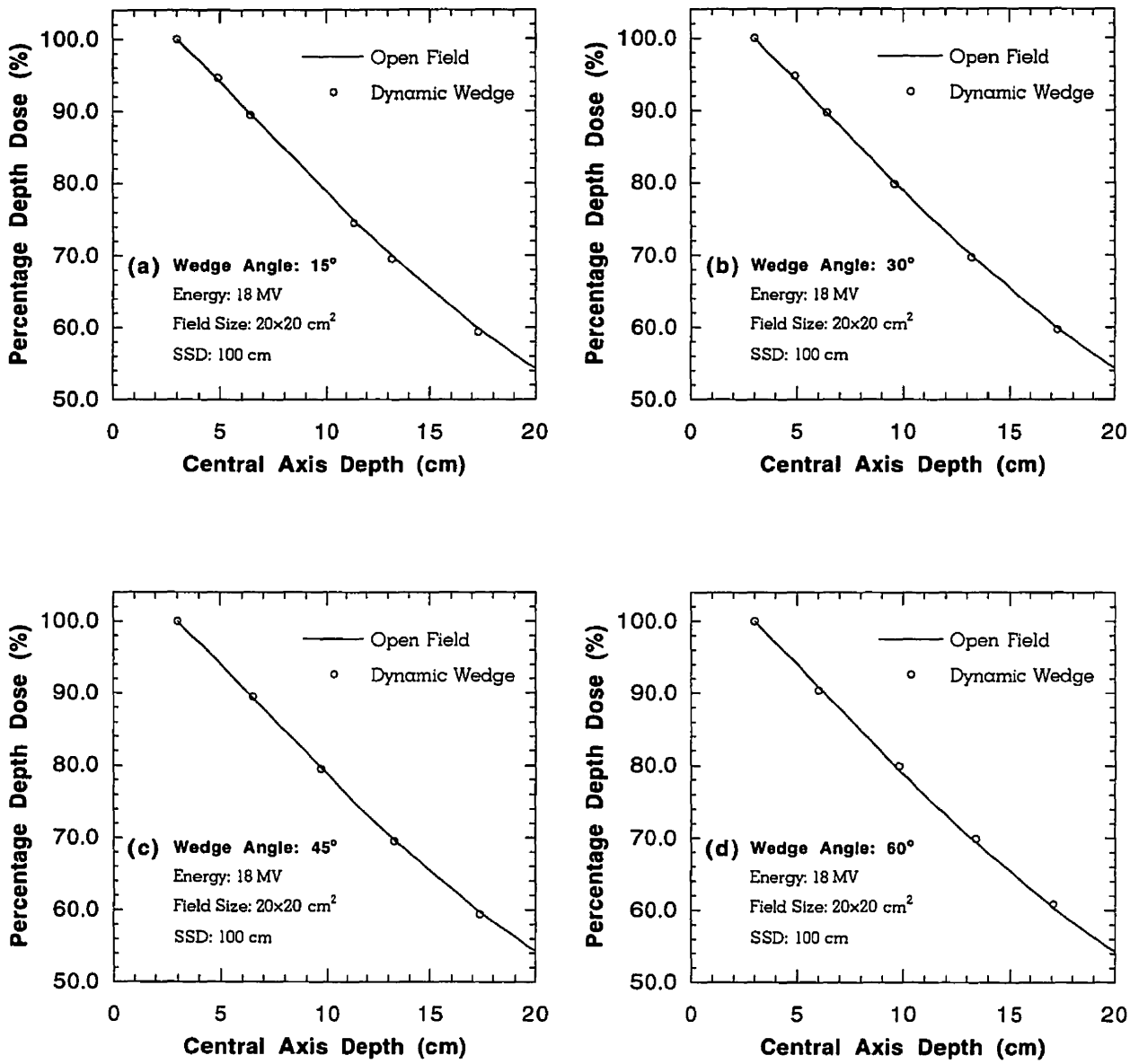

FIGURE 6.10. *The percentage depth dose (PDD) at various depths in water for the (a) 15° dynamic wedge, (b) 30° dynamic wedge, (c) 45° dynamic wedge, and (d) 60° dynamic wedge as compared to open field data for a 18 MV photon beam with a 20×20 cm² field size. SSD: 100 cm.*

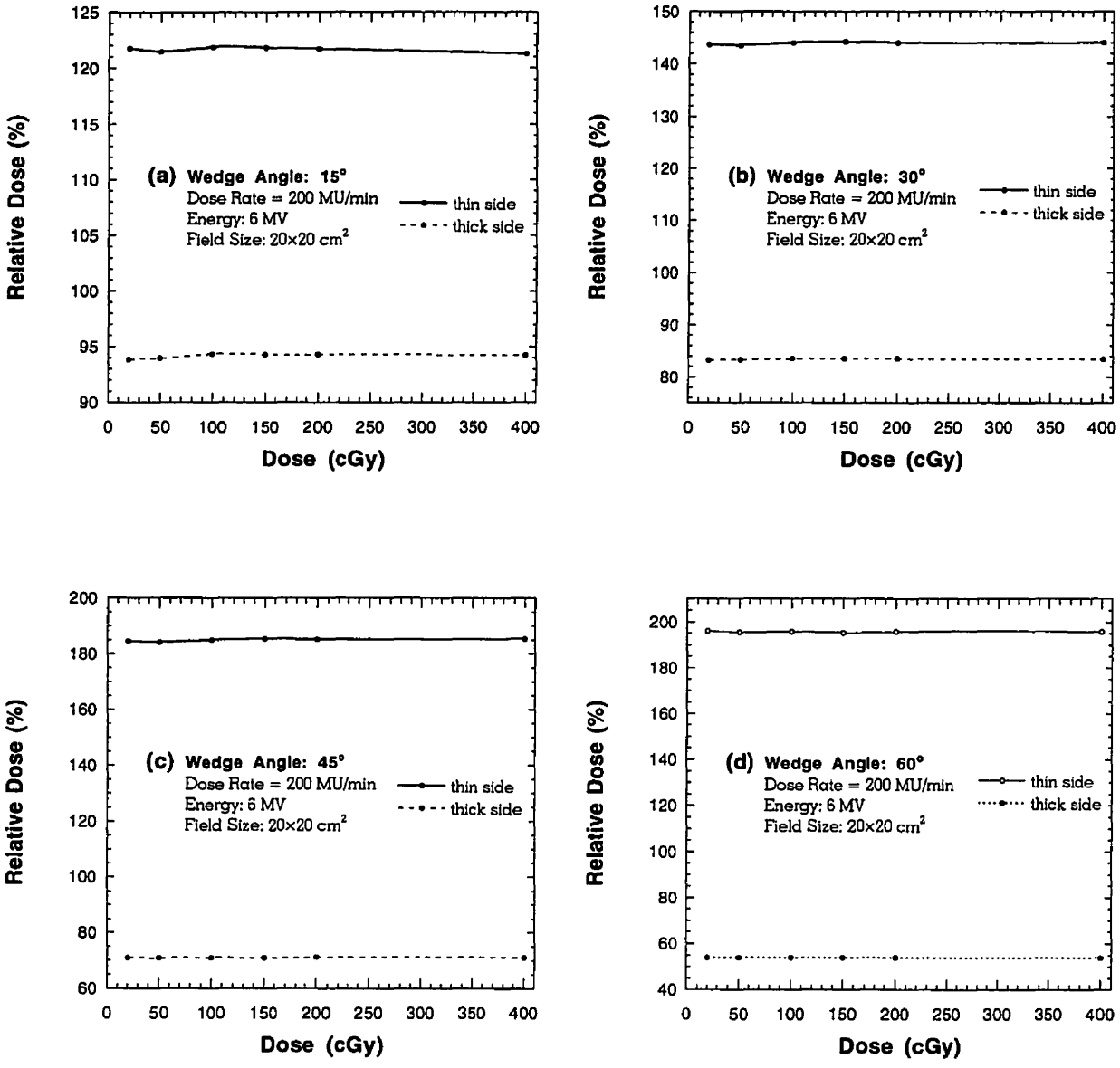

FIGURE 6.12. ***Linearity of the dynamic wedge with dose in the 6 MV photon mode for the (a) 15° dynamic wedge (b) 30° dynamic wedge (c) 45° dynamic wedge, and (d) 60° dynamic wedge. The dose rate was held constant at 200 MU/min while the prescribed dose was varied. The field size was kept at 20×20 cm² and all measurements were performed in Solid Water at depth d_{max}. The data is normalized to 100 at d_{max} on the central axis. SSD: 100 cm.***

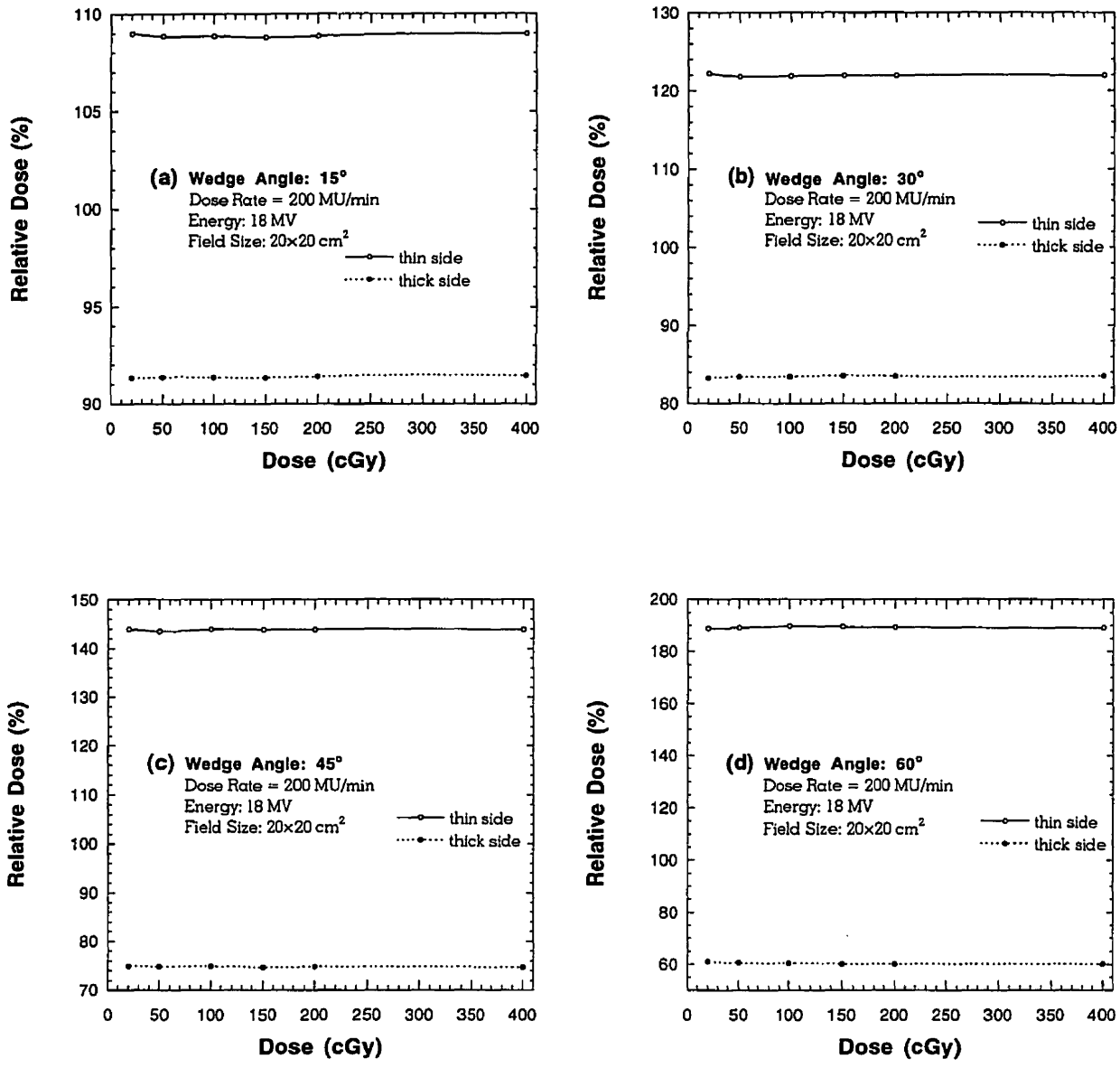

FIGURE 6.13. ***Linearity of the dynamic wedge with dose in the 18 MV photon mode for the (a) 15° dynamic wedge (b) 30° dynamic wedge (c) 45° dynamic wedge, and (d) 60° dynamic wedge. The dose rate was held constant at 200 MU/min while the prescribed dose was varied. The field size was kept at 20×20 cm² and all measurements were performed in Solid Water at depth d_{max}. The data is normalized to 100 at d_{max} on the central axis. SSD: 100 cm.***

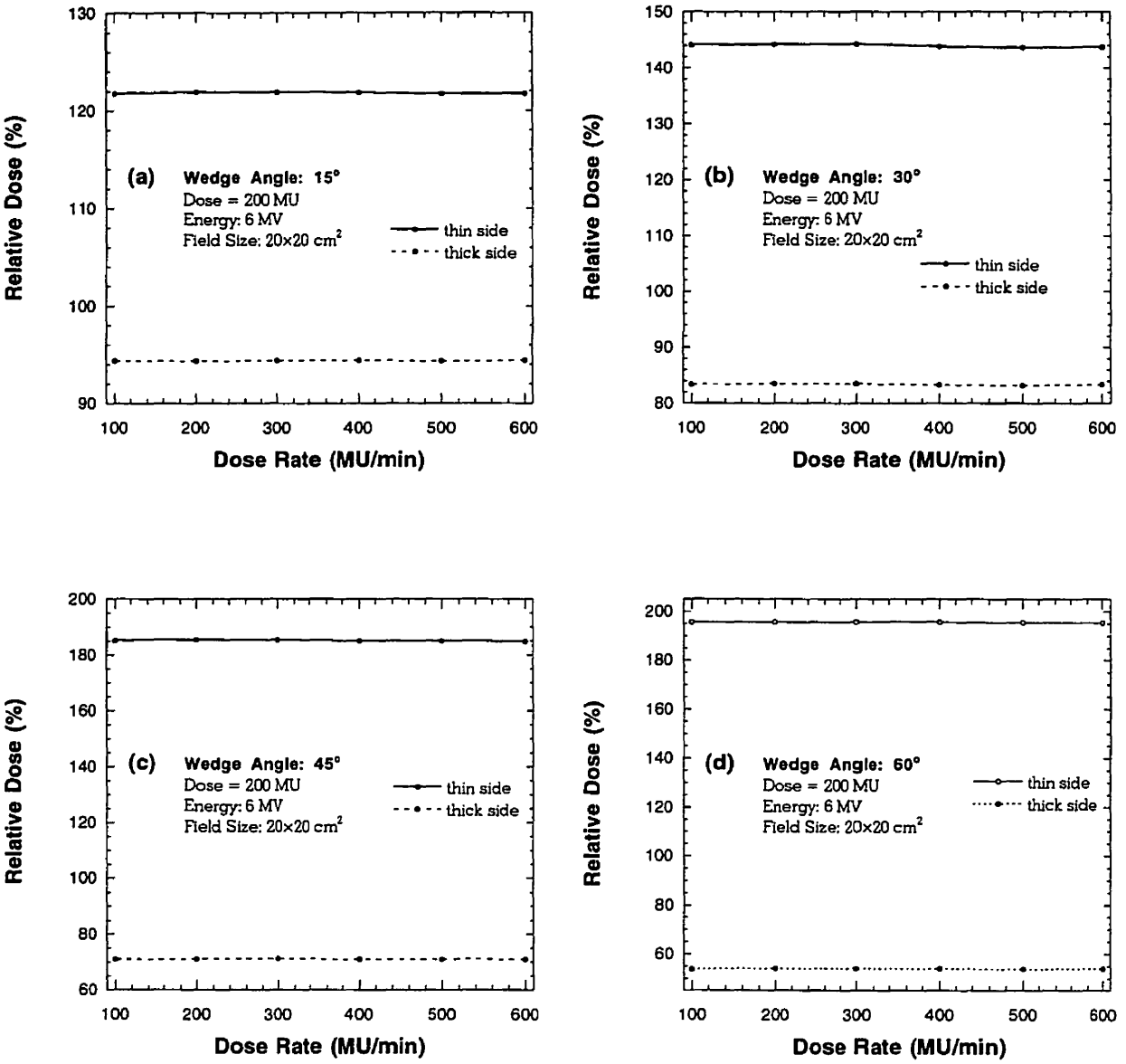

FIGURE 6.14. *Linearity of the dynamic wedge with dose rate in the 6 MV photon mode for the (a) 15° dynamic wedge (b) 30° dynamic wedge (c) 45° dynamic wedge, and (d) 60° dynamic wedge. The prescribed dose was held constant at 200 MU while the dose rate was varied. The field size was kept at 20×20 cm² and all measurements were performed in Solid Water at depth d_{max}. The data is normalized to 100 at d_{max} on the central axis. SSD: 100 cm.*

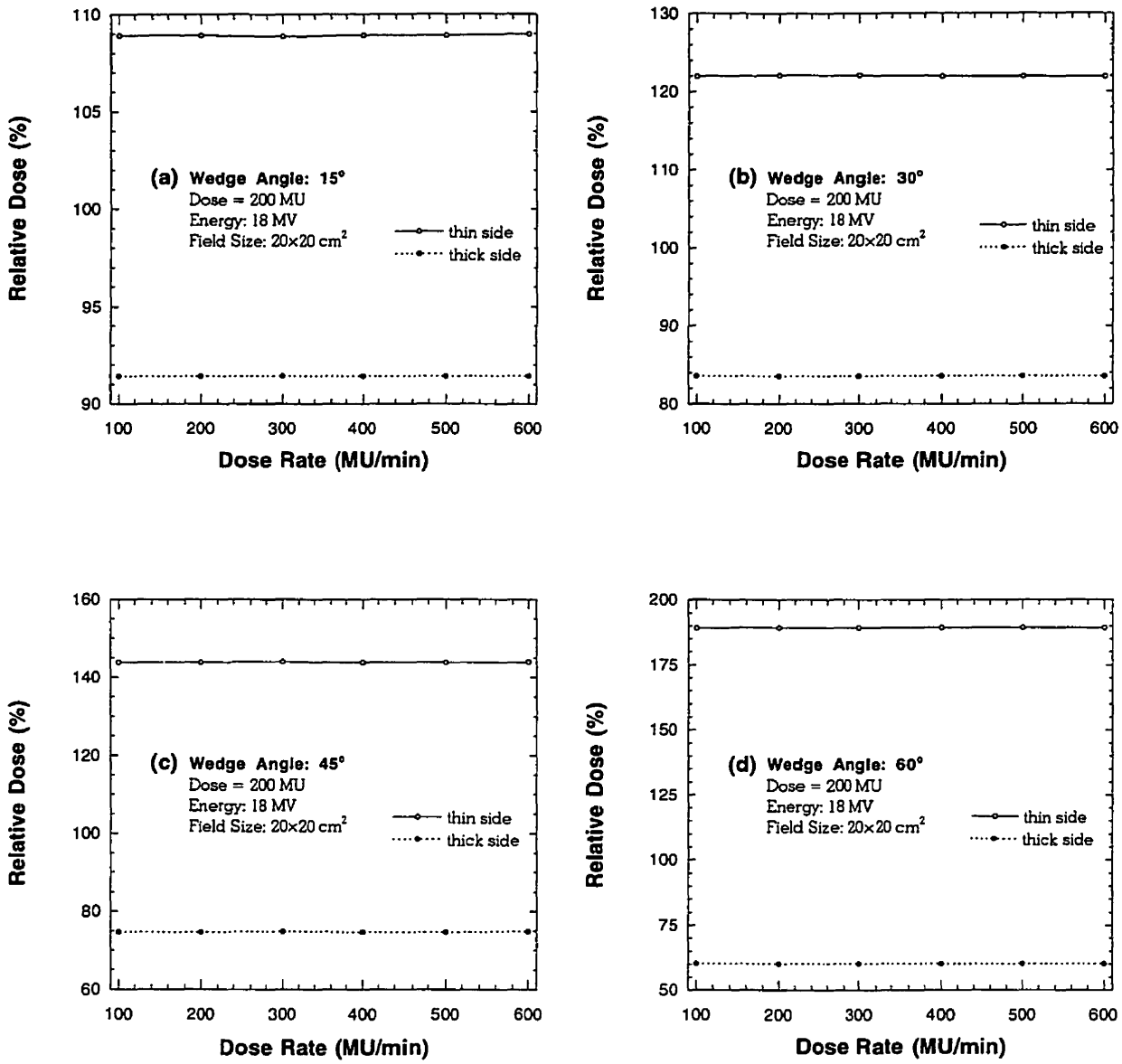

FIGURE 6.15. *Linearity of the dynamic wedge with dose rate in the 18 MV photon mode for the (a) 15° dynamic wedge (b) 30° dynamic wedge (c) 45° dynamic wedge, and (d) 60° dynamic wedge. The prescribed dose was held constant at 200 MU while the dose rate was varied. The field size was kept at 20×20 cm² and all measurements were performed in Solid Water at depth d_{max}. The data is normalized to 100 at d_{max} on the central axis. SSD: 100 cm.*

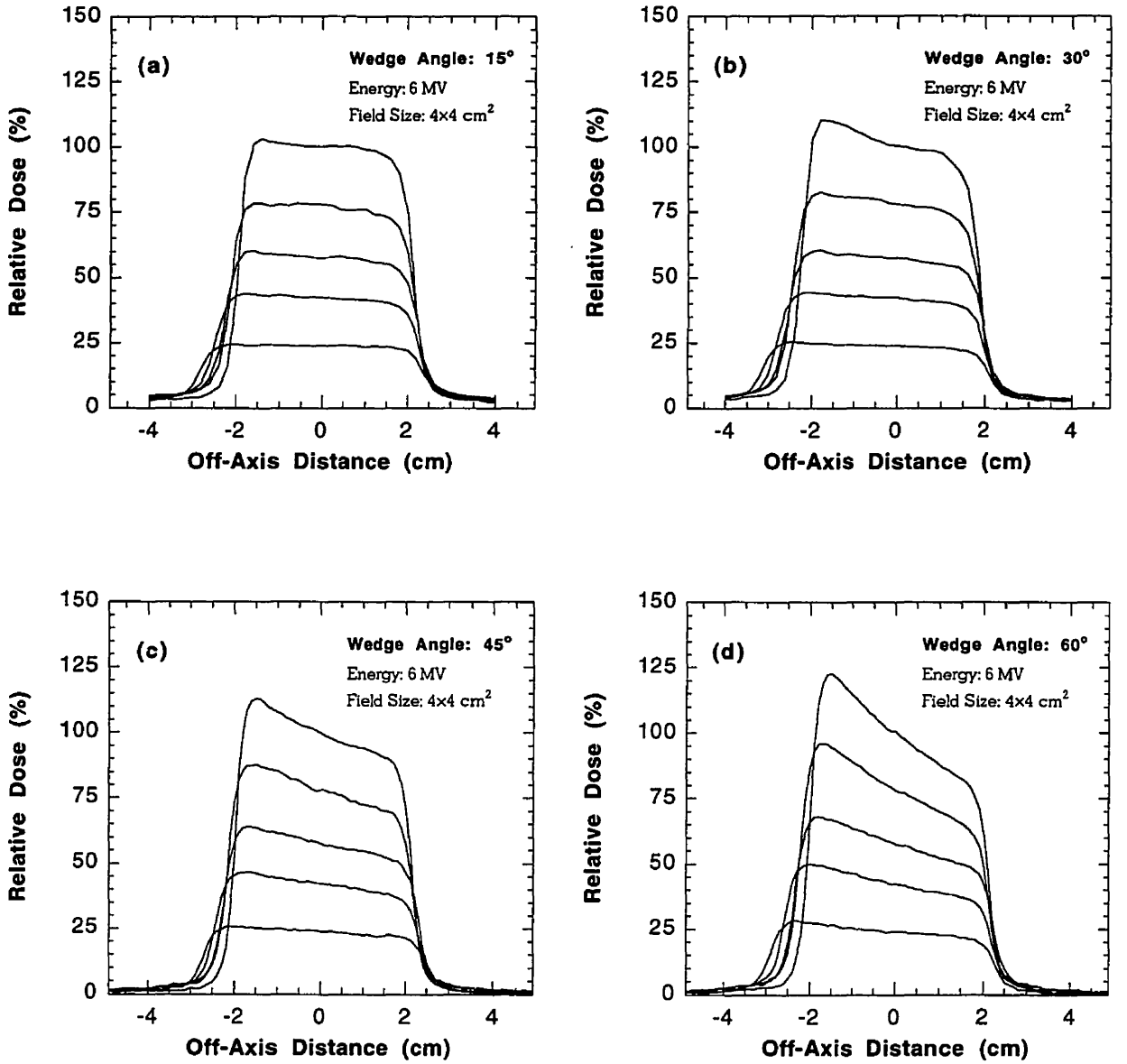

FIGURE 6.17. *Dynamic wedge profiles for the (a) 15° dynamic wedge, (b) 30° dynamic wedge, (c) 45° dynamic wedge, and (d) 60° dynamic wedge at depths of d_{max}=1.5 cm, 6.5 cm, 11.5 cm, 16.5 cm, and 26.5 cm for a 6 MV photon beam with a field size of 4×4 cm². SSD: 100 cm. Data are normalized to 100 at d_{max} on the beam central axis.*

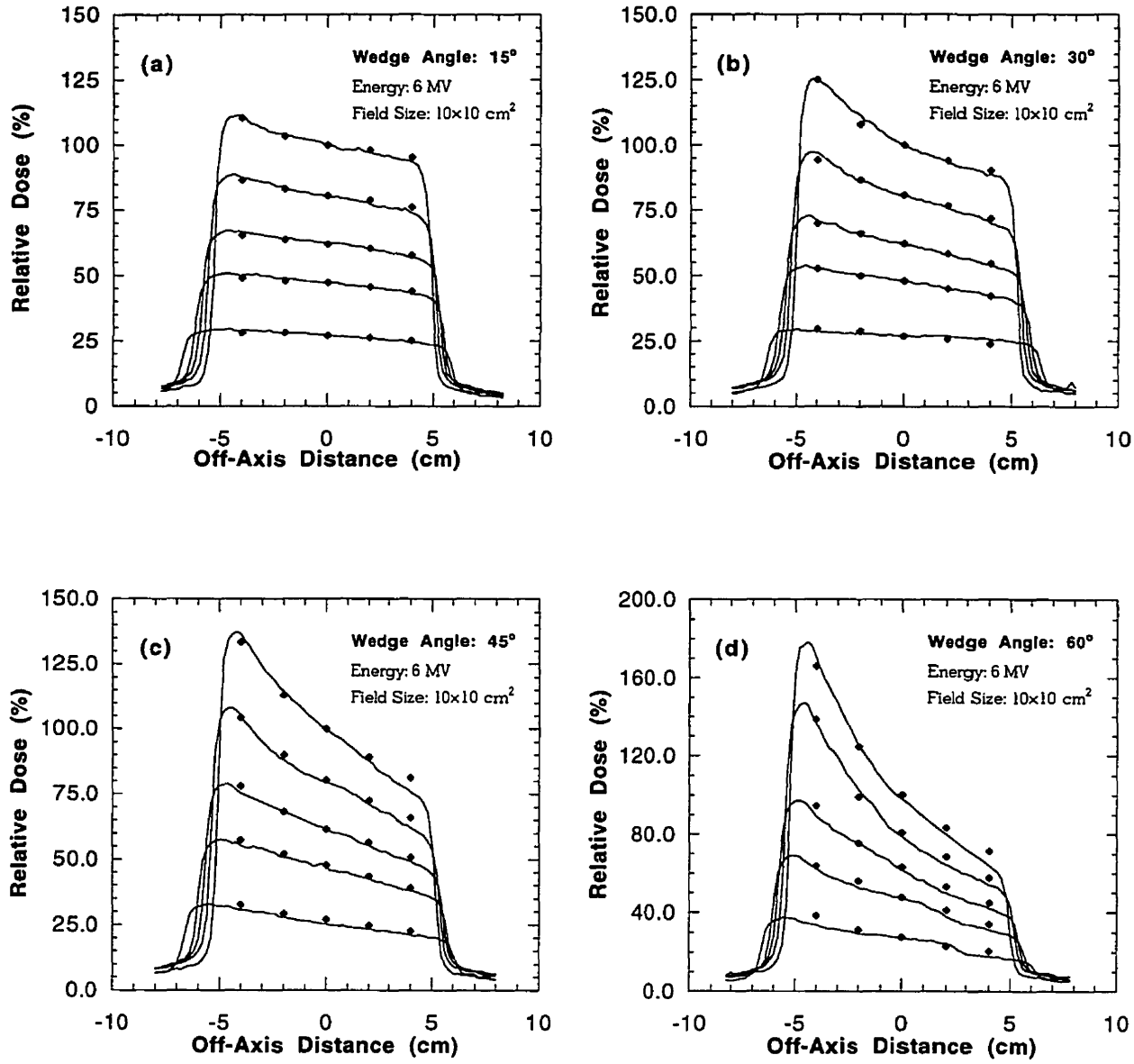

FIGURE 6.18. *Dynamic wedge profiles for the (a) 15° dynamic wedge, (b) 30° dynamic wedge, (c) 45° dynamic wedge, and (d) 60° dynamic wedge at depths of d_{max}=1.5 cm, 6.5 cm, 11.5 cm, 16.5 cm, and 26.5 cm for a 6 MV photon beam with a field size of 10x10 cm². The solid diamonds represent ionization measurements. SSD: 100 cm. Data are normalized to d_{max} on the beam central axis.*

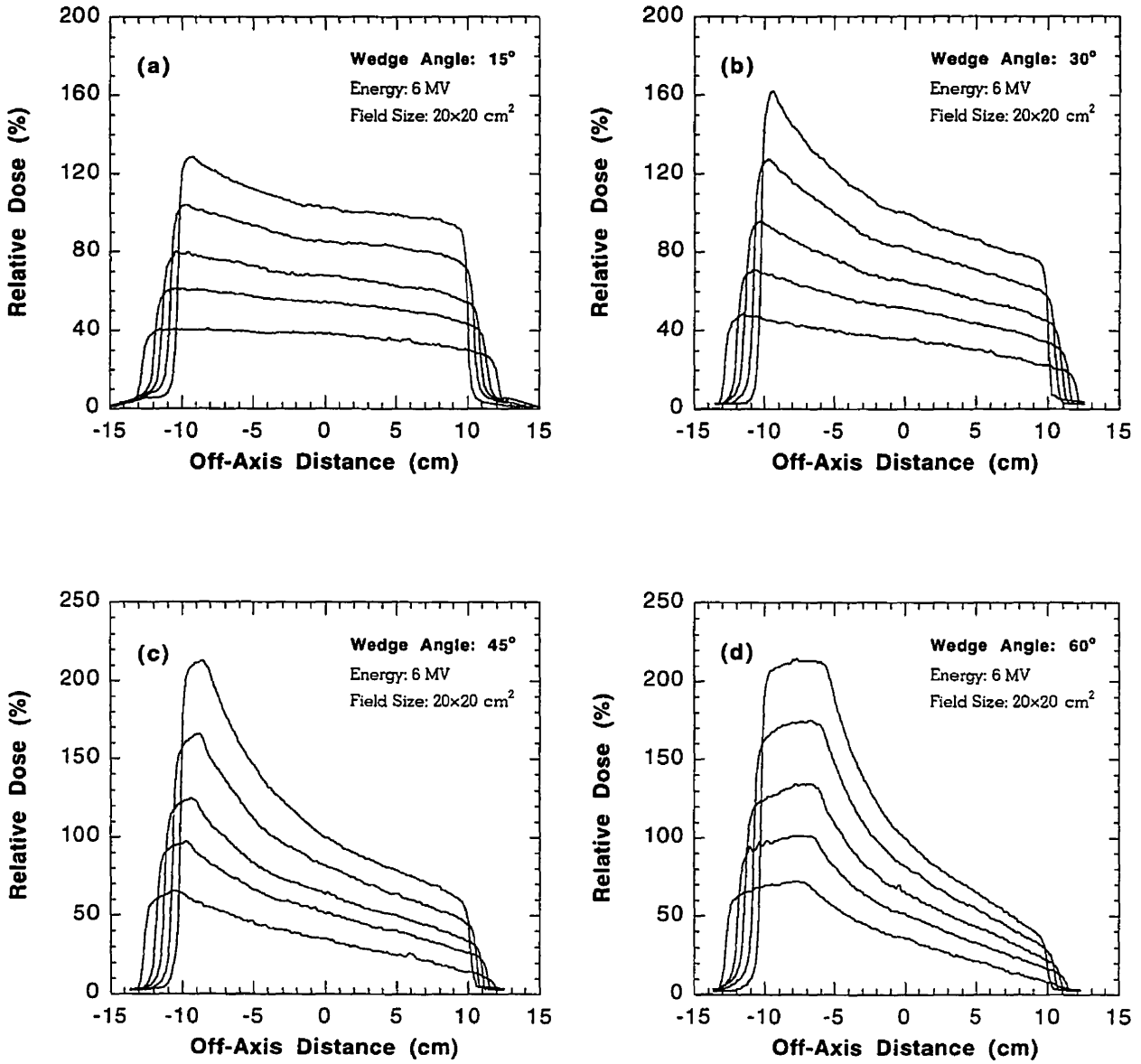

FIGURE 6.19. *Dynamic wedge profiles for the (a) 15° dynamic wedge, (b) 30° dynamic wedge, (c) 45° dynamic wedge, and (d) 60° dynamic wedge at depths of d_{max}=1.5 cm, 6.5 cm, 11.5 cm, 16.5 cm, and 26.5 cm for a 6 MV photon beam with a field size of 20×20 cm². SSD: 100 cm. Data are normalized to 100 on the beam central axis.*

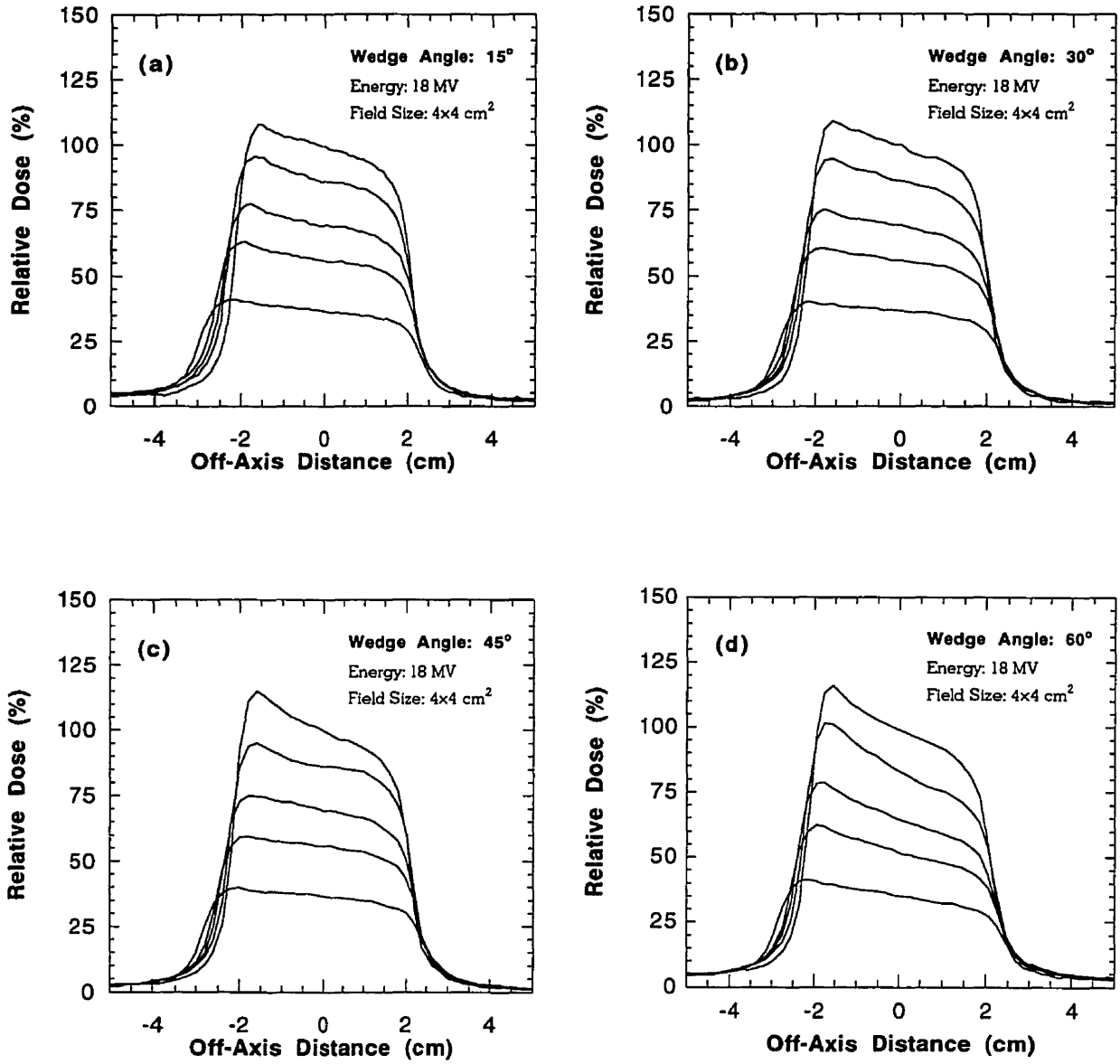

FIGURE 6.20. *Dynamic wedge profiles for the (a) 15° dynamic wedge, (b) 30° dynamic wedge, (c) 45° dynamic wedge, and (d) 60° dynamic wedge at depths of d_{max} =3.0 cm, 8.0 cm, 13.0 cm, 18.0 cm, and 28.0 cm for a 18 MV photon beam with a field size of 4×4 cm². SSD: 100 cm. Data are normalized to 100 at d_{max} on the beam central axis.*

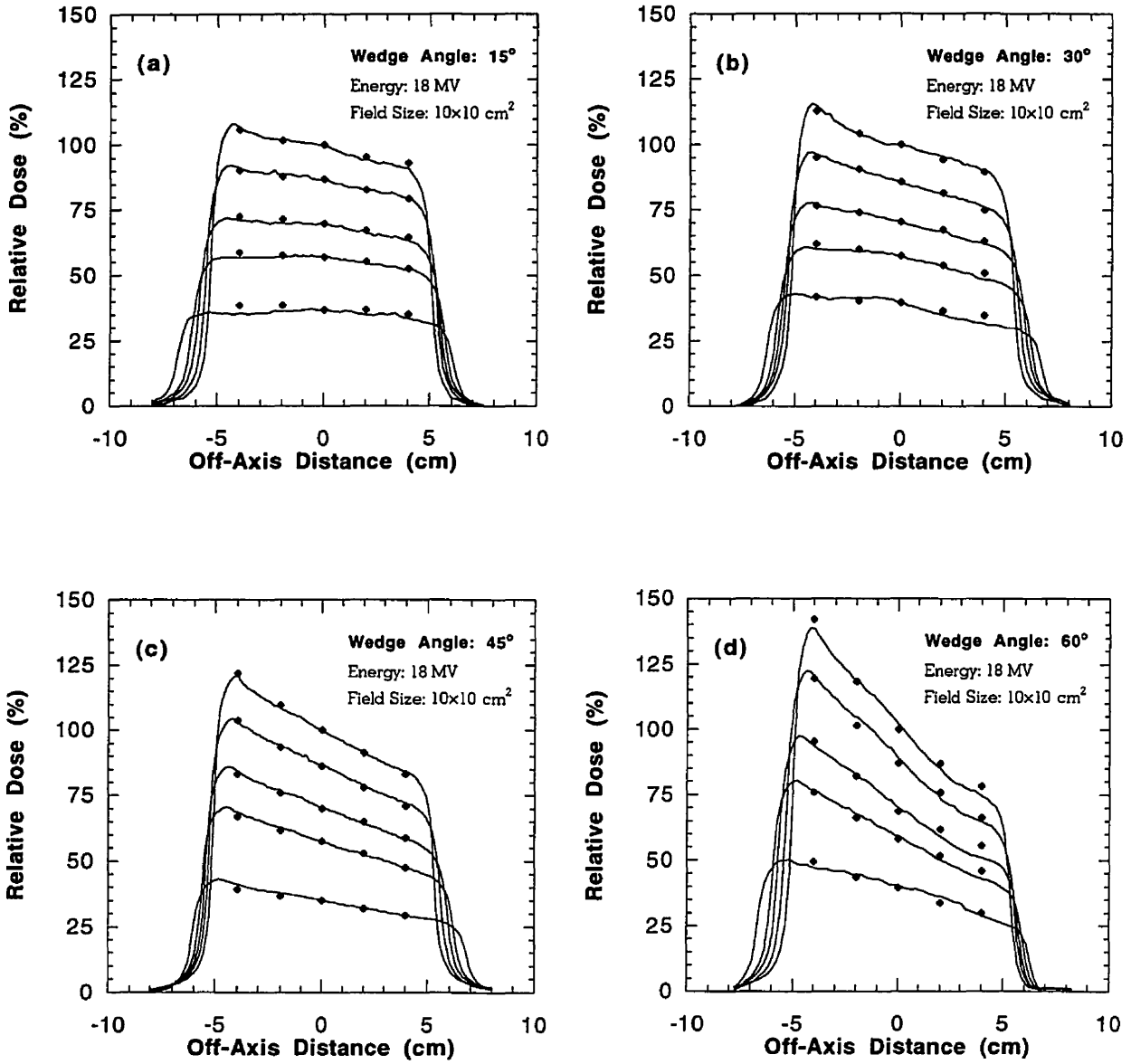

FIGURE 6.21. *Dynamic wedge profiles for the (a) 15° dynamic wedge, (b) 30° dynamic wedge, (c) 45° dynamic wedge, and (d) 60° dynamic wedge at depths of d_{max}=3.0 cm, 8.0 cm, 13.0 cm, 18.0 cm, and 28.0 cm for a 18 MV photon beam with a field size of 10x10 cm². The solid diamonds represent ionization measurements. SSD: 100 cm. Data are normalized to 100 at d_{max} on the beam central axis.*

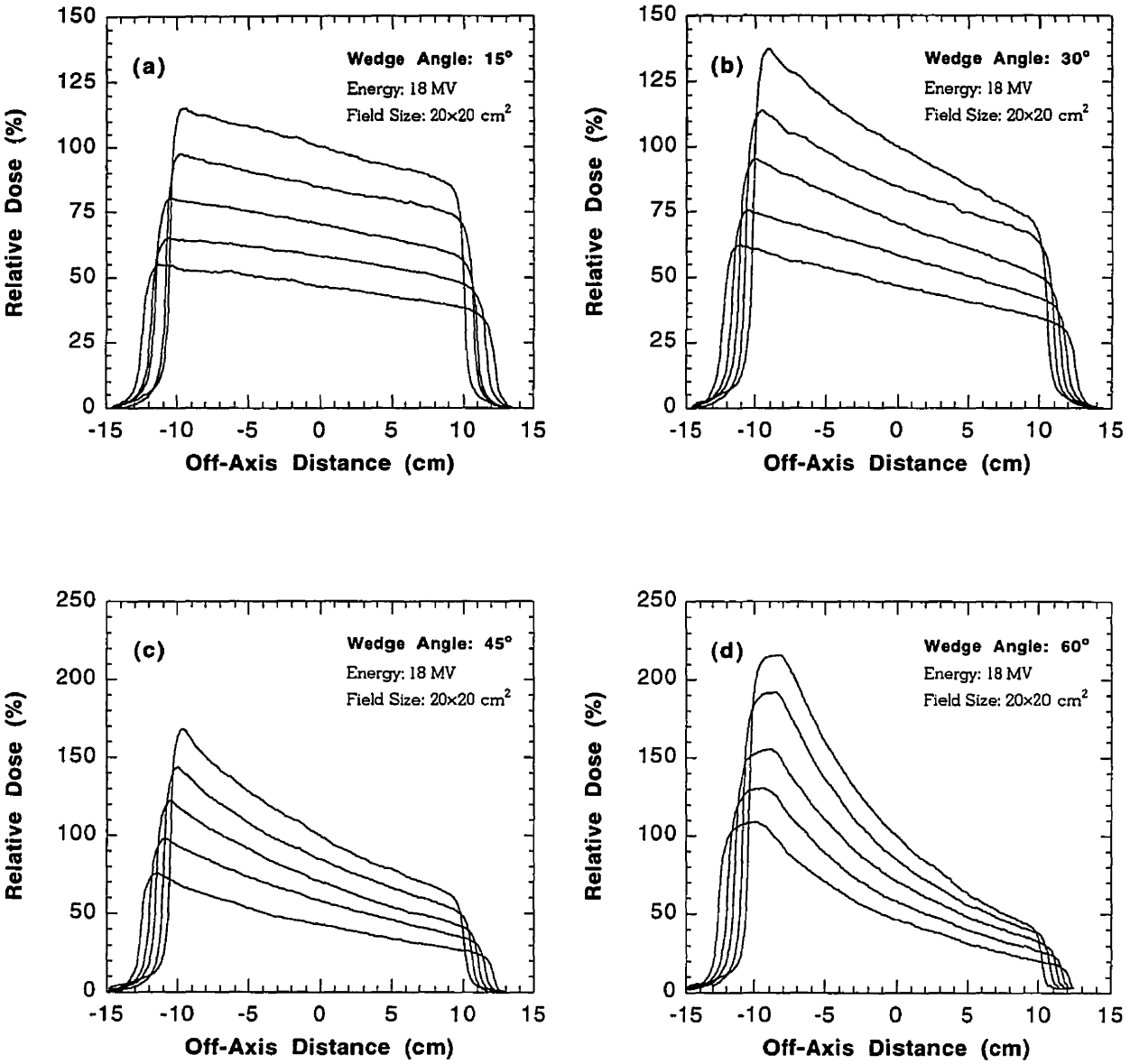

FIGURE 6.22. *Dynamic wedge profiles for the (a) 15° dynamic wedge, (b) 30° dynamic wedge, (c) 45° dynamic wedge, and (d) 60° dynamic wedge at depths of d_{max}=3.0 cm, 8.0 cm, 13.0 cm, 18.0 cm, and 28.0 cm for a 18 MV photon beam with a field size of 20×20 cm². SSD: 100 cm. Data are normalized to 100 at d_{max} on the beam central axis.*

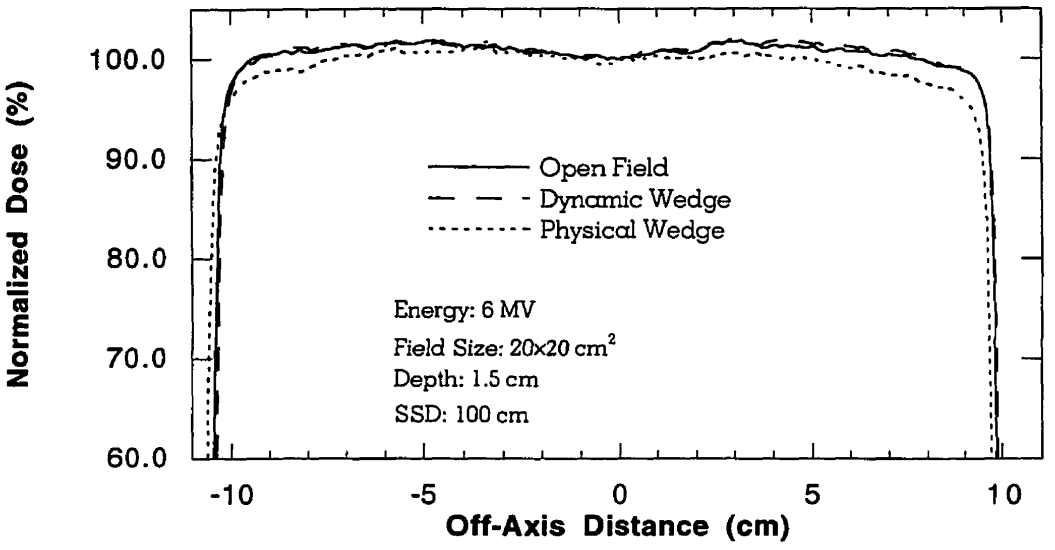

FIGURE 6.23. ***Comparison of open field, dynamic wedge, and physical wedge beam profiles in the non-wedge direction for a 45° wedge angle with a field size of 20×20 cm^2 and a photon beam energy of 6 MV. SSD = 100 cm, depth of measurement d_{max} = 1.5 cm.***

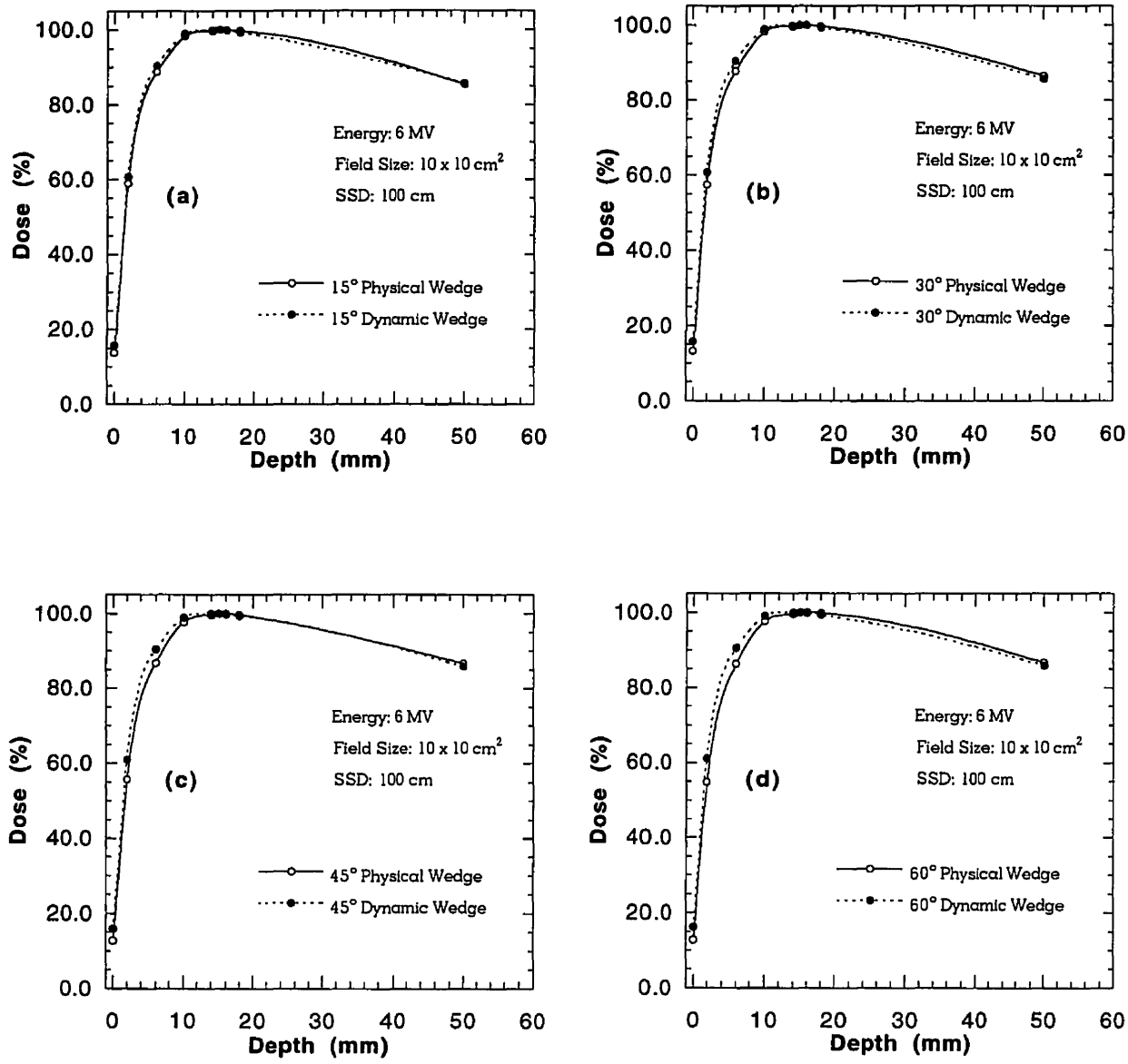

FIGURE 6.25. ***Comparison of build-up region measurements between the dynamic wedge and physical wedge for the (a) 15° dynamic wedge, (b) 30° dynamic wedge, (c) 45° dynamic wedge, and (d) 60° dynamic wedge for a 6 MV photon beam with a field size of 10×10 cm². SSD: 100 cm.***

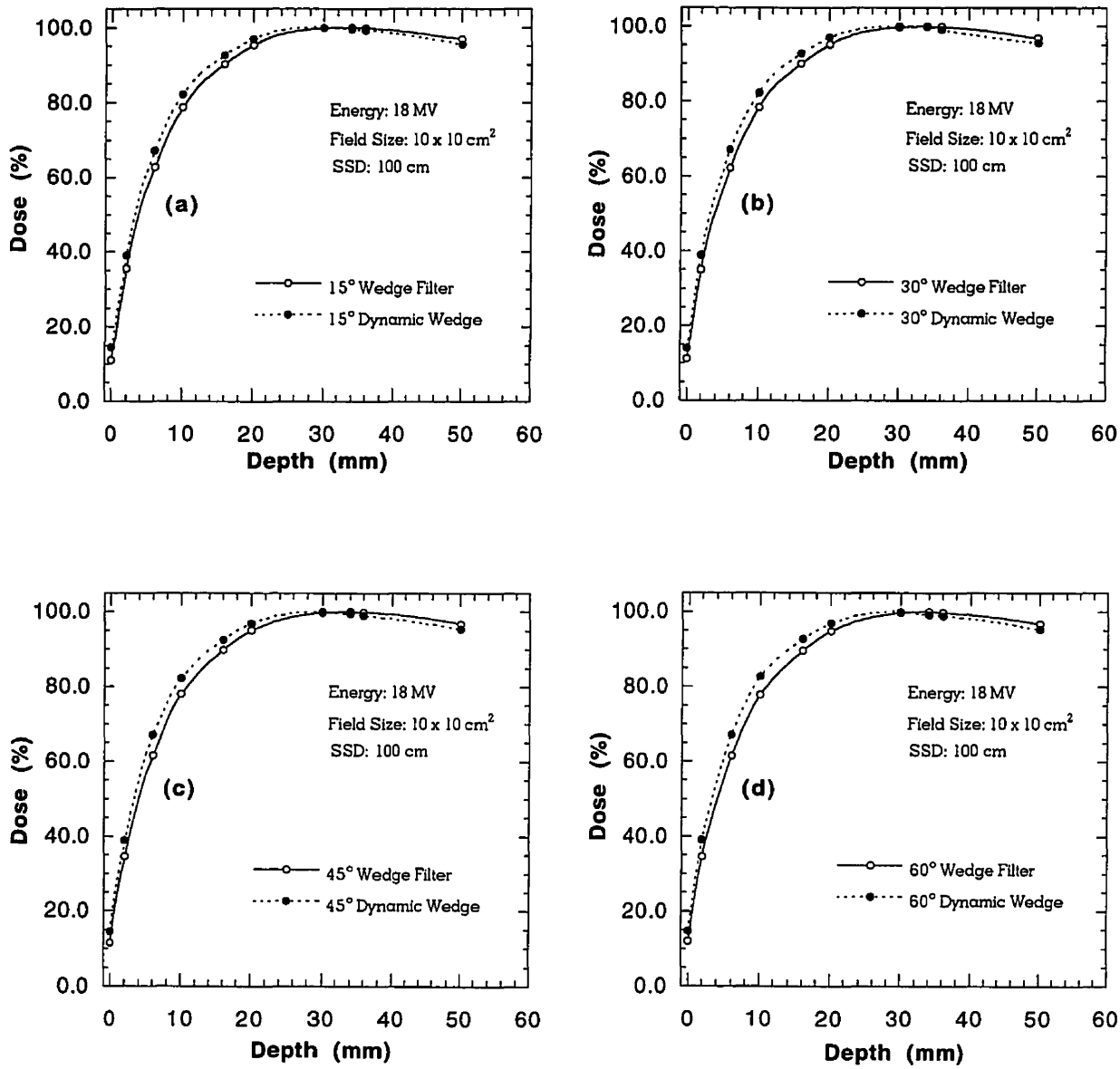

FIGURE 6.26. ***Comparison of build-up region measurements between the dynamic wedge and physical wedge for the (a) 15° dynamic wedge, (b) 30° dynamic wedge, (c) 45° dynamic wedge, and (d) 60° dynamic wedge for an 18 MV photon beam with a field size of 10×10 cm². SSD: 100 cm.***

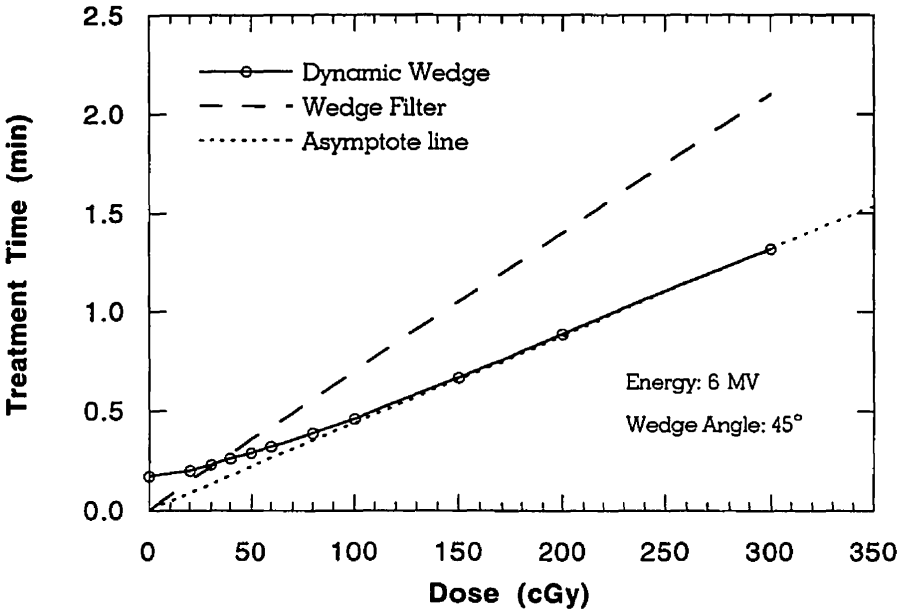

FIGURE 6.27. ***Treatment time curves for a 45° dynamic wedge and physical wedge filter for a 6 MV photon beam with a field size of 10×10 cm². SSD: 100 cm.***

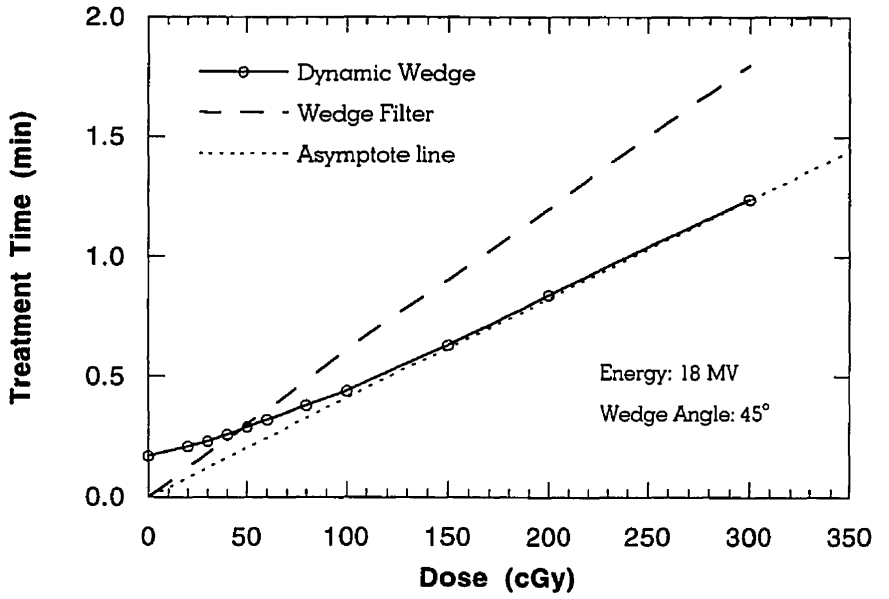

FIGURE 6.28. ***Treatment time curves for a 45° dynamic wedge and physical wedge filter for a 18 MV photon beam with a field size of 10×10 cm². SSD: 100 cm.***

CONCLUSIONS

7.1 Summary

Standard static physical wedge filters provide the traditional method of modifying dose distributions in order to optimize treatment of cancer patients with radiation by generating tilted isodose distributions that compensate for irregular surface contours, missing tissue, and irregular tumor volumes. However, physical wedges are constructed from dense materials that cause certain dosimetric problems such as beam hardening effects. In addition, they result in some practical inconveniences, such as filter handling, blocking of the optical distance indicator, and possible filter misalignment. Through integration of the computer with linear accelerator it is possible to generate wedge shaped isodose distributions dynamically, providing an interesting practical alternative to the standard physical wedge filter.

The dynamic wedge creates wedge-shaped isodose distributions by irradiating different segments of the treatment field for different intervals of time. This is accomplished by moving one of the primary collimators in a continuous fashion to produce a continuously shrinking field width during the entire treatment process. During this dynamic wedge process, the collimator velocity and dose rate are modulated in accordance with the segmented treatment table (STT), which specifies the amount of the cumulative dose delivered as a function of the collimator position. This approach differs significantly from conventional physical wedge filters, since no external beam modifying device is necessary. In this thesis, the dosimetric properties of the dynamic wedge option, available on a Clinac 2300 C/D linear accelerator, were investigated in order to assess the viability of using this radiation modality clinically and on a regular basis.

Unlike the measurement techniques used to accumulate beam data for conventional physical wedges, dynamic beam radiotherapy requires the use of an integrating dosimetry technique, since the treatment field width is continuously changing. Such measurements were performed via the use of film densitometry and with direct integration using an ionization chamber.

The current Clinac 2300 C/D software offers the user the choice of four discrete dynamic wedges designated by their nominal isodose tilt angles of 15°, 30°, 45°, and 60°. Measurements were taken to verify that each of the nominal dynamic wedges operates linearly with prescribed dose and dose rate for both 6 MV and 18 MV photon energies and the largest treatment field size. This was accomplished by collecting data in solid water at the depth of dose maximum d_{max} with a radiation therapy beam monitor and a special electrometer. All four dynamic wedges were found to operate linearly both with prescribed dose and dose rate. This ensures that, if the user changes the dose or dose rate parameters in subsequent dynamic wedge treatments, the same dose, relative to the central axis, will be delivered to all points in each radiation field.

Although the dynamic wedge does not attenuate the photon beam like conventional physical wedges do, there still is an effective wedge factor which has to be accounted for. Measurements in solid water with an Farmer-type ionization chamber reveal that the effective wedge factors (256 in total) have a strong dependence upon field size, increasing as field size decreases. Therefore, it is not possible to use simple interpolation calculations of a square field wedge factor table in order to find the number of monitor units needed to give the prescribed dose at the depth of d_{max}. Moreover, there is a discontinuity in wedge factors between the 9.5×9.5 cm^2 and the 10×10 cm^2 square fields. This occurs, because the STT beam generation algorithm switches from beam weight reference point increments of 0.25 cm to increments of 0.5 cm.

Wedge factors were also measured with variable X-collimator setting in comparison to nominal 4×4 cm^2 and 20×20 cm^2 fields. The results indicate that to within ±1%, the effective wedge factors depend only on the dynamic wedge field width and not on the equivalent square of the radiation field.

The dynamic wedge central axis percentage depth dose (*PDD*) data was measured using a water tank containing a small volume ionization chamber. These measurements were performed for dynamic wedge field sizes of 4×4 cm^2, 10×10 cm^2, and 20×20 cm^2 for all available wedge angles for 6 MV and 18 MV photons. Results indicate that the central axis *PDD* for the dynamic wedge closely approximates measured open field *PDD* data. All measured dynamic wedge data are within ±2% of open field measurements. This is a significant contrast to the *PDD*s of physical wedge filters which can differ from open field data by as much as ~5% because of beam hardening effects. This is not only important for monitor unit calculations but also for treatment planning, and implies that the use of open

field *PDD* data is an appropriate first order approximation in the calculation of dose distributions for treatment calculations.

Beam profiles were measured in solid water using film densitometry techniques, verified by ionization chamber measurements, for all available dynamic wedge angles for 6 MV and 18 MV photon beam energies with field sizes of 4×4 cm^2, 10×10 cm^2, and 20×20 cm^2. Profiles in the non-wedged direction were also measured and compared for open fields, dynamic wedge fields, and physical wedge fields. The dynamic wedge closely approximates the open field dose profile, but delivers a higher dose than the physical wedge filter close to the boundary of the field edge.

The surface doses were measured in solid water using a parallel-plate ionization chamber with a 10×10 cm^2 field for all available dynamic wedges and standard physical wedge angles. The results show that the surface dose for the dynamic wedges is within ±2% of the open field. A slight increase in surface dose was noticed for the 60^o dynamic wedge. However, this increase is not large enough to be of any clinical significance.

The time needed to deliver a single beam dynamic wedge treatment was found to be less than the treatment time for a physical wedge treatment for the delivery of clinically useful doses. This implies that a single dynamically wedged treatment can deliver dose faster and more efficiently than conventional physical wedge filter techniques.

Overall, the technology of the dynamic wedge offers distinct advantages over standard physical wedges, possibly making the latter obsolete.

7.2 Current limitations

Currently, the dynamic wedge is limited in maximum field size (20 cm maximum in the wedge direction) and wedge orientation. Contrary to the physical wedge filter, the dynamic wedge is limited to the Y-direction since only the Y-collimator jaws are dynamic during the treatment process. This allows two of four orientations available with standard physical wedges and requires a collimator rotation to perform wedging in the orthogonal direction. Additionally, the dynamic wedge is currently capable of only four user-selected wedge angles (15^o, 30^o, 45^o, and 60^o) and is limited to symmetric field settings. Moreover, the dynamic wedge cannot be used in conjunction with some electronic portal imagers. Due to their acquisition electronics, a majority of electronic portal imagers require a constant accelerator output. This is accomplished via a pulse length servo board installed in the Clinac 2300 C/D card rack. During dynamic wedge procedures the pulse length is

variable, making it incompatible with most electronic portal imaging techniques, even during the open field portion of the treatment, thus complicating patient imaging.

7.3 Future work

The next generation of dynamic wedges, known as the "enhanced" dynamic wedge, will offer many technological advances over the previous generation. The required advances are the capability of selecting arbitrary wedge angles, the availability of asymmetric field settings, a maximum field width of 30 cm, and the possibility for electronic portal imaging acquisition during the initial open field portion of the wedge.

The major difference between the dynamic wedge and the enhanced dynamic wedge (EDW) is the way in which the segmented treatment tables (STTs) are generated. The dynamic wedge has 132 STTs per photon energy, while the EDW has only 1 STT per photon energy currently referred to as the "Golden STT" (GSTT). The method in which the desired wedge angles are generated from a single STT is illustrated in Fig. 7.1 as a five step process.

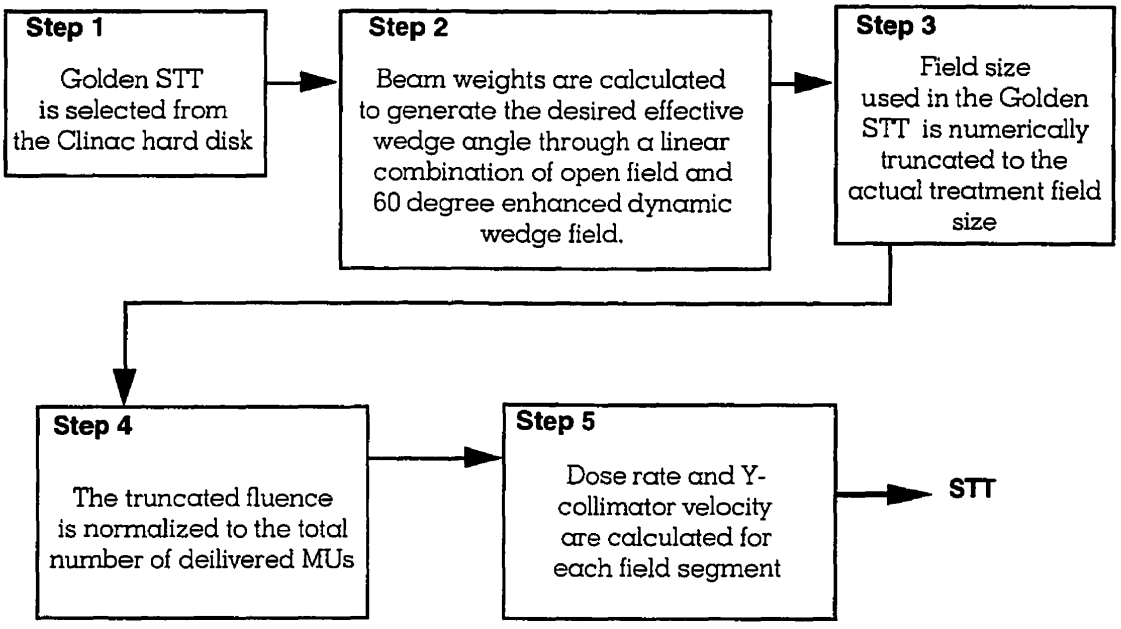

FIGURE 7.1. ***The five step procedure used by the enhanced dynamic wedge to generate an STT table.***

The first step in the enhanced dynamic wedge STT generation sequence is the selection of the appropriate beam fluence profile data set for the user-selected photon energy. This fluence profile data set describes the dose fluence necessary to deliver a maximum field (i.e., 30 cm) 60° enhanced dynamic wedge treatment. One fluence profile set is used for each available photon energy (6 MV or 18 MV). The GSTT for each photon energy is stored permanently on the Clinac computer hard drive and is manipulated in such a way that the STT for any wedge angle and field size can be derived. This method is much simpler than the dynamic wedge, where separate STT tables are stored on hard disk and must be retrieved for every selected combination of wedge angle and field size.

The second step in the enhanced dynamic wedge STT generation procedure is the linear combination of the GSTT with an open field to create a fluence profile set that will generate the desired effective wedge angle. Such a linear combination can be written as follows:

$$D_{\theta} = D_{open} \cdot W_{open} + D_{60} \cdot W_{60} \quad , \tag{7.1}$$

where D_{θ} is the desired dose profile with the effective wedge angle θ, D_{open} is the dose profile of the open field, W_{open} is open field beam weight, D_{60} is the dose profile of the 60 degree enhanced dynamic wedge (i.e., Golden STT fluence data set), and W_{60} is the beam weight of the 60 degree enhanced dynamic wedge beam. The corresponding beam weights, W_{open} and W_{60}, are computed as a function of the effective wedge angle as shown in the following equations:

$$W_{open} = \frac{\tan 60^{o} - \tan\theta}{\tan 60^{o}} \quad , \tag{7.2}$$

$$W_{60} = \frac{\tan\theta}{\tan 60^{o}} \quad , \tag{7.3}$$

By choosing different beam weights the enhanced dynamic wedge offers operator selected wedge angles of 10°, 15°, 20°, 25°, 30°, 45°, and 60°. This is an improvement over the dynamic wedge which offers only 15°, 30°, 45°, and 60°.

The third step in the enhanced dynamic wedge STT generation procedure is the numerical truncation of the maximum field size fluence used in the GSTT to the actual field size in the specific treatment.

Step four is the normalization of the truncated dose fluence to yield the STT that is unique to the treatment setup. The normalization is carried out in such a way that the final dose given to the last field segment is the total number of MUs entered by the operator. The last step occurs after the STT has been correctly normalized, the dose rate and Y-collimator velocity for each field segment is calculated. The procedure of STT delivery is then analogous to that in the dynamic wedge explained in this thesis.

We suspect that, after the technological advances demonstrated with the enhanced dynamic wedge, arbitrary wedge angles will be available in future generations of this treatment modality. This will inevitably make treatment planning easier, since the operator will be able to select a wedge angle that is optimized to each individual patient, making the administration of radiotherapy treatments more efficient.

In closing, implementation of the dynamic wedge technology is a major step towards conformal radiation therapy in which the delivered dose can be modulated to fit irregularly-shaped treatment volumes. This produces a more homogenous dose distribution within the tumor, as compared to conventional radiotherapy techniques, thereby increasing the effectiveness of radiation used in the treatment of cancer. The measurements reported in this thesis were used as the basis for the clinical introduction of the dynamic wedge option on a Clinac-2300 C/D linear accelerator at the Montreal General Hospital.

LIST OF FIGURES

LIST OF TABLES

BIBLIOGRAPHY

Abrath, F. G., J. A. Purdy: *Wedge design and dosimetry for 25 MV X rays*, Radiol. **136**, 757-762 (1980).....pp. 38,40,42,80

Anderson, D. W., F. St. George: *Comparison of Film and Ion Chamber Systems for Depth-dose Measurements for a 25 MV Beam*, Phys. Med. Biol. **24**, 636-638 (1979).....p. 75

Attix, F. H. : Introduction to Radiological Physics and Radiation Dosimetry, John Wiley & Sons, Inc., New York, U.S.A. (1986).....pp. 63

Clinac 2300 C/D maintenance manual, Varian Associates, Palo Alto, California (1992).....pp. 18,19,20,22,23,27,28,34

Constantinou, C., F. H. Attix, B. R. Paliwal: *A solid water phantom material for radiotherapy x-ray and γ-ray beam calibrations*, Med. Phys. **9**, 436-441 (1982).....p. 63

Curry, T. S., J. E. Dowdey, R. C. Murry: Christensen's Physics of Diagnostic Radiology, 4th edition. Lea & Febiger, Philadelphia, U.S.A. (1990).....pp. 20,71

Dutreix, J., A. Dutreix: *Film dosimetry of high energy electrons*, Ann. N.Y. Acad. Sci. **161**, 33-43 (1969).....pp. 71,75

Ho, A. K., B. R. Paliwal: *Stopping power and mass energy-absorption coefficient ratios for solid water*, Med. Phys. **13**, 403-404 (1986).....p. 64

Ho, A. K., B. R. Paliwal, F. H. Attix: *Charge storage in electron-irradiated phantom materials*, Med. Phys. **13**, 99-100 (1986).....p. 64

Hughes, D. B., C.J. Karzmark, R.M. Levy: *Conventions for Wedge Filter Specifications*, Br. J. Radiol. **45**, 868 (1972).....p. 41

Humphries, L. J., T. W. Slowey: "Dosimetry Instrumentation" in Radiation Oncology Physics - 1986 (AAPM Monograph No. 15) (1987).....p. 64

Huntzinger, C. J. : *Dynamic Wedge: A Physicist's Perspective*, Varian Dynamic Wedge Users' Meeting Proc. (Calgary 1992).....p. 58

ICRU report # 24, *Determination of Absorbed Dose in a Patient Irradiated by Beams of X or Gamma Rays in Radiotherapy Procedures*, International Commission on Radiation Units and Measurements, Washington, DC (1976).....pp. 41,58,62

IEC Performance Standard 976, *Medical Electron Accelerators - Functional Performance Characteristics*, International Electrotechnical Commission, Geneva (1989).....p. 58

Johns, H. E, J. R. Cunningham: The Physics of Radiology, 4th edition, Charles C. Thomas, Springfield, Illinois, U.S.A. (1983).....pp. 6,13,30

Karzmark, C. J., C. S. Nunan, E. Tanabe, Medical Electron Accelerators, McGraw-Hill, Inc. (1983).....pp. 2,26,28,30,34

Karzmark, C. J., D. Angelo, R. Loevinger, P. Steed: *Notation and formulae for dose specification and calculations in radiotherapy*, Br. J. Radiol. **39**, 476 (1966).....p. 41

Khan, F. M. : The Physics of Radiation Therapy, 2nd edition, Williams & Wilkins, Maryland, U.S.A. (1994).....pp. 11,39,64

Khan, F. M., K. P. Doppke, K. R. Hogstrom, G. J. Kutcher, R. Nath, S. C. Prasad, J. A. Purdy, M. Rosenfeld, B. L. Werner: *Clinical electron-beam dosimetry: Report of AAPM Radiation Therapy Committee Task Group No. 25*, Med. Phys. **18**, 73-109 (1991).....p. 70

Khan, F. M., B. J. Gerbi, F. C. Deibel: *Dosimetry of asymmetric x-ray collimators*, Med. Phys. **13**, 936-941 (1986).....pp. 49,51

Kijewski, P. K., L. M. Chin, B. D. Bjarngard: *Wedge-shaped dose distributions by computer-controlled collimator motion*, Med. Phys. **5**, 426-429 (1978).....p. 46

Klein, E., D. A. Low, A.S. Meigooni, J. A. Purdy: *Dosimetry and clinical implementation of dynamic wedge*, Int. J. Radiation Oncology Biol. Phys. **31**, 583 -592(1995).....p. 38

Knapp, E. A., B. C. Knapp, J. M. Potter: *Standing wave high energy linear accelerator structures*, Rev. Sci. Instr. **39**, 979-991 (1968).....p. 32

Knoos, T., L. Wittgren: *Which depth dose data should be used for dose planning when wedge filters are used to modify the photon beam?*, Phys. Med. Biol. **36**, 255-266 (1991).....p. 42

Leavitt, D. D., M. Martin, J. H. Moeller, W. L. Lee: *Dynamic wedge field techniques through computer-controlled collimator motion and dose delivery*, Med. Phys. **17**, 87-91 (1990).....p. 47

McCullough, E. C., J. Gortney, C. R. Blackwell: *A depth dependence determination of the wedge transmission factor for 4-10 MV photon beams*, Med. Phys. **15**, 621-623 (1988).....p. 41

Palta, J. R., I. Daftari, N. Suntharalingam: *field size dependence of wedge factors*, Med. Phys. **15**, 624-626 (1988).....pp. 41,42

Patten, L., J. Purdy, G. Oliver: *Automated film dosimetry* [Abstract], Med. Phys. **1**, 110 (1974).....p. 75

Podgorsak, M. B., S. S. Kubsad, B. R. Paliwal: *Dosimetry of large wedged high-energy photon beams*, Med. Phys. **20**, 369-372 (1993).....p. 42

Private communication with Paul Lefebvre, Medical Physics Department, Montreal General Hospital, Montreal, Canada.....p. 34

Private communication with Joe Larkin, Medical Physics Department, Montreal General Hospital, Montreal, Canada.....p. 22

Reft, C. S.: *Output calibration in solid water for high energy photon beams*, Med Phys. **16**, 299-301 (1989).....pp. 63,64

Private communication with Calvin Huntzinger, Varian Oncology Systems, Varian Associates, Inc., Palo Alto, California.....pp. 42,77

Segre, E. : Nuclei and Particles, W.A. Benjamin, Inc., New York (1965).....p. 6

Silverman, R. , J. Distasio, Radiation Therapy with Heavy Particles and Fast Electrons, Noyes Data Corporation, New Jersey, U.S.A. (1980).....p. 1

TG21, *A new protocol for the determination of absorbed dose from high-energy photon and electron beams*, Med. Phys. **10**, 741-771 (1983).....pp. 13,62

Varian, R. H., S. F. Varian: *A high frequency oscillator and amplifier*, Journal of Applied Physics, **10**, 321-327 (1939).....p. 23

White, D. R.: *Tissue substitutes in experimental radiation physics*, Med. Phys. **5**, 467-479 (1978).....p. 63

Williamson, J. F., F. M. Kahn, S. C. Sharma: *Film dosimetry of megavoltage photon beams: A practical method of isodensity-to-isodose curve conversion*, Med. Phys. **8**, 94-98 (1981).....pp. 70,75

Wu, A., R. D. Zwicker, F. Krasin, E. S. Sternick: *Dosimetry characteristics of large wedges for 4 and 6 MV x rays*, Med. Phys. **11**, 186-188 (1984).....p. 80

Yaffe, M., K.W. Taylor, H.E. Johns: *Spectroscopy of diagnostic x rays by a Compton-scattered method*, Med. Phys. **3**, 328-334 (1976).....p. 6

Zankowski, C.: *Monte carlo analysis of the 10 MV x-ray beam from a Clinac-18 linear accelerator*, M.Sc. thesis, McGill University, Montreal, Canada, 1994.....p. 62

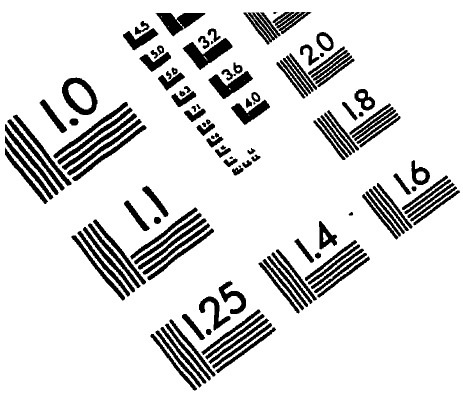

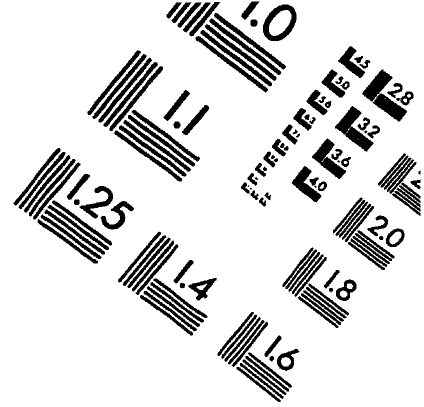

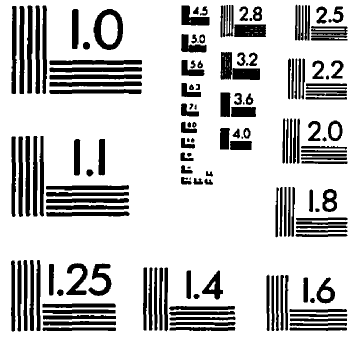

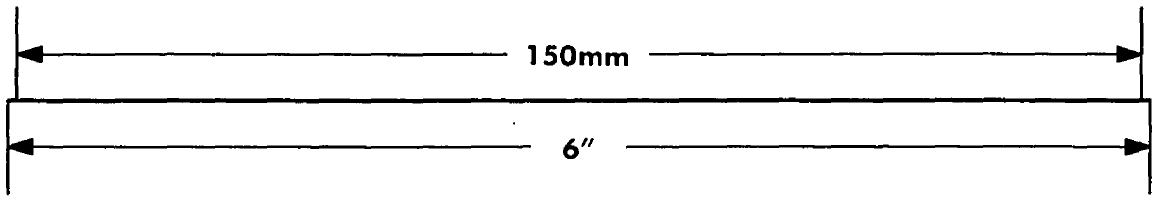

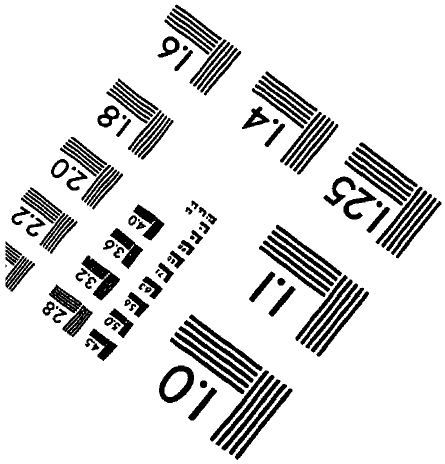

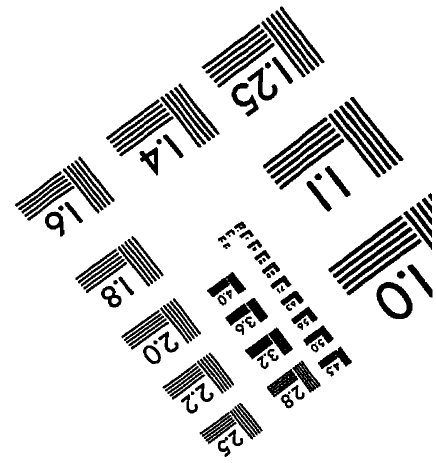

APPLIED IMAGE, Inc
1653 East Main Street
Rochester, NY 14609 USA
Phone: 716/482-0300
Fax: 716/288-5989